Habilitationsschrift

zur
Erlangung der Venia legendi
für das Fach Physik

der
Ruprecht – Karls – Universität
Heidelberg

vorgelegt von
Andreas Glindemann
aus Braunschweig
1997

Beating the Seeing Limit –
Adaptive Optics on Large Telescopes

Abstract

Observations with ground based telescopes suffer from atmospheric turbulence. Independent of the telescope size the angular resolution in the visible is equivalent to that of a telescope with a diameter of 10–20 cm. This effect is caused by the turbulent mixing of air with different temperature in the atmosphere. Thus, the perfectly plane wave from a star at infinity is aberrated before it enters the telescope.

In the following, we will discuss the physical background of imaging through turbulence, using Kolmogorov statistics, and the different techniques to sense and to correct the wave-front aberrations with adaptive optics. We will also present a simulation method for time-evolving turbulence. The requirements for the control loop of an adaptive optics system are discussed including formulas for the limiting magnitude of the guide star as a function of the wave-front sensing method, of the quality of the wave-front sensor camera, and of the degree of correction.

In the discussion of tip-tilt correction by tracking the intensity peak rather than the intensity centroid some new aspects will be presented of the relationship between the properties of the wave-front, and the image intensity distribution. Also, a new method will be discussed to measure and distinguish individual turbulent layers in order to increase the isoplanatic angle.

A short introduction to deformable mirror technology and the principles of adaptive optics with laser guide stars will be followed by examples of adaptive optics systems. Here, we will demonstrate how the image improvement is done in practice. Two tip-tilt systems and ALFA, the adaptive optics system with a laser guide star of the Calar Alto 3.5-m telescope will be presented in detail.

Contents

Chapter 1

Introduction

The image quality of ground based telescopes suffers from atmospheric turbulence. Independent of the telescope size the angular resolution in the visible is equivalent to that of a telescope with a diameter of 10–20 cm. This effect is caused by the turbulent mixing of air with different temperature in the atmosphere. Thus, the perfectly plane wave from a star at infinity is aberrated before it enters the telescope.

It was the idea of H. Babcock in 1953 to correct these aberrations with a deformable mirror to obtain diffraction limited images [3]. The principle of an adaptive optics system is displayed in Fig. 1.1. The deformable mirror, a wave-front sensor and a camera in the corrected focus form the main elements. The wave-front sensor measures the aberrations with a high frame rate and sends the control signals to the deformable mirror in order to correct the aberrations. Then, the corrected focus can be recorded by a camera with an exposure time independent of atmospheric turbulence.

Although this sounds simple, some demanding technical requirements for the wave-front sensor and for the deformable mirror delayed the realisation of adaptive optics systems by several decades. In the US Air Force, adaptive optics systems were developed since 1970 in classified research [35] both for improved imaging of satellites and for the projection of high energy laser beams onto missiles. In the civilian sector, it took until the late 1980's before the COME-ON system of the European Southern Observatories was installed on the 3.6-m telescope in

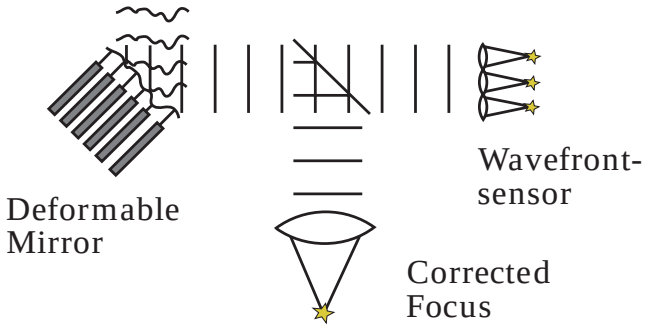

Figure 1.1: The main elements of an adaptive optics system. The wave-front sensor measures the aberrations and sends the information to the deformable mirror to flatten the wave-front. A camera in the corrected focus takes the corrected image.

Chile [60]. In the northern hemisphere, the PUEO adaptive optics system of the Canada-France-Hawaii Telescope was the first to become available to the astronomical community for regular science observations in 1996 [71].

The technical requirements for adaptive optics systems concern the frame rate and the sensitivity of the wave-front sensor camera, and the frequency that can be applied to the deformable mirror. The required frame rate is determined by the rate of changes of the atmospheric turbulences. Therefore, the statistical parameters of the turbulence play a vital role for adaptive optics systems. Kolmogorov statistics provide a suitable theoretical model for atmospheric turbulence. Measurements of the statistical properties have mostly confirmed the assumptions of this theory.

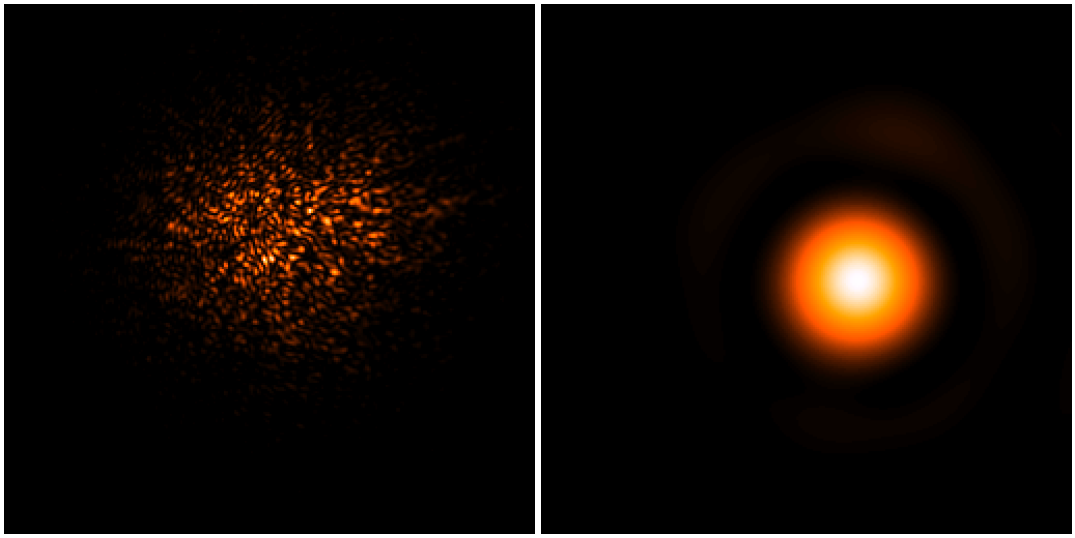

Figure 1.2: Speckle images of a single star in the visible at 0.5 μm (on the left) and at 10 μm (on the right) under identical atmospheric conditions on a 3.5-m telescope. In the 10 μm image, parts of the first diffraction ring can be seen. A simulation for atmospheric turbulence was used to produce the images.

The most important question for the applicability of adaptive optics systems to astronomical research is the question about the sky coverage: how much of the sky can be observed given that a star of suitable brightness, the guide star in the wave-front sensor, has to be close to the object star? The required brightness of the guide star follows from the required frame rate of the wave-front sensor camera determined by the rate of changes in the atmosphere, and from the desired degree of correction. In Fig. 1.2, instanteneous images of a single star on a 3.5-m telescope under identical atmospheric conditions are displayed at different wavelengths. At 10 μm, a single diffraction limited speckle is moving around slowly, and image stabilisation is sufficient to create a diffraction limited image. In the visible at 0.5 μm, a speckle cloud of a few hundred speckles displays a dynamic behaviour like in Brownian motion. Creating a single diffraction limited point spread function requires a deformable mirror with approximately as many actuators as there are speckles. This example illustrates the very different requirements for the adaptive optics system at different wavelengths. Thus, the answer to the question about the sky coverage depends on the desired degree of correction and the subsequent parameters for wave-front sensor frame rate, and on atmospheric conditions.

In the following, we will discuss the physical background of imaging through turbulence, and the different techniques to sense and to correct the aberrations caused by the turbulence. Examples of adaptive optics systems will demonstrate how the image improvement is done in practice.

The chapters are organised as follows. In Chapter 2, after a short introduction to the notation used in Fourier optics, the Kolomogorov statistics and the impact on the imaging process are discussed, and a simulation method is presented. The emphasis in Chapter 3 is put on wave-front sensing and reconstruction, and on closed loop operation. The limiting magnitude of the guide star is expressed quantitatively as a function of the wave-front sensing method, of the quality of the wave-front sensor camera, and of the degree of correction. The discussion of tip-tilt correction by tracking the intensity peak rather than the intensity centroid contains some new aspects of the relationship between the properties of the wave-front and the image intensity distribution.

Also in Chapter 3, the deformable mirror technology and the principles of adaptive optics with laser guide stars are introduced. The chapter closes with the presentation of a new method to measure and distinguish individual turbulent layers in order to increase the isoplanatic angle.

In Chapter 4, examples of adaptive optics systems are given, incorporating the discussion of Chapter 3. Two tip-tilt systems and ALFA, the adaptive optics system with a laser guide star of the Calar Alto 3.5-m telescope will be presented in detail.

For further reading on this subject, the book by R. K. Tyson [89] covers the field in great detail, and M. C. Roggemann and B. M. Welsh devote several chapters in their book on imaging through turbulence to adaptive optics [79]. The conference proceedings of a NATO summer school on adaptive optics, edited by D. Alloin and J.-M. Mariotti [2], contains interesting contributions for the expert reader.

Chapter 2

Imaging through Atmospheric Turbulence

In the following, the relevant theoretical framework for understanding imaging through atmospheric turbulence will be discussed. For a more detailed description the reader is referred to the review by Roddier [73] which is mainly based on the analysis of wave propagation in a turbulent medium by Tatarski [85].

In the first section of this chapter, the quantities and the underlying theory of the imaging process are briefly stated. In the following sections, first Kolmogorov's mathematical model to describe atmospheric turbulence is introduced [46]. Then, the statistical properties of the electromagnetic wave are discussed, and the impact on image motion and the appearance of the image are investigated. Finally, a numerical method for simulation of Kolmogorov turbulence is presented.

2.1 Preliminaries

The wave propagation through the atmosphere and the telescope into the focal plane is very conveniently described by Fresnel diffraction. Incorporating optical elements like lenses or mirrors in a spherical approximation leads to the well known Fourier relationship between the amplitude of the electromagnetic wave in the pupil of the telescope and the amplitude in its focal plane [30, 5, 53].

We use the notation $\Psi(\vec{x})$ for the complex amplitude in the telescope pupil and $A(\vec{u})$ for the complex amplitude in the focal plane. The two quantities are connected through a Fourier transform

$$A(\vec{u}) = \int \Psi(\vec{x}) \exp(2\pi i \vec{x}\vec{u})\, d\vec{x},$$

where the integration is performed over the telescope pupil. The phase $\phi(\vec{x})$ of $\Psi(\vec{x})$ incorporates the turbulent atmosphere as well as the telescope aberrations. In the telescope focus, we are usually interested in the intensity distribution $I(\vec{u}) = |A(\vec{u})|^2$ that can be written as

$$\begin{aligned} I(\vec{u}) &= \iint \Psi(\vec{x}')\Psi^*(\vec{x}'') \exp(2\pi i(\vec{x}' - \vec{x}'')\vec{u})\, d\vec{x}' d\vec{x}'' \\ &= \int \left(\int \Psi(\vec{x}')\Psi^*(\vec{x}' - \vec{x}) d\vec{x}' \right) \exp(2\pi i \vec{x}\vec{u})\, d\vec{x}, \end{aligned}$$

where $\int \Psi(\vec{x}')\Psi^*(\vec{x}'-\vec{x})d\vec{x}'$ is the autocorrelation of the amplitude in the telescope pupil that is called the optical transfer function (OTF). If a plane wave from a point source at infinity enters a perfect, *i.e.* aberration free, telescope the OTF is a purely real function – approximately shaped like a triangle – and its Fourier transform is the diffraction limited point spread function, the Airy disk.

In the case of statistical fluctuations of the electromagnetic wave, due to an incoherent source or atmospheric turbulence, the autocorrelation can be expressed as an ensemble average over all possible realisations, called the coherence function:

$$\Gamma(\vec{x}) = < \Psi(\vec{x'})\Psi^*(\vec{x'}-\vec{x}) > .$$

It is one of the main tasks of turbulence theory to connect the atmospheric properties to the coherence function in the telescope pupil and, thus, to its Fourier transform, the point spread function (PSF) in the telescope focal plane. If atmospheric turbulence rather than the telescope diameter limits the size of the PSF it is called the seeing disk and its full width at half maximum (FWHM) is called the *seeing*.

2.2 Kolmogorov turbulence

The statistics of the spatial and temporal structure of atmospheric turbulence is of great importance to describing the propagation of light through the atmosphere. Following from the theory of fluid motion the flow of air becomes turbulent, *i.e.* unstable and random, if the *Reynolds number* $Re = L_0 v_0/k_v$ exceeds a critical value, where L_0 is the characteristic size of the flow, v_0 is the characteristic velocity and k_v is the kinematic viscosity. With typical numbers for these parameters, $L_0 \approx 15\,\mathrm{m}$, $v_0 \approx 10\,\mathrm{m/sec}$ and $k_v = 15 \times 10^{-6}$ it is $Re \approx 10^5$ which corresponds to fully developed turbulence.

Kolmogorov suggested that the kinetic energy in the largest structures of the turbulence is transferred successively to smaller and smaller structures [46]. He also assumed that the motion of the turbulent structure is both homogeneous and isotropic implying that the second and higher order statistical moments of the turbulence depend only on the distance between any two points in the structure. If the product of the characteristic size L of the small structure and its velocity v is too small to keep the Reynolds number in the turbulent regime the break up process stops and the kinetic energy is dissipated as heat by viscous friction. In a stationary state, the energy flow from larger structures L to smaller structures l must be constant, *i.e.* the amount of energy that is being injected into the largest structure must be equal to the energy that is dissipated as heat. If the typical transfer time of the kinetic energy E through a structure of size l is given by l/v the energy flow rate, ϵ_0 can be written as

$$\epsilon_0 = \frac{E(L)}{t(L)} = \frac{E(l)}{t(l)} = \frac{\frac{1}{2}mv^2}{l/v} = \mathrm{const}, \tag{2.1}$$

and it is

$$v \propto \epsilon_0^{1/3} l^{1/3}. \tag{2.2}$$

The kinetic energy $E(k)$ in the spectral range k and $k+dk$ is proportional to v^2. With the spatial frequency $k \propto l^{-1}$ one obtains

$$E(k)dk \propto k^{-2/3} \text{ or } E(k) \propto k^{-5/3}. \tag{2.3}$$

For isotropic turbulence the three dimensional case can be calculated by integrating over the unit sphere:

$$E(k) = 4\pi k^2 E(\vec{k}) \Rightarrow E(\vec{k}) \propto k^{-11/3}. \tag{2.4}$$

This relationship expresses the Kolmogorov spectrum. It holds in the *inertial range* of turbulence for $L_0^{-1} \ll k \ll l_0^{-1}$ where L_0 is the outer scale of turbulence, generally the size of the largest structure that moves with homogeneous speed, and l_0 is the inner scale at which the viscous dissipation starts. The outer scale of turbulence varies between a few meters close to the ground where the largest structure is determined by the height over the ground, and a few hundred meters in the free atmosphere which is the thickness of the turbulent layer [10, 86, 33]. The inner scale of turbulence is in the range of a few millimetres near the ground to about $1\,\mathrm{cm}$ near the tropopause [73].

2.3 Index-of-refraction fluctuations

Light traveling through the atmosphere is affected by fluctuations of the refraction index. The physical source of these fluctuations are temperature inhomogeneities produced by turbulent mixing of air. The index of refraction as a function of wavelength is given by the Cauchy formula [94]

$$n(\lambda) = 1 + (272.6 + \frac{1.22}{\lambda^2})10^{-6}, \tag{2.5}$$

with λ in $\mu\mathrm{m}$ and the numerical parameters for 15°C and 1000 mbar. $n(\lambda)$ for different temperatures is displayed in Fig. 2.1. Both numerical parameters depend slightly on temperature and pressure. However, this dependence can be neglected in the second parameter (that is 1.22 in Eq. 2.5), and the index of refraction $n(\vec{r})$ can be modelled as the sum of a purely wavelength dependent part $n(\lambda)$, and a randomly fluctuating part $n_f(\vec{r})$ depending on temperature and pressure. This approximation has the consequence that the shape of the wave-front is independent of the wavelength. Effects that show a wavelength dependence, like the different number of speckles in the optical and in the infrared, are caused by the different relative impact of the same wave-front distortion at different wavelengths.

Using $n(\lambda) \approx 1$, the refraction index as a function of temperature and pressure at optical and near infrared wavelengths can be written as [43]

$$n(\vec{r}) - 1 = n_f(\vec{r}) = \frac{77.6\,P}{T}10^{-6}, \tag{2.6}$$

where T is the temperature of the air in Kelvin and P the pressure in millibar. It can be shown that the refraction index as a passive, conservative additive, *i.e.* a quantity that does not affect atmospheric turbulences and that is not affected by the motion of the air, also follows Kolmogorov

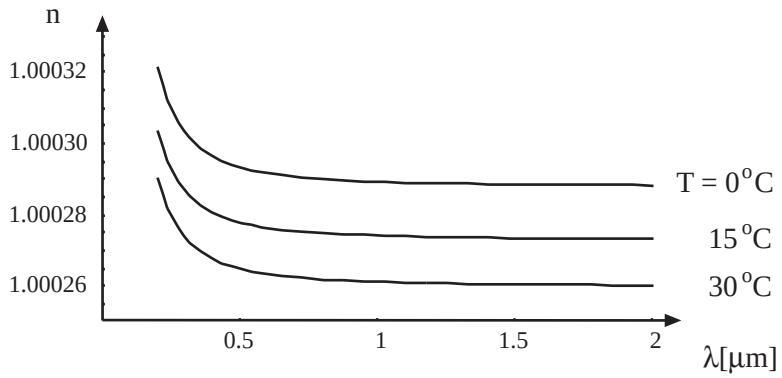

Figure 2.1: The refraction index of air at 0, 15 and 30^oC and 1000 mbar as given by the Cauchy formula. The dependence on temperature can be modeled by approximating the refraction as a sum of temperature and wavelength dependent terms.

statistics [63]. Then, the power spectral density $\Phi_n(k)$ of $n(\vec{r})$ has the same spatial frequency dependence as the kinetic energy and can be expressed as

$$\Phi_n(k) = 0.033\ C_n^2\ k^{-11/3}. \tag{2.7}$$

The quantity C_n^2 is called the *structure constant* of the refraction index fluctuations and has units of $\mathrm{m}^{-2/3}$. It characterises the strength of the refraction index fluctuations. Measurements of C_n^2 have shown a good agreement with the Kolmogorov theory (see *e.g.* Hufnagel [41] and Clifford [9]). The latest measurements of C_n^2 have been performed by Klückers et al. [45] using a method suggested by Vernin [92].

Based on measurements Hufnagel, together with Valley [90] suggested a model for the atmospheric turbulence profile called the Hufnagel-Valley-Boundary model. As the profile varies from site to site and from time to time this model can only give a rough idea of the layer structure. The structure constant can be modelled using the formula

$$C_n^2(h) = 2.2 \times 10^{-23} h^{10} e^{-h}\ +\ 10^{-16} e^{-h/1.5}\ +\ 1.7 \times 10^{-14} e^{-h/0.1}. \tag{2.8}$$

Like the statistical distribution of velocity discussed in Sect. 2.2 the refraction index distribution is isotropic and homogeneous as long as the spatial frequencies involved are in the inertial range, with $L_0^{-1} \ll k \ll l_0^{-1}$. The Kolmogorov theory predicts a mathematical form for $\Phi_n(k)$ only inside the inertial range. The von Karman spectrum [43] models the power spectral density also outside of this regime.

So far, only the power spectral density of the refraction index fluctuations has been discussed. The power spectral density is related to the autocorrelation $\Gamma_n(\vec{r}) =< n(\vec{r_1})n(\vec{r_1}+\vec{r}) >$ by the Wiener-Khinchin theorem:

$$\Gamma_n(\vec{r}) = \int \Phi_n(|\vec{k}|) e^{-2\pi i \vec{k}\vec{r}} d\vec{k}. \tag{2.9}$$

As already noted, the random process leading to the fluctuation of the refractive index is isotropic and homogeneous. Thus, second and higher moments of n, like the autocorrelation depend only on the distance between two points. This allows us to express both the power spectral density

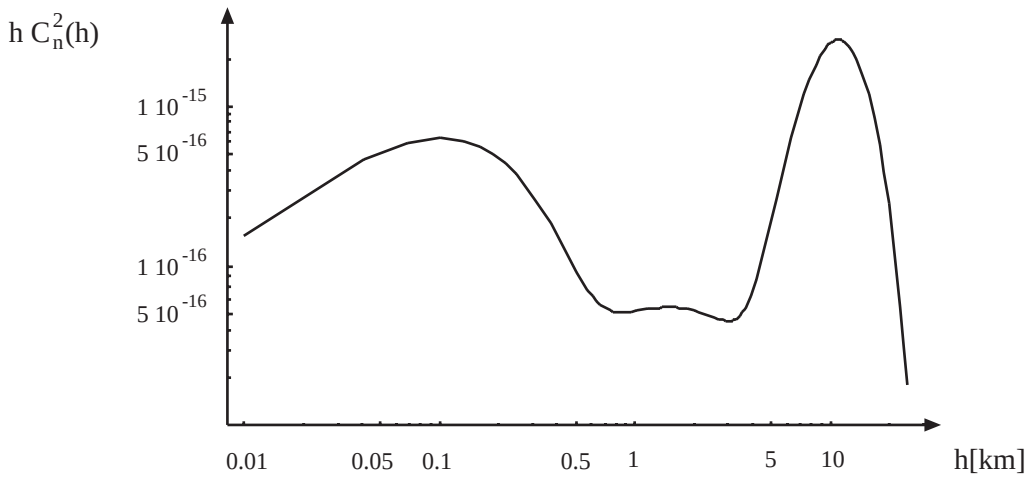

Figure 2.2: Average C_n^2 profile as a function of altitude in km as given by the Hufnagel-Valley model. Two distinct layers can be distinguished, near the ground (100 m) and at 10 km. For better visualisation the hC_n^2 vs. $\log h$ presentation was chosen.

and the autocorrelation as functions of the three dimensional vectors $\vec{k}$ and $\vec{r}$ where $|\vec{k}|$ and $|\vec{r}|$ are denoted by k and r respectively.

To avoid the integration over the pole at $k = 0$ the *structure function* of the refraction index is introduced as

$$\begin{aligned} D_n(r) &= < |n(r_1) - n(r_1 + r)|^2 > \\ &= 2(< n(r_1)^2 > - < n(r_1)n(r_1 + r) >) \\ &= 2(\Gamma_n(0) - \Gamma_n(r)) \ . \end{aligned}$$

The result of this calculation was derived by Obukhov [63]:

$$D_n(r) = C_n^2 r^{2/3}. \tag{2.10}$$

This form of the structure function of the refractive index is known as Obukhov's law. Together with the Kolmogorov spectrum (Eq. 2.7) it forms the basis for the description of wave propagation through turbulence.

2.4 Statistical properties of the aberrated complex wave

For the sake of simplicity, only horizontal monochromatic plane waves are considered, propagating downwards through atmospheric turbulence from a star at zenith. The fluctuations of the complex amplitude are calculated by using the Kolmogorov spectrum and Obukhov's law.

2.4.1 Thin layer turbulence model

Using the thin screen approximation [73], the layer thickness is assumed to be large compared to the correlation scale of the fluctuations but small enough to neglect diffraction effects within the

layer. Also, the layer is non-absorbing and its statistical properties depend only on the altitude h, *i.e.* the structure constant C_n^2 does not vary in the horizontal direction.

After propagation through a thin turbulent layer at altitude h, the phase is related to the distribution of the refractive index through

$$\phi_h(\vec{x}) = \frac{2\pi}{\lambda} \int_h^{h+\delta h} n(\vec{x}, z) dz, \tag{2.11}$$

where δh is the thickness of the layer and $\vec{x} = (x, y)$ denotes the horizontal coordinate vector. The complex amplitude after propagation through a layer at altitude h can be written as

$$\Psi_h(\vec{x}) = e^{i\phi_h(\vec{x})}. \tag{2.12}$$

To describe the statistical properties of the complex wave we need the correlation function of the complex amplitude, the coherence function, defined as

$$\begin{aligned} \Gamma_h(\vec{x}) &= < \Psi_h(\vec{x'}) \Psi_h^*(\vec{x'} + \vec{x}) > \\ &= < e^{i[\phi_h(\vec{x'}) - \phi_h(\vec{x'} + \vec{x})]} > . \end{aligned} \tag{2.13}$$

As the intensity distribution in the telescope focal plane is the Fourier transform of the coherence function in the telescope aperture, its description as a function of the atmospheric properties determines the telescope point spread function affected by atmospheric turbulence, *i.e.* the seeing disk.

Since the phase $\phi_h(\vec{x})$ is the sum of a large number of independent variables (the refraction indices $n(\vec{x}, z)$, Eq. 2.11) it is reasonable to apply the central-limit theorem implying that $\phi_h(\vec{x})$ and also $\phi_h(\vec{x'}) - \phi_h(\vec{x'} + \vec{x})$ follow Gaussian statistics. Then, the expectation value in Eq.(2.13) is called the characteristic function of the Gaussian random process, and it is defined as

$$< e^{izv} > = \int e^{izx} p_v(x) dx = e^{-\frac{1}{2} < v^2 > z^2}, \tag{2.14}$$

where $p_v(x)$ denotes the Gaussian distribution of the random variable v. In Eq.(2.13) v is the Gaussian distributed phase difference $\phi_h(\vec{x'}) - \phi_h(\vec{x'} + \vec{x})$ and z equals unity. Using these properties, the coherence function can be written as

$$\Gamma_h(\vec{x}) = e^{-\frac{1}{2} < [\phi_h(\vec{x'}) - \phi_h(\vec{x'} + \vec{x})]^2 >}, \tag{2.15}$$

or, introducing the phase structure function $D_{\phi,h}(\vec{x}) = < [\phi_h(\vec{x'}) - \phi_h(\vec{x'} + \vec{x})]^2 >$,

$$\Gamma_h(\vec{x}) = e^{-\frac{1}{2} D_{\phi,h}(\vec{x})}. \tag{2.16}$$

The problem of determining the coherence function of the complex amplitude is now shifted to calculating the phase structure function $D_{\phi,h}(\vec{x})$. The relation between the three-dimensional distribution of the refraction index and the two-dimensional distribution of the phase is given by Eq.(2.11). This leads from the three-dimensional structure function of the refraction index (Eq. 2.10) to the one of the phase $D_{\phi,h}(\vec{x})$ that depends on the two-dimensional vector $\vec{x}$. Assuming also that δh is much larger than the correlation scale of the fluctuations, one can show

that for a horizontal wave-front entering the layer i at altitude h_i, the phase structure function at the exit of the layer is [17]

$$D_{\phi,h_i}(\vec{x}) = 2.91(\frac{2\pi}{\lambda})^2 \delta h_i C_{n_i}^2 |\vec{x}|^{5/3}. \tag{2.17}$$

In the following the scalar variable $x = |\vec{x}|$ will be used.

D_{ϕ,h_i} is the phase structure function of the phase in rad. If the phase is given in the dimension of meter it describes the physical shape of the turbulent wave-front. It is interesting to note that the phase structure function of the phase in meter, and thus the shape of the phase, is independent of wavelength. This follows from $n(\vec{r}) = n(\lambda) + n_f(\vec{r})$. It is $D^m_{\phi,h_i} = D_{\phi,h_i} \times (\frac{\lambda}{2\pi})^2 = 2.91\delta h_i C_{n_i}^2 |\vec{x}|^{5/3}$. Therefore a wave-front sensor can be operated in the visible determining the shape of the wave-front and steering the deformable mirror for observations in the infrared.

2.4.2 Multiple layers, the Fried parameter

The extension to multiple layers is relatively straightforward. At the beginning of this section, the complex amplitude at the exit of a layer at altitude h_{i+1} can be related to that at the entrance of that layer by multiplication with the phase disturbance,

$$\Psi_{h_{i+1}}(x) = \Psi_{h_i}(x) e^{-i\phi_{h_{i+1}}(x)}, \tag{2.18}$$

and the coherence function can be determined by

$$\begin{aligned} < \Psi_{h_{i+1}}(x')\Psi^*_{h_{i+1}}(x'+x) > &= < \Psi_{h_i}(x')\Psi^*_{h_i}(x'+x) >< e^{i[\phi_{h_{i+1}}(x') - \phi_{h_{i+1}}(x'+x)]} > \\ &= < \Psi_{h_i}(x')\Psi^*_{h_i}(x'+x) > e^{-\frac{1}{2}D_{\phi,h_{i+1}}(x)}. \end{aligned} \tag{2.19}$$

Calculating the coherence function iteratively for all layers one obtains the coherence function on the ground in the telescope aperture after propagation through N turbulent layers as

$$\begin{aligned} < \Psi_0(x')\Psi^*_0(x'+x) > &= e^{-\frac{1}{2}D_{\phi,0}(x)}, \text{with} \\ D_{\phi,0}(x) &= 2.91(\frac{2\pi}{\lambda})^2 \sum_{i=1}^{N} \delta h_i C_{n_i}^2 \; x^{5/3}. \end{aligned} \tag{2.20}$$

The distances between the layers and the size of the diffraction structures are such that the propagation of the complex amplitude has to be described by Fresnel diffraction. That means that the complex amplitude on the ground fluctuates both in amplitude and in phase. The propagation of the coherence function through the atmosphere, however, is reduced to a simple product of the coherence functions of the single layers, unaffected by Fresnel diffraction [73]. This reflects the general property of the coherence function that Fresnel terms cancel when describing the propagation of the coherence function through space or through an optical system [53, 20].

In the case of a continuous distribution of turbulence and of a source at zenith distance γ one obtains

$$D_{\phi,0}(x) = 2.91(\frac{2\pi}{\lambda})^2 (\cos\ \gamma)^{-1} x^{5/3} \int C_n^2(h) dh. \tag{2.21}$$

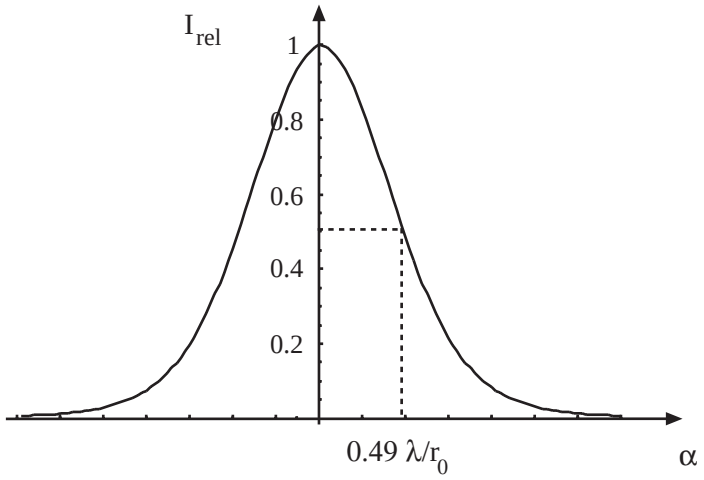

Figure 2.3: The intensity distribution in a seeing disk in arbitrary units calculated numerically using the phase structure function $D_\phi(x) = 6.88\left(\frac{x}{r_0}\right)^{5/3}$. The full width at half maximum (FWHM) is approximately λ/r_0.

Fried further simplified the expression by introducing the quantity r_0, called the Fried parameter [16], which is defined by

$$r_0 = \left(0.423\ (\frac{2\pi}{\lambda})^2(\cos\ \gamma)^{-1}\int C_n^2(h)dh\right)^{-3/5}. \tag{2.22}$$

The wavelength dependence of r_0 is given by $r_0 \propto \lambda^{6/5}$ and the dependence on zenith angle is $r_0 \propto (\cos\gamma)^{3/5}$.

The phase structure function in the telescope pupil can now be expressed by

$$D_{\phi,0}(x) = 6.88\left(\frac{x}{r_0}\right)^{5/3}, \tag{2.23}$$

and the coherence function in the telescope pupil is

$$\Gamma_0(x) = < \Psi_0(x')\Psi_0^*(x'+x) > = e^{-3.44(\frac{x}{r_0})^{5/3}}. \tag{2.24}$$

If a single star is observed through the telescope the turbulence limited point spread function is obtained by computing the Fourier integral of the coherence function over the circular telescope aperture. Fig. 2.3 displays the turbulence limited point spread function, that is called the seeing disk. A Gaussian function models the seeing disk reasonably well. However, with the Gaussian approximation the seeing disk converges to zero much faster than measured seeing profiles that are better described by the Kolmogorov model. The full width half maximum (FWHM) of the seeing disk is $0.98\lambda/r_0$ corresponding in good approximation to a telescope with diameter r_0. With $r_0 \propto \lambda^{6/5}$ the seeing is $\lambda/r_0 \propto \lambda^{-1/5}$, *i.e.* it is decreasing slowly with increasing wavelength.

Very often the power spectrum of the phase fluctuations is needed for analysis. Similar to the calculation that related the Kolmogorov spectrum of refractive index fluctuations (Eq. 2.7)

to the structure function of the refractive index (Eq. 2.10) the Kolmogorov power spectrum of the phase fluctuations can be calculated [62], yielding

$$\Phi(k) = 0.023\ r_0^{-5/3}\ k^{-11/3}. \tag{2.25}$$

The integral over the power spectrum gives the variance of the phase. As noted above, the integral over $\Phi(k) \propto k^{-11/3}$ is infinite. This means, that the variance of the turbulent phase is infinite which is a well known property of Kolmogorov turbulence. If the outer scale is finite the (finite) variance can be calculated using the von Karman spectrum. In general, the phase variance increases with increasing outer scale.

2.4.3 Anisoplanatic and temporal effects

So far we have discussed a single plane wave originating from a star at an angular distance γ from zenith. By calculating the coherence function as the ensemble average over many realisations of the atmospheric turbulence we have effectively determined the time average and, thus, the time averaged seeing disk. A snapshot image of a single random realisation of the turbulence displays the well known speckle image caused by the quasi frozen turbulence of the atmosphere. The light of a star at a slightly different angular position travels through slightly different portions of the atmosphere – the more different the higher the contributing layers are – and displays a different speckle pattern. However, the long time exposures of the two stars are identical as long as the statistical characteristics of the turbulent layers, *i.e.* C_n^2, do not differ. In speckle interferometry this property allows the use of a reference star that might be separated by several degrees from the science object but that still has the same statistical parameters.

In adaptive optics systems the guide star has to be very close to the observed object in order to measure a wave-front that closely resembles the object wave-front. The two quantities, the acceptable angular distance between the object and the guide star (the isoplanatic angle), and the rate of the temporal decorrelation of the turbulence that determines the required frame rate of the wave-front sensor camera, are the most important limiting factors for the performance.

The isoplanacy can be quantified in a very simple way: The displacement by an angle $\vec{\theta}$ is replaced by the lateral shift $\vec{\theta}h$ of the relevant layer at altitude h, and the phase distribution in the observing direction $\vec{\theta} + \vec{\theta'}$ can be expressed by a shift of the phase at $\vec{\theta'}$:

$$\phi(\vec{x}, \vec{\theta} + \vec{\theta'}) = \phi(\vec{x} - \vec{\theta}h, \vec{\theta'}). \tag{2.26}$$

The angular phase structure function, describing the correlation between the phase distribution in $\vec{\theta}$ and $\vec{\theta'}$ can be written as

$$\begin{aligned} D_\phi(\vec{\theta}) &= < [\phi(\vec{x}, \vec{\theta'}) - \phi_h(\vec{x} - \vec{\theta}h, \vec{\theta'})]^2 > . \\ &= 6.88 \left(\frac{\theta h}{r_0}\right)^{5/3}. \end{aligned} \tag{2.27}$$

The influence of different layers with different wind speeds can be investigated by applying the individual altitudes h_i of the individual layers i with structure constants $C_{n_i}^2$ (see Eq. 2.20) and performing the summation.

For the simplest case of a single dominant layer at altitude h an isoplanatic angle can be defined as $\theta_0 = r_0/h$. Thus, if the main turbulent layer is at an altitude of 10 km and $r_0 = 60\,\mathrm{cm}$, which corresponds to 0.76″ seeing in the near infrared at $\lambda = 2.2\,\mu\mathrm{m}$[1], it is $\theta_0 = 12''$. This value can only give an idea of the order of magnitude of the isoplanatic angle. In practical cases the value depends on the particular composition of the atmosphere and the degree of the adaptive correction. For low order adaptive optics, *e.g.* a tip-tilt system or low altitude layers the angle may be much larger.

Using the Taylor hypothesis of frozen turbulence the temporal evolution can be estimated. The assumption is that a static piece of turbulence moves with constant speed $\vec{v}$ in front of the telescope aperture. Then the phase at point $\vec{x}$ at time $t' + t$ can be written as

$$\phi(\vec{x}, t' + t) = \phi(\vec{x} - \vec{v}t, t'), \tag{2.28}$$

and the temporal phase structure function is

$$D_\phi(\vec{v}t) = < [\phi(\vec{x}, t') - \phi(\vec{x} - \vec{v}t, t')]^2 > . \tag{2.29}$$

The temporal difference is thus transformed to a difference in spatial coordinates with the difference being $\vec{v}t$. The phase structure function depends individually on the two coordinates parallel and perpendicular to the wind direction. In the direction of the wind speed a simple estimate of the correlation time similar to the isoplanatic angle above yields the coherence time $\tau_0 = r_0/|\vec{v}|$. A wind speed of $v = 10\,\mathrm{m/sec}$ and a Fried parameter of $r_0 = 60\,\mathrm{cm}$ give a coherence time of $\tau_0 = 60\,\mathrm{msec}$. In speckle interferometry, this is approximately the exposure time that can be used for single speckle images. For adaptive optics the reciprocal of the coherence time indicates the required bandwidth of the closed loop correction system. Greenwood [32], after more elaborate analysis, gave a definition for the required bandwidth, the so-called Greenwood frequency that is often used to specify adaptive optics system. For a single turbulent layer this frequency is $f_G = 0.43v/r_0$ (see Sect. 3.4.2). Multiple layers with different speeds are considered equivalently to the case of anisoplanacy by applying individual speed vectors to individual layers with structure constants $C_{n_i}^2$.

The temporal power spectrum of the phase fluctuations can be calculated from the spatial power spectrum $\Phi(|\vec{k}|)$ (Eq. 2.25). With $\vec{v}$ being *e.g.* parallel to the x axis, one sets $k_x = f/v$ and performs an integration over k_y to obtain the temporal power spectrum $\Phi_t(f)$ [11],

$$\Phi_t(f) = 1/v \int \Phi(f/v, k_y)\, dk_y = 0.077\, r_0^{-5/3}\, \frac{1}{v}\, \left(\frac{f}{v}\right)^{-8/3} . \tag{2.30}$$

The variance of the phase fluctuations is the integral over the temporal power spectrum. As there is a pole at $f = 0$ this integral is infinite which is the well known property of Kolmogorov turbulence discussed above [85]. This integral can be computed if the outer scale L_0 is taken to be finite. As already noted, the Kolmogorov spectrum is not defined outside the inertial range and the von Karman spectrum has to be used to perform the integration.

[1] The atmosphere transmits only certain bands in the infrared. One important band in the near infrared is the *K* band at 2.2±0.2 μm. Most of the numerical examples will be given for this band.

2.5 Image motion

In the last section, the statistical properties of the propagating turbulent wave-front have been described. When it comes to analysing the imaging process in the telescope, some assumptions have to be made about the phase distribution in the telescope aperture. We assume that the turbulent atmosphere can be represented by a single thin layer in the telescope aperture neglecting the effects of Fresnel diffraction, *e.g.* scintillation, discussed in Sect. 2.4 [73].

The average gradient of the phase distribution in the telescope aperture determines the position of the image in the telescope focus. Although this is a low-order effect of atmospheric turbulence on the imaging process it is worthwhile discussing it in more detail as it determines the requirements for wave-front sensors like the Shack-Hartmann sensor that rely on reconstructing the wave-front from gradient measurements in the subapertures.

First we discuss the statistical properties of the gradient $\vec{\theta}$ of the wave-front without averaging over the telescope aperture. The two components θ_x and θ_y as a function of the horizontal coordinate $\vec{x} = (x, y)$ are [73]

$$\theta_x(x,y) = -\frac{\lambda}{2\pi}\,\frac{\partial}{\partial x}\phi(x,y) \text{ and } \theta_y(x,y) = -\frac{\lambda}{2\pi}\,\frac{\partial}{\partial y}\phi(x,y)\ . \tag{2.31}$$

The power spectra of the two vector components $\Phi_{\theta_x}(\vec{k})$ and $\Phi_{\theta_y}(\vec{k})$ are related to the power spectrum of the phase $\Phi(|\vec{k}|)$ by

$$\Phi_{\theta_x}(\vec{k}) = \lambda^2 k_x^2 \Phi(|\vec{k}|) \text{ and } \Phi_{\theta_y}(\vec{k}) = \lambda^2 k_y^2 \Phi(|\vec{k}|)\ , \tag{2.32}$$

and the power spectrum $\Phi_\theta(\vec{k})$ is obtained by adding Φ_{θ_x} and Φ_{θ_y}, since $\Phi_\theta(\vec{k}) = |\hat{\vec{\phi}}_\theta(\vec{k})|^2 = |\hat{\phi}_{\theta_x}(\vec{k})|^2 + |\hat{\phi}_{\theta_x}(\vec{k})|^2 = \Phi_{\theta_x}(\vec{k}) + \Phi_{\theta_y}(\vec{k})$ where $\hat{\phi}_\theta$ is the Fourier transform of the gradient $\theta(\vec{x})$. It is

$$\Phi_\theta(k) = 0.023\lambda^2(k_x^2 + k_y^2) r_0^{-5/3} k^{-11/3} = 0.023\lambda^2 r_0^{-5/3} k^{-5/3}. \tag{2.33}$$

The effect of averaging the gradient over the telescope aperture is considered by convolving the gradient in Eq.(2.31) with the aperture function $A(\vec{x})$ that usually has a circular shape. The central obscuration usually can be neglected. The averaged gradient can be written as

$$\theta_x^D(\vec{x}) = \int \theta_x(\vec{x'}) A(\vec{x} - \vec{x'}) d\vec{x'}, \tag{2.34}$$

where the superscript D indicates the average over the aperture D. For a point like aperture the averaging process collapses yielding $\theta_x^D(\vec{x}) = \theta_x(\vec{x'})$. The convolution transforms into a multiplication in Fourier space and one obtains the power spectrum of the phase gradient after averaging with the telescope aperture [54, 11]

$$\Phi_\theta^D(k) = 0.023\lambda^2 r_0^{-5/3} k^{-5/3} \left| \frac{2J_1(\pi Dk)}{\pi Dk} \right|^2 , \tag{2.35}$$

with J_1 the first order Bessel function describing the diffraction limited point spread function, the Airy disk, which is the Fourier transform of the circular aperture [5]. The Bessel function acts

like a low pass filter on the power spectrum. The contributions at high frequencies corresponding to small distances in the turbulent wave-front are reduced as the averaging process smoothes the gradients. At low frequencies, *i.e.* for large distances the effect of the pupil averaging is much reduced and the power spectrum is unaffected.

The variance of the image motion can be calculated by integrating over the power spectrum $\Phi_\theta^D(k)$ yielding the two-axis variance of the position θ of the image centroid as [88]

$$(\Delta\theta)^2 = 0.34(\lambda/r_0)^2(D/r_0)^{-1/3}[\mathrm{arcsec}^2], \tag{2.36}$$

with λ/r_0 the seeing in arcsec. The quotient D/r_0 will appear in all those formulas that describe the imaging process in the telescope. In practical cases it can be calculated quite easily as it relates the size of the seeing disk λ/r_0 to the FWHM of the Airy pattern λ/D, $\frac{\lambda/r_0}{\lambda/D} = D/r_0$. In 0.76″ seeing at $2.2\,\mu\mathrm{m}$ on a 3.5-m telescope it is $D/r_0 = 6$. The dependence of $(\Delta\theta)^2$ on $D^{-1/3}$ means that the variance of the image motion increases with decreasing telescope diameter. It is important to note that $(\Delta\theta)^2$ is independent of wavelength; the image motion in arcsec is the same at all wavelengths. Thus, wave-front sensors like the Shack-Hartmann sensor measuring the wave-front gradient can be operated in the visible for corrections at all wavelengths.

2.5.1 Temporal evolution of image motion

The Taylor hypothesis of frozen turbulence is used again to estimate the effect of moving turbulence. The temporal power spectrum of the averaged phase gradient can be calculated similar to the one of the phase (Eq. 2.30) by integrating over the direction perpendicular to the wind speed. It is

$$\Phi_{\theta,t}(f) = 1/v \int \Phi_\theta^D(f/v, k_y)\, dk_y. \tag{2.37}$$

This integral cannot be solved in closed form. Tyler [88] gave an approximation for the power spectrum at low and high frequencies that can be simplified by assuming that there is one dominant layer with wind speed $\hat{v}$ [22]. Then, the power spectral density of the centroid motion in the two regimes are

$$\begin{aligned} P_{f_{\mathrm{low}}} &= 0.096(r_0/\hat{v})^{1/3}(\lambda/r_0)^2 f^{-2/3}[\mathrm{arcsec}^2/\mathrm{Hz}], \\ P_{f_{\mathrm{high}}} &= 0.0013(D/\hat{v})^{-8/3}(\lambda/r_0)^2(D/r_0)^{-1/3} f^{-11/3}[\mathrm{arcsec}^2/\mathrm{Hz}], \end{aligned} \tag{2.38}$$

where λ/r_0 is the seeing in arcsec. In Fig. 2.4 , $P_{f_{\mathrm{low}}}$ and $P_{f_{\mathrm{high}}}$ are displayed and compared to measured power spectra. In the low frequency region the power spectrum decreases with $f^{-2/3}$ and it is independent of the size of the aperture D. In the high frequency region the spectrum is proportional to $f^{-11/3}$ decreasing with D^{-3}. This illustrates the influence of the Bessel function as a low pass filter that leaves the low frequency region unaffected by the aperture and that takes effect as soon as the frequency is beyond a value of $f_t = 0.24\hat{v}/D$ which is the transient region between the two approximations. This value agrees well with the value given by Conan [11]. Because of the steep slope ($\propto f^{-11/3}$) of the power spectrum at frequencies beyond the transient frequency f_t the contributions to the image motion are very small. Thus, a tip-tilt system that stabilises the image motion must have a bandwidth of approximately f_t to correct for most of the

turbulence induced image motion. In Chapter 3, the bandwidth requirements will be discussed in greater detail.

The increasing variance of the image motion with smaller apertures D can now be attributed to an increase of the power spectrum in the high frequency region. In order to stabilise the image motion on smaller telescopes the correction frequency has to be higher. It is interesting to note that if the telescope aperture is larger than the outer scale of turbulence L_0 the image motion is reduced below the values predicted by Kolmogorov statistics. This affects in particular the fringe motion on telescope interferometers with a baseline longer than L_0.

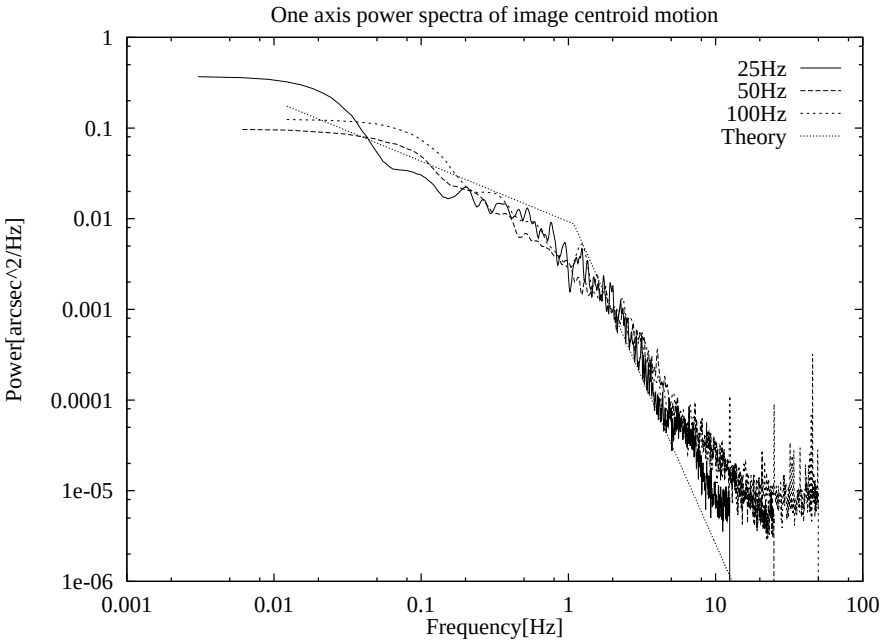

Figure 2.4: Measured power spectra of the image centroid motion on a 3.5-m telescope for different sampling frequencies. The dashed lines display the approximation for the same seeing and wind parameters. From the transient frequency of about $f_t = 1\,\mathrm{Hz}$ and $D = 3.5\,\mathrm{m}$ the effective wind speed can be estimated to be $\hat{v} \approx 14\,\mathrm{m/sec}$. The measurements agree very well with each other and reasonably well with the theoretical curve (dotted line) [22].

2.6 Zernike representation of atmospheric turbulence

In the theory of optical aberrations Zernike polynomials are used very often to describe the aberrations. They were introduced in 1934 by F. Zernike who deduced them from the Jacobi polynomials and slightly modified them for the application in optics [97]. Zernike polynomials have the advantage that they are mathematically well defined and that the low order terms are related to the classical aberrations like astigmatism, coma and spherical aberration.

Since the Zernike polynomials are defined on the unit circle and since we are interested in the turbulent wave-front in the circular telescope aperture it is useful to express the wave-front in terms of the Zernike polynomials. The influence of the central obscuration is negligible. Noll [62] introduced a normalisation for the polynomials that is particularly suited for application to

Kolmogorov turbulence. In this normalisation the rms value of each polynomial over the circle is set equal to one. The Zernike polynomials form a set of orthogonal polynomials and it is convenient to write them as a function of ρ and θ:

$$\begin{aligned} Z_{j_{\text{even}}} &= \sqrt{n+1}\, R_n^m(\rho)\sqrt{2}\, \cos(m\theta), \text{ for } m \neq 0, \\ Z_{j_{\text{odd}}} &= \sqrt{n+1}\, R_n^m(\rho)\sqrt{2}\, \sin(m\theta), \text{ for } m \neq 0, \\ Z_j &= \sqrt{n+1}\, R_n^0(\rho), \text{ for } m = 0, \end{aligned} \tag{2.39}$$

where

$$R_n^m(\rho) = \sum_{s=0}^{\frac{n-m}{2}} \frac{(-1)^s (n-s)!}{s!(\frac{n+m}{2}-s)!\,(\frac{n-m}{2}-s)!}\, \rho^{n-2s}. \tag{2.40}$$

Table 2.1 shows the low order Zernike polynomials where the columns m indicate the azimuthal orders and the rows n the radial orders, and Fig. 2.5 displays them graphically.

n	m = 0	1	2	3
0	Z_1=1 (piston)			
1		Z_2=$2\rho\cos\theta$ Z_3=$2\rho\sin\theta$ (tip and tilt)		
2	Z_4=$\sqrt{3}\,(2\rho^2-1)$ (focus)		Z_5=$\sqrt{6}\,\rho^2\sin 2\theta$ Z_6=$\sqrt{6}\,\rho^2\cos 2\theta$ (astigmatism)	
3		Z_7=$\sqrt{8}(3\rho^3$–$2\rho)\sin\theta$ Z_8=$\sqrt{8}(3\rho^3$–$2\rho)\cos\theta$ (coma)		Z_9=$\sqrt{8}\rho^3\sin 3\theta$ Z_{10}=$\sqrt{8}\rho^3\cos 3\theta$ (trifoil)
4	Z_{11}=$\sqrt{5}(6\rho^4$–$6\rho^2$+1) (spherical aberration)			

Table 2.1: Zernike polynomials Z_j for $j = 1$ to 11. n is the radial order and m the azimuthal order. The modes are ordered such that even j correspond to the symmetric modes given by $\cos m\theta$ and odd j to the antisymmetric modes given by $\sin m\theta$

It is interesting to note that every Zernike polynomial is balanced in order to minimise the remaining aberration. For instance, if pure coma is considered to be $\propto \rho^3$, the Zernike coma (Z_7 and Z_8) has an additional linear term ρ that tilts the wave-front so that the contribution of this aberration is minimised in the sense that the integral over the square of the aberration Z_7^2, the phase variance, is at a minimum. In Sect. 3.1 we will come back to this property.

The polynomial expansion of the arbitrary wave-front $\phi(\rho,\theta)$ over the unit circle is defined as

$$\phi(\rho,\theta) = \sum_{i=1}^{\infty} a_i Z_i(\rho,\theta), \tag{2.41}$$

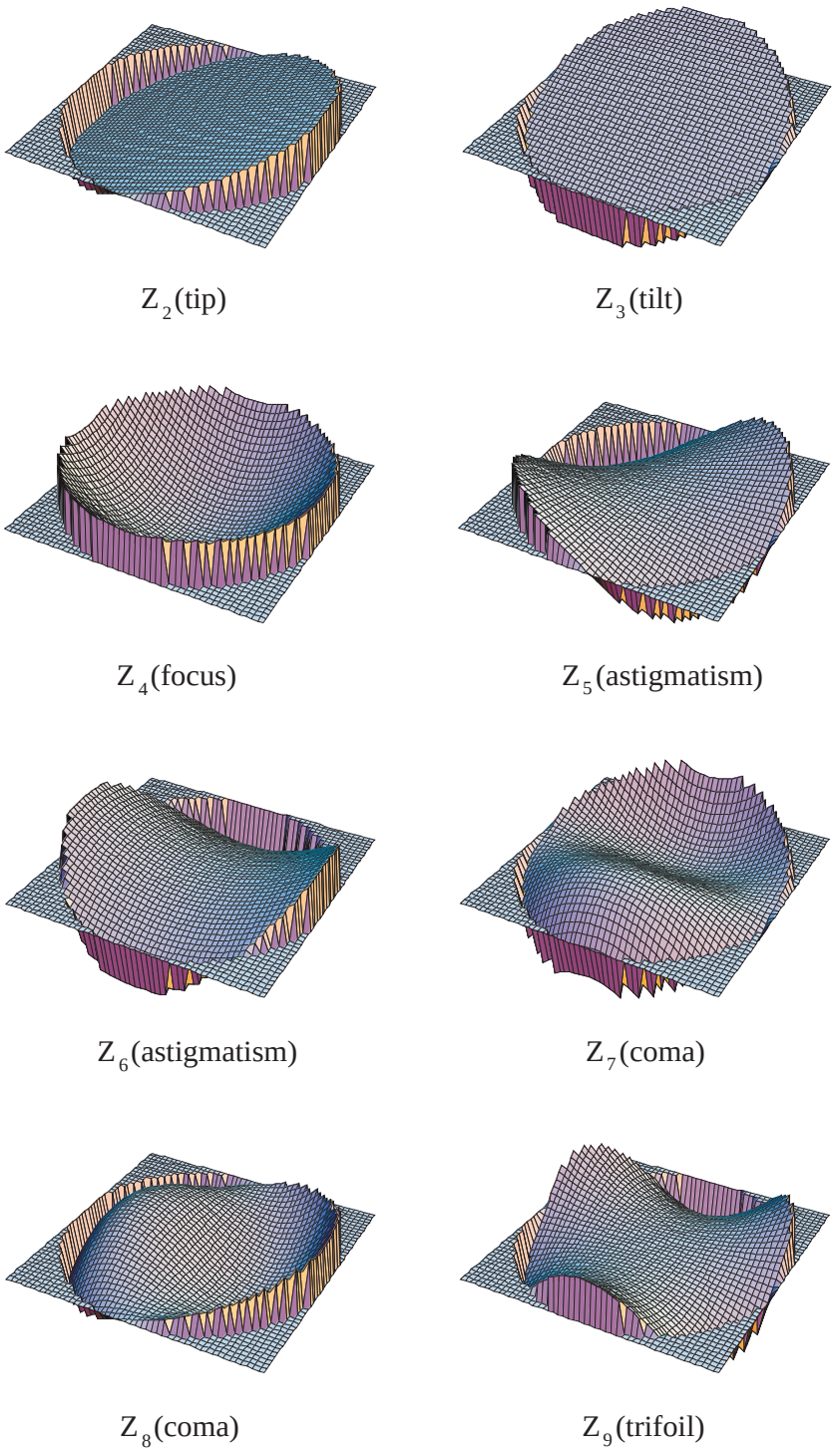

Figure 2.5: Zernike polynomials $j = 2$ to 9.

$\Delta_1 = 1.030(D/r_0)^{5/3}$	
$\Delta_2 = 0.582(D/r_0)^{5/3}$	$\Delta_2 - \Delta_1 = 0.448$
$\Delta_3 = 0.134(D/r_0)^{5/3}$	$\Delta_3 - \Delta_2 = 0.448$
$\Delta_4 = 0.111(D/r_0)^{5/3}$	$\Delta_4 - \Delta_3 = 0.023$
$\Delta_5 = 0.0880(D/r_0)^{5/3}$	$\Delta_5 - \Delta_4 = 0.023$
$\Delta_6 = 0.0648(D/r_0)^{5/3}$	$\Delta_6 - \Delta_5 = 0.023$
$\Delta_7 = 0.0587(D/r_0)^{5/3}$	$\Delta_7 - \Delta_6 = 0.0062$
$\Delta_8 = 0.0525(D/r_0)^{5/3}$	$\Delta_8 - \Delta_7 = 0.0062$
$\Delta_9 = 0.0463(D/r_0)^{5/3}$	$\Delta_9 - \Delta_8 = 0.0062$
$\Delta_{10} = 0.0401(D/r_0)^{5/3}$	$\Delta_{10} - \Delta_9 = 0.0062$
$\Delta_{11} = 0.0377(D/r_0)^{5/3}$	$\Delta_{11} - \Delta_{10} = 0.0024$

Table 2.2: The residual variance Δ_j of Kolmogorov turbulence after the first j Zernike modes are removed. The difference in the right column illustrates the strength of the single modes demonstrating that modes of equal radial order contribute the same amount to the variance.

and the coefficients a_i, using the orthogonality, are given by

$$a_i = \int_{\text{aperture}} \phi(\rho,\theta) Z_i(\rho,\theta) \rho d\rho d\theta \ . \tag{2.42}$$

The convenience of the Zernike polynomials lies in the property that, following from the Kolmogorov statistics, one can determine individually the power in every single mode like tip-tilt, astigmatism or coma. One can then immediately calculate the residual aberration after correcting a specified number of modes with an adaptive optics system. This computation was done by Noll [62]. The variance of the residual aberration is expressed as the variance of the difference between the uncorrected phase and of the removed modes. If the aberration that is due to the first J Zernike polynomials is written as

$$\phi_J(\rho,\theta) = \sum_{i=1}^{J} a_i Z_i(\rho,\theta), \tag{2.43}$$

the variance of the remaining aberrations can be expressed as

$$\Delta_J = \iint_{\text{aperture}} < [\phi(\rho,\theta) - \phi_J(\rho,\theta)]^2 > \ \rho d\rho d\theta. \tag{2.44}$$

As already noted, the variance of the phase fluctuations $< \phi^2(\rho,\theta) >$ is infinite. The analysis in terms of Zernike polynomials shows that the infinity lies in the piston term. Removing the piston term gives a finite value for the variance of the residual aberration. The residual variances in Table 2.2 are given in terms of $(D/r_0)^{5/3}$ as the Zernike polynomials are defined in the telescope aperture D. The right column of the table shows the differential improvement. It shows that the differences are constant for the same radial degree n.

For the removal of higher orders Noll gave an approximation for the phase variance [62], as

$$\Delta_J \approx 0.2944 J^{-\sqrt{3}/2} \ (D/r_0)^{5/3} \ [rad^2] \ . \tag{2.45}$$

$$\begin{pmatrix}
0.4557 & 0 & 0 & 0 & 0 & 0 & -0.0144 & 0 & 0 & 0 & 0 \\
0 & 0.4557 & 0 & 0 & 0 & -0.0144 & 0 & 0 & 0 & 0 & 0 \\
0 & 0 & 0.0236 & 0 & 0 & 0 & 0 & 0 & 0 & -0.0039 & 0 \\
0 & 0 & 0 & 0.0236 & 0 & 0 & 0 & 0 & 0 & 0 & 0 \\
0 & 0 & 0 & 0 & 0.0236 & 0 & 0 & 0 & 0 & 0 & -0.0039 \\
0 & -0.0144 & 0 & 0 & 0 & 0.0063 & 0 & 0 & 0 & 0 & 0 \\
-0.0144 & 0 & 0 & 0 & 0 & 0 & 0.0063 & 0 & 0 & 0 & 0 \\
0 & 0 & 0 & 0 & 0 & 0 & 0 & 0.0063 & 0 & 0 & 0 \\
0 & 0 & 0 & 0 & 0 & 0 & 0 & 0 & 0.0063 & 0 & 0 \\
0 & 0 & -0.0039 & 0 & 0 & 0 & 0 & 0 & 0 & 0.0025 & 0 \\
0 & 0 & 0 & 0 & -0.0039 & 0 & 0 & 0 & 0 & 0 & 0.0025
\end{pmatrix}$$

Table 2.3: Covariance matrix between the first 11 Zernike modes as given by N. Roddier. For an optimal reconstruction of the turbulent wave-front the covariance matrix should be diagonal.

Correcting an increasing number of Zernike modes changes the shape of the seeing disk in an unexpected way. Rather than narrowing the seeing disk in total, a diffraction limited spike appears on top of the seeing disk. This spike becomes more dominant with increasing number of corrected modes, until the seeing halo disappears for perfect correction. All the corrected images in Chapter 4 show this property. Since correcting the low orders does not affect r_0 very much it is intuitively understandable that the seeing disk, as λ/r_0, remains constant.

The image quality is usually expressed in terms of *Strehl ratio* that defines the peak of the point spread function normalised to the peak of the diffraction limited point spread function. The aberrations can be related to the Strehl ratio in a simple way using the Maréchal approximation [5]. If the residual variance is smaller than about $\pi^2/4$ the Strehl ratio is approximated by

$$S = \exp(-(\Delta\phi)^2) \ . \tag{2.46}$$

For a numerical example, we assume an adaptive optics system that perfectly corrects the first 10 Zernike modes. The Fried parameter is $r_0 = 60\,\mathrm{cm}$ which is typical in the near infrared and corresponds to a seeing value of 0.76″. On a 3.5-m telescope the residual variance equals $0.0401(D/r_0)^{5/3} = 0.76\,\mathrm{rad}^2$ and the Strehl ratio is 47%.

Expressing the wave-front as a Zernike polynomial the covariance matrix of the expansion coefficients $< a_i a_{i'} >$ plays an important role. This matrix can be calculated using the power spectrum of the phase fluctuations [62, 78]. It turns out that the covariance matrix is not perfectly diagonal. This means that when describing Kolmogorov turbulence with Zernike polynomials the Zernike modes are not statistically independent with the consequence that the wave-front reconstruction from the wave-front sensor data is sub-optimal. Noll found Karhunen-Loève functions to be more appropriate as they have a diagonal covariance matrix. Their disadvantage in practice is that they cannot be obtained in closed form. Using a method by N. Roddier [78] to approximate the Karhunen-Loève functions in terms of Zernike functions, Lane and Tallon have shown that when correcting more than ≈20 modes the residual aberration starts decreasing faster when using Karhunen-Loève functions [49]. In low order systems, this difference is negligible. Instead of applying Karhunen-Loève functions one can also measure the covariance matrix by using actual atmospheric data and feed this information into the reconstruction algorithm [50].

2.6.1 Temporal evolution of Zernike modes

Using the same formalism as for the analysis of the temporal characteristics of the image motion (Sect. 2.5) the temporal evolution of Zernike modes can be calculated [62, 77, 11]. The results are important for the specification of the bandwidth requirements of adaptive optics systems.

In the last section, the covariance matrix of the Zernike coefficients $< a_i a_{i'} >$ was calculated. Now we are interested in the temporal correlation of single Zernike coefficients $< a_i(t')a_i(t' + t) >$. Thus, equivalent to the calculation of the power spectrum of the image motion (Sect. 2.5) we determine a Zernike coefficient as the convolution

$$a_i(\rho, \theta) = \int_{\mathrm{aperture}} \phi(\rho', \theta') Z_i(\rho - \rho', \theta - \theta') \rho d\rho' d\theta' \; . \tag{2.47}$$

At $\rho = 0$ and $\theta = 0$ this equation is identical to the calculation of the Zernike coefficient a_i (Eq. 2.42) that can be used (see Noll [62]) to calculate the variance of the Zernike modes (see Table. 2.2). The temporal covariance follows from the spatial covariance $< a_i(\rho', \theta') \; a_i(\rho' + \rho, \theta' + \theta) >$ by using the frozen turbulence hypothesis similar to the calculation of the image motion (Eq. 2.37).

The resulting power spectra cannot be given in closed form. The numerical results were discussed by Roddier et al. [77] and Conan et al. [11], and they are briefly summarised here. The spectra show a dependence on the radial degree of the Zernike polynomial at low frequencies and a high frequency behaviour proportional to $f^{-17/3}$ that is independent of the Zernike mode. In the low frequency domain, polynomials with a radial degree of $n = 1$, Zernike tip and tilt (see Table 2.1) decrease with $f^{-2/3}$. Higher order polynomials have a slightly different characteristic depending on their azimuthal dependence; all radially symmetric polynomials go with f^0, all others with f^0, with $f^{4/3}$ or with f^2 depending on the wind direction.

The transient frequency between the high and the low frequency regions can be approximated by

$$f_t^n \approx 0.3(n + 1)\hat{v}/D, \tag{2.48}$$

where n is the radial degree of the Zernike polynomials. The transient frequency is approximately equal to the bandwidth required to correct for the Zernike mode in an adaptive optics system.

Averaging the Zernike spectra for a given radial degree shows the mean behaviour for this degree. This behaviour can also be modelled when using a multi layer model with different wind directions that is more realistic than the single layer approach [11]. The curves are displayed in Fig 2.6. It shows that for $n > 1$ the power spectra are all proportional to f^0 at low frequencies. The curves are scaled in order to give the proper variance of the single modes (see Table 2.2). It is interesting to note that at high frequencies the power spectra increase only very slowly with n. The increase in transient frequency f_t, and thus in bandwidth is partially compensated by the decrease in variance at higher radial degrees. Conan et al. [11] argue that for a given degree of correction all modes have to be corrected with approximately the same bandwidth. Otherwise the residual variance from *e.g.* the tip-tilt correction could be larger than the uncorrected variance of a high order mode. This is particularly interesting for laser guide star systems, when the tip-tilt correction is decoupled from the high order correction. If the image motion is not corrected very accurately the quality achieved with the higher order corrections is easily destroyed. We will come back to this point in Sect. 3.4.

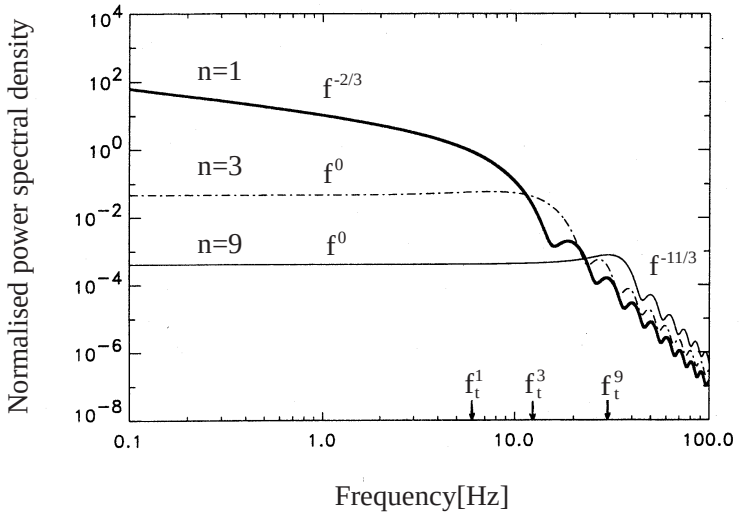

Figure 2.6: Zernike polynomial mean temporal power spectrum in a given radial degree n for n=1, 3, 9. The spectra are normalised to the turbulence variance of one polynomial of the considered radial degree: $\hat{v}/D = 10$ Hz. The asymptotic power laws and the cutoff frequencies are indicated. The figure is taken from Conan et al. [11].

It is interesting to compare the high frequency behaviour of the image motion power spectrum (Eq. 2.38) that goes with $f^{-11/3}$ to the $f^{-17/3}$ decay of the Zernike tip-tilt terms. One can show [28], that the image centroid that usually characterises the image motion is the sum of Zernike-tilt, -coma and other higher order terms. The slower decrease can then be attributed to the sum of the single power spectra with increasing transient frequencies f_t. In the low frequency region the $f^{-2/3}$ dependence of the image motion power spectrum remains unchanged as all high order terms have much smaller contributions here.

2.7 Simulation of Kolmogorov turbulence

There are two main techniques for the simulation of Kolmogorov turbulence. The first technique was presented by McGlamery in 1976 [57]. He used the statistical characteristics of the power spectrum of the phase fluctuations $\Phi(k)$ (Eq. 2.25) to create the Fourier spectrum of the turbulent phase. The difficulty arises from the very low spatial frequencies k that cannot easily be represented by a numerical array of limited size. The smallest frequency in a numerical array of size N is represented by a sine wave with a period of exactly N. Pure tilt terms that carry a very large portion of the turbulent phase fluctuations (see Sect. 2.6) cannot be simulated with this method unless very large phase screens are used of which only a very small portion is applied. In the original paper by McGlamery the phase screen was 16 times larger than the simulated aperture. This approach is not very efficient and takes a lot of computing time.

An extension to lower frequencies was presented by Lane et al. [48]. Here the fact was used that very low frequencies in the image domain show up as *subharmonics* in the Fourier domain. This method has also been extended to temporal evolution [25] and multi layer simulations [4].

A second method with a completely different approach, based on Zernike polynomials, has

been proposed by N. Roddier [78]. He starts from the Karhunen-Loève functions that can be simulated since their covariance matrix is purely diagonal. The simulated functions are then composed to form the Zernike polynomials. This makes it easy to investigate adaptive optics systems with different degrees of correction, as the corrected modes can most easily be removed in the simulation. However, if the outer scale is reduced to some finite value the covariance matrix has to be recalculated and the simulation has to be redone.

In the simulation method based on the addition of subharmonics in the power spectrum of the phase fluctuations the outer scale L_0 can be adjusted simply by limiting the lowest spatial frequency to $k > L_0^{-1}$.

Sampled representations

In conventional spectral analysis, a phase screen over a finite circular aperture with a diameter of D would be completely defined by samples of its spectrum on a rectangular grid spaced by $1/D$ [6]. A difficulty with this approach becomes apparent when one considers the effects of changing the size D of the simulated phase screen. As noted by N. Roddier [78] it is convenient to scale the resulting phase screen values by $(D/r_0)^{5/3}$ to simulate a larger aperture (or a smaller r_0)

In practice the actual sampled approximation to the Kolmogorov power spectrum is given by,

$$\Phi(i,j) = 0.023 \left(\frac{2D}{r_0}\right)^{5/3} |(i,j)|^{-11/3}, \tag{2.49}$$

where i and j are the sample indices. Note that the variation of the sample amplitude is solely a function of D/r_0.

The process of sampling numerically means to take the function $f(x)$ at N discrete points spaced equally by 1. This can be expressed mathematically by first multiplying $f(x)$ with a rectangular function of width N to represent the finite number of points, then by multiplying with a Dirac comb $\mathrm{comb}(j)$ [2] to describe the sampling process with a spacing of 1. j represents the integer values of x. Finally, in order to represent the infinite repetition of the sampled function when doing a digital Fourier transform one has to convolve the product with a second Dirac comb $\mathrm{comb}(j/N)$ that repeats the sampled function spaced by N:

$$f_j = f(x)\ \mathrm{rect}\left(\frac{x}{N}\right) \mathrm{comb}(j) \otimes \mathrm{comb}(j/N)\ . \tag{2.50}$$

Applying the discrete Fourier transform to this function, the Fourier spectrum of $f(x)$ becomes

$$\begin{aligned} \hat{f}_k &= \sum_{-N/2}^{N/2} f_j e^{2\pi\, i \frac{j\,k}{N}} \\ &= \left(\hat{f}(R) \otimes \mathrm{sinc}(\pi R) \otimes \mathrm{comb}(k/N)\right) \mathrm{comb}(k), \end{aligned} \tag{2.51}$$

where k represents the integer values of R and the sinc(.) function is defined as sinc(x) = sin(x)/x.

[2] The Dirac comb is defined as: $\mathrm{comb}(j/W) = \sum_{k=-\infty}^{\infty} \delta(j - kW)$

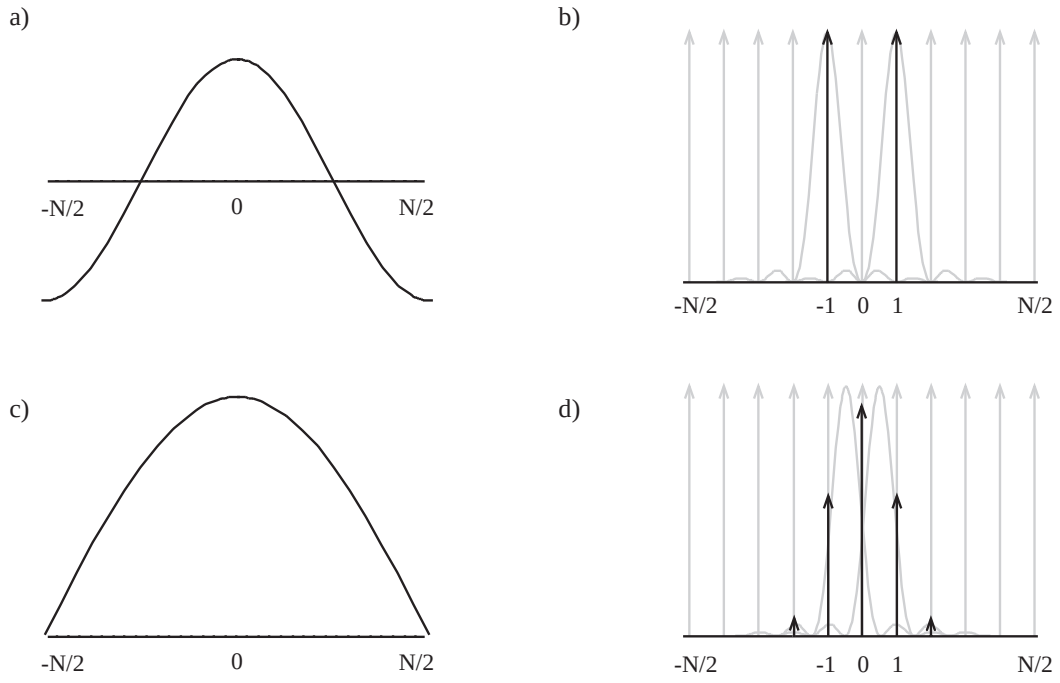

Figure 2.7: Fourier transforms of a cosine function with a period length of N (a) and $2N$ (c). The Fourier transform of the cosine in (a) produces two delta peaks at the lowest frequency (b), the Fourier transform of the function in (c) gives more than one peak (d) as described below. If this process is reversed one can produce frequencies in image space with a period length larger than the array.

The Fourier transform $\hat{f}(R)$ of $f(x)$ is convolved with the Fourier transform $\mathrm{sinc}(\pi R)$ of the rectangular function $\mathrm{rect}\left(\frac{x}{N}\right)$. The two Dirac combs make sure that the product of the convolution is sampled with a spacing of 1 and that the sampled spectrum is repeated ad infinitum with a spacing of N.

If we have a cosine function with a period of N, it is $f(x) = \cos(2\pi\frac{x}{N})$ and its Fourier transform $\hat{f}(R) = \frac{1}{2}(\delta(R+1) + \delta(R-1))$. Then the convolution product is

$$\hat{f}(R) \otimes \mathrm{sinc}(\pi\ R) = \mathrm{sinc}(\pi\ (R+1)) + \mathrm{sinc}(\pi\ (R-1))\ . \tag{2.52}$$

The multiplication of the convolution product with the Dirac comb $\mathrm{comb}(k)$ gives the classical result for the Fourier transform of two cosine functions: two δ-functions at +1 and -1 (see Fig. 2.7b) as the sinc-function has zero values exactly at the positions of the δ-functions of the Dirac comb.

In the case of a cosine with twice the period length, $f(x) = \cos(2\pi\frac{x}{2N})$ its Fourier transform is $\hat{f}(R) = \frac{1}{2}(\delta(R+1/2)+\delta(R-1/2))$ and the product of the convolution is $\mathrm{sinc}(\pi(R+1/2))+\mathrm{sinc}(\pi(R-1/2))$. In this case the multiplication with the Dirac comb $\mathrm{comb}(k)$ gives more than two values because the zero values of the sinc-functions no longer coincide with the δ-functions of the Dirac comb. The result is displayed in Fig. 2.7d.

Essentially what is required is still to generate the sampled form of the Kolmogorov spectrum, except this should be done after it has been convolved with the Fourier transform of the

aperture. Sampling at this stage incorporates the effects of frequencies with a period greater than the aperture.

Turbulence simulations with adjustable outer scale

The turbulent phase distribution $\phi(\vec{x})$ is generated by first creating Gaussian distributed random numbers with the variance of one for the real and for the imaginary part of a complex random number. These numbers are multiplied with the values of the Kolmogorov power spectrum $\Phi(|\vec{k}|)$ so that the average over many realisations forms exactly the power spectrum. The mean of the random number at a frequency $\vec{k_0}$ is set equal to the function value $\Phi(|\vec{k_0}|)$. At $|\vec{k}| = 0$ the function is set to zero which is equivalent to setting the average phase to zero. In Sect. 2.6 it was discussed that the piston term of the Zernike polynomial is solely responsible for the covariance of the phase fluctuations going to infinity. Setting the phase to zero removes the piston term without affecting the quality of the simulation with respect to the imaging process.

The square root of the power spectrum is taken to obtain the modulus $|\hat{\phi}(\vec{k})|$ of the complex Fourier transform of $\phi(\vec{x})$. A random phase $\psi(\vec{k})$ with uniform distribution is added, since only the power spectrum is defined in the Kolmogorov theory. The Fourier transform of this complex field, with the decomposition in the real and imaginary part, gives two distinct realisations of the turbulent phase distribution. This phase distribution, however, lacks the long distance correlation inherent in Kolmogorov turbulence, because the longest period that can be modelled is given by the reciprocal of the smallest frequency in the spectrum. Thus, the slope in the phase of the telescope aperture, responsible for a shift of the centroid of the speckle image, cannot be modelled unless the array size taken for the power spectrum is many times larger than the actual telescope aperture.

This restriction is circumvented by the addition of subharmonics. One has to introduce a weighting function because the square of size 1x1 around the origin (0,0) in the discrete array of the frequency space is now represented by a number of samples, i.e. the number of added subharmonics, and not only by the single sample at (0,0). We have chosen to replace the single sample by nine subsamples at (-1/3,-1/3), (-1/3,0), (-1/3,1/3) etc., each representing 1/9 of the square. Thus, each contribution has to be weighted down by 1/9. The addition of further subsamples can be done correspondingly, i.e. subdividing the remaining patch of size 1/9 at the origin again into nine subsamples each of size 1/81. The low frequencies involved in this second step are (-1/9,-1/9), (-1/9,0), (-1/9,1/9) etc. and the weighting factor is 1/81. This process can be repeated until the peak at the origin of the power spectrum is sampled satisfactorily. In our calculation, we went down to $1/3^5$ requiring a weighting factor of $(1/3^5)^2$.

The complete spectrum, including the contribution of the subharmonics to the frequencies on the discrete array, becomes

$$\begin{aligned}
\hat{\phi}_{\mathrm{conv}}(k,l) &= \sqrt{0.023}\left(\frac{2D}{r_0}\right)^{5/6}|(k,l)|^{-11/6}e^{i\psi(k,l)} \\
\hat{\phi}_{\mathrm{sub}}(k,l) &= \sqrt{0.023}\left(\frac{2D}{r_0}\right)^{5/6}\mathrm{sinc}(\pi(k-k_s))\mathrm{sinc}(\pi(l-l_s))\times \\
&\quad W(k_s,l_s)|(k_s,l_s)|^{-11/6}e^{i\psi(k_s,l_s)} \\
\hat{\phi}(k,l) &= \hat{\phi}_{\mathrm{conv}}(k,l)+\hat{\phi}_{\mathrm{sub}}(k,l), \qquad (2.53)
\end{aligned}$$

where (k,l) is the vector coordinate of the discrete array and $W(k_s, l_s)$ is the weighting factor of the added low frequency (k_s, l_s).

Temporal evolution

This simulation technique can easily be used to model the temporal evolution due to the shift of frozen turbulence [25]. The shift of the phase screen is performed in frequency space by adding a linear function to the phase of the complex spectrum. Then the spectrum becomes

$$\hat{\phi}_{\text{shift}}(k,l) = \hat{\phi}_{\text{old}}(k,l)e^{2\pi ikN_s/N} \ , \tag{2.54}$$

where N_s is the number of pixels that the phase screen has to be shifted in the direction of the coordinate k and N^2 is the size of the array. Since the shift is performed in Fourier space (k,l), N_s is not restricted to integers. Fig. 2.8 displays the temporal phase structure function for different numbers of subharmonics as well as the ideal curve for a single frozen layer (Eq. 2.29) with a coherence time $\tau_0 = 50 \ \text{msec}$ (according to the parameters of the simulation $r_0 = 0.35\,\text{m}$ and $v = 7 \ \text{m/sec}$). The addition of subharmonics gives a much better fit to the ideal curve. Thus, for a phase array only four times larger than the telescope aperture the addition of subharmonics is essential for a good estimate of the temporal phase structure function.

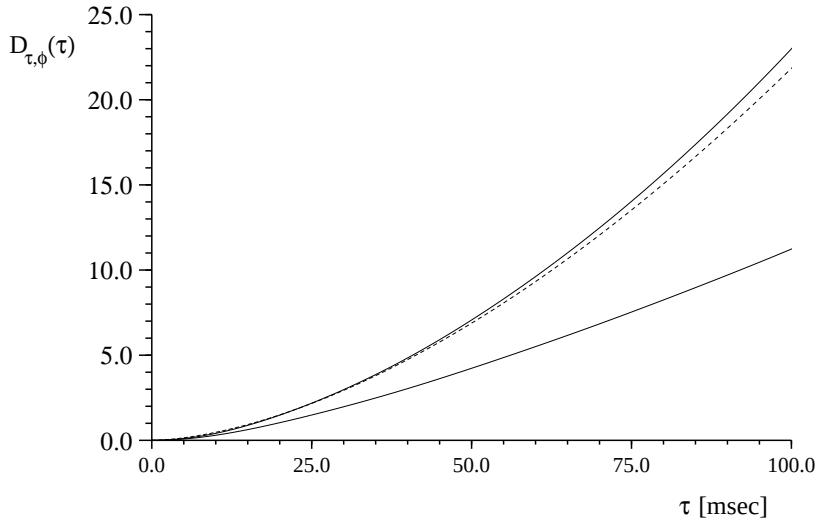

Figure 2.8: The temporal phase structure function $D_{\tau,\phi}(\tau)$ for different numbers of additional low frequencies. The dashed line represents the theoretical result. The upper solid line displays our result of two sets of additional low frequencies are used. The lower solid line shows the phase structure function without any additional low frequencies. Although the phase array that was used for the simulation is four times larger than the aperture, the addition of subharmonics is essential for a good estimate of the temporal phase structure function.

To model the statistical evolution in the phase screen rather than assuming the frozen turbulence, the random numbers in its Fourier spectrum can be evolved by using a Markov process. Starting with a phase screen created by using the procedure described in the last section, a second set of numbers $\hat{\phi}(k,l)$ is created and they are combined with the old spectrum to obtain the

result $\hat{\phi}_{\text{new}}(k,l)$ using the procedure

$$\hat{\phi}_{\text{new}}(k,l) = \frac{\hat{\phi}_{\text{shift}}(k,l) + \alpha(k,l)\ \hat{\phi}(k,l)}{\sqrt{1+\alpha^2(k,l)}}, \tag{2.55}$$

where $\alpha(k,l) = M \times 2/N \times |(k,l)|$ is the decorrelation factor that affects the velocity of the evolving process and N^2 is the size of the array. We have set α proportional to $|(k,l)|$, so that small structures related to high spatial frequencies decorrelate faster than large structures (which makes sense physically). M can be set to match the short time constant of measurements. This method has been used to model the temporal intensity correlation of speckle images [25] and it has been shown that a short time scale of the order of 10 msec, associated with an evolution of the wave-front, and a long time scale of the order of 1 sec, associated with the moving wave-front, can be distinguished.

Chapter 3

Elements of Adaptive Optics Systems

The requirements for the components of adaptive optical systems can be deduced from the discussion of imaging through turbulence in Chapter 2. The emphasis in the following is put on the requirements for wave-front sensing and reconstruction, and on the closed loop operation.

The chapter is organised as follows: we start the discussion with a closer look at image motion sensors that are called tip-tilt sensors as they measure the slope of the incident wave-front. Although these sensors seem to be very primitive since they just measure the image position many times per second they are discussed here because they form the basis for the measurement principle of the Shack-Hartmann sensor, and because all the properties of closed loop systems can be understood in a very intuitive way. Furthermore, the discussion of peak-tracking allows some interesting insight into the imaging process.

We then present three higher order wave-front sensors, the Shack-Hartmann sensor, the curvature sensor and the shearing interferometer. A short introduction to control loop theory is given and the error budget of adaptive optics systems is investigated. The principle of laser guide star systems and the deformable mirror design are discussed before, finally, methods for multi-layer adaptive optics are presented.

3.1 Tip-tilt sensors

3.1.1 Centroid tracking

The measurement of the image intensity centroid after the light has passed through either the full aperture or a sub-aperture in a Shack-Hartmann sensor provides an estimate of the wave-front slope. The centroid, or first-order moment M, of the image intensity $I(u,v)$ with respect to the x-direction in the image, is related to the partial derivative of the wave-front in the full telescope aperture by [64]

$$\begin{aligned} M_x &= \frac{\iint_{\text{image}} I(u,v)\; u\; dudv}{\iint_{\text{image}} I(u,v)\; dudv} \\ &= \frac{\lambda f}{2\pi} \iint_{\text{aperture}} \frac{\partial \phi}{\partial x}\, dxdy \;=\; \frac{\lambda f}{2\pi} \int_0^1 \int_0^{2\pi} \frac{\partial \phi}{\partial x} \rho d\rho d\theta \;, \end{aligned} \tag{3.1}$$

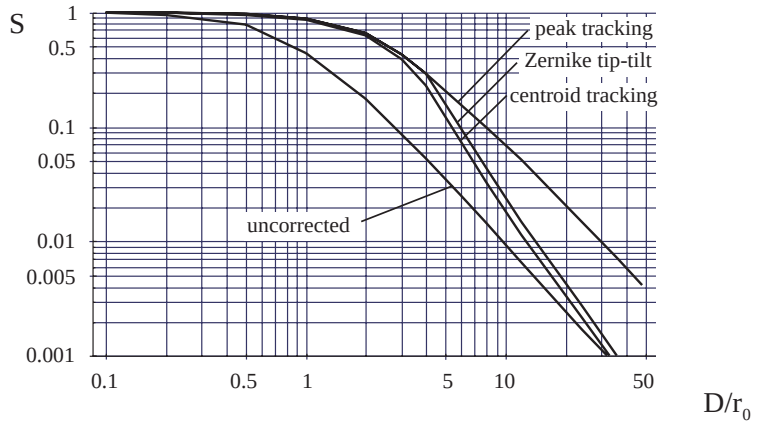

Figure 3.1: Calculated Strehl ratios of tip-tilt corrected images using peak tracking, Zernike tip-tilt tracking and centroid tracking. For comparison the Strehl ratios for uncorrected images are displayed, too. Tip-tilt tracking achieves more than 10% Strehl ratio up to $D/r_0 = 6$, what corresponds to a seeing of 0.76″ at 2.2 μm on a 3.5-m telescope. Beyond $D/r_0 = 10$, only peak tracking improves the image noticeably. Centroid tracking, being affected by Zernike tip-tilt and coma, performs a little bit worse than pure Zernike tip-tilt tracking. The latter can be realised by stopping down the beam in the tip-tilt camera to about 80% of the full aperture.

with f the telescope focal length. Taking the derivatives of the Zernike polynomials we find [28] that

$$M_x \propto a_2 + \sqrt{2}\, a_8 + \ldots , \tag{3.2}$$

where a_2 is the tilt term and a_8 is the coma term of the Zernike polynomials in Table 2.1. Since the optimal tip-tilt correction is done with the Zernike tip-tilt terms alone, using the image centroid over-compensates for coma. It was discussed in Sect. 2.6 that Zernike coma is balanced in such a way that the aberration is minimised. Affecting this balance by tilting the wave-front as a result of the image centroid measurement increases the wave-front variance by an amount that is twice as large as the one of the unaffected coma[1]. However, the influence of the coma term is relatively small. With the residual variance of the phase ϕ due to coma ($0.0062(D/r_0)^{5/3}$, see Table 2.2), the additional phase variance from both coma terms a_7 and a_8 is

$$\sigma^2_{\mathrm{coma}} = 2(0.0062 + 0.0062)(D/r_0)^{5/3}[\mathrm{rad}^2]. \tag{3.3}$$

Adding this expression to the variance $\sigma^2_{\mathrm{h.o.}} = 0.134(D/r_0)^{5/3}$ that remains after perfect tip-tilt correction (see Table 2.2), the residual phase variance after tip-tilt correcting by tracking the image centroid is

$$\sigma^2_{\mathrm{centroid}} = \sigma^2_{\mathrm{h.o.}} + \sigma^2_{\mathrm{coma}} = 0.158(D/r_0)^{5/3}[\mathrm{rad}^2]. \tag{3.4}$$

This expression was derived in [22] with a minor numerical inaccuracy. Using the simulation method for atmospheric turbulence described in Sect. 2.7 we calculated Strehl ratios for varying seeing conditions displayed in Fig. 3.1. In the K band at 2.2 μm, r_0 is 60 cm when the seeing

[1] Tilting the wave-front to compensate for $\sqrt{2}\, a_8$ means to add a term $\sqrt{2}\, 2\rho$ to the Zernike coma a_8. The wave-front variance of the tilted coma is three times larger than the balanced Zernike mode. That means one has to add two times the variance of that mode.

is 0.76″. For a telescope diameter of 3.5 m it is $D/r_0 = 6$, and the Strehl ratio achievable with centroid tracking is then 7% (see Fig. 3.1). This is more than a factor of two improvement over the uncorrected case with $S = 2.6\%$. However, for slightly better seeing of 0.6″ at 2.2 μm, corresponding to $r_0 = 75$ cm (and $D/r_0 = 4.7$), the uncorrected Strehl ratio is 4% and centroid tracking improves the Strehl ratio by a factor of three to $S = 13\%$. This is illustrated by the slope of the curves in Fig. 3.1: The Strehl ratio for centroid tracking decreases faster with D/r_0 than the Strehl ratio of the uncorrected image. Thus, tip-tilt corrected images are more sensitive to varying seeing conditions than uncorrected images. Short time seeing variations that are barely noticed in the uncorrected image can cause a measurable peak intensity variation in the tip-tilt corrected image.

If the Zernike tip-tilt coefficients are determined properly, the variance of the wave-front phase is given by $\sigma^2_{\text{h.o.}}$ alone, and compared to centroid tracking, the achievable Strehl ratios are improved (see Fig. 3.1). Usually this measurement requires a high order wave-front sensor. However, by changing the integration limits of the image centroid calculation in Eq.(3.1) one obtains an unbiased estimate of the wave-front slope [22]. If the telescope aperture is stopped down to about 80% (depending on the central obscuration) of the full diameter the image centroid calculation in Eq.(3.1) becomes independent of the coma term a_8. Since the guide star has to be only about twice as bright as for the full aperture this method works on all but the faintest guide stars. The tip-tilt system of the UKIRT[2] telescope is equipped with an aperture stop filter wheel with apertures stops of different size to measure the unbiased wave-front slope [27]. Simulations have shown that for 0.76″ seeing the peak intensity of the Zernike tip-tilt corrected image is improved to a Strehl ratio of 9.5% instead of 7% for centroid tracking. Fig. 3.1 illustrates the improvement that can be achieved.

3.1.2 Peak tracking

Peak tracking, better known as shift-and-add for image post-processing, provides a higher Strehl ratio than centroid tracking. This has been demonstrated by Christou in a comparative study [8], and this is well known to observers who use shift-and-add.

In the terminology of wave-fronts, the better performance of peak tracking can be explained by using an error measure that takes the periodicity of the light wave into account [21]. Determining the tip-tilt term of a Zernike polynomial means minimising the residual aberration regardless of the wavelength. The practical consequence is that one can use a tip-tilt sensor in the visible for observations in the infrared.

However, if the tip-tilt term is determined by minimising the residual aberration modulo 2π we find that this tip-tilt term coincides with the position of the brightest speckle. The general relationship between the complex amplitude in the telescope pupil and the intensity distribution in the focal plane illustrates this effect. The image intensity is related to the phase $\phi(\vec{x})$ in the pupil plane through a Fourier transform (see Sect. 2.1):

$$I(\vec{u}) = \left| \int_{\text{aperture}} \exp(i\phi(\vec{x})) \exp(2\pi i \vec{x}\vec{u}) \, d\vec{x} \right|^2 . \tag{3.5}$$

[2]UKIRT is the United Kingdom Infra Red Telescope on Mauna Kea, Hawaii. It has a 3.8-m primary mirror.

Shifting the image by a distance $\vec{s}$ is equivalent to adding a linear term, the wave-front tilt $2\pi\vec{s}\vec{x}$ to the phase. The intensity at the image center $\vec{u} = 0$ as a function of the wave-front tilt is then

$$\begin{aligned} I_{\vec{s}}(0) &= \left| \int_{\text{aperture}} \exp(i(\phi(\vec{x}) + 2\pi\vec{s}\vec{x}) \exp(2\pi i\vec{x}\vec{u})|_{\vec{u}=0}\, d\vec{x} \right|^2 \\ &= \left| \int_{\text{aperture}} \exp(i(\phi(\vec{x}) + 2\pi\vec{s}\vec{x}))\, d\vec{x} \right|^2 . \end{aligned} \tag{3.6}$$

We can now try to maximise the image intensity by finding the appropriate shift vector $\vec{s}$. Since shifting the image means tilting the wave-front the variance of the new phase distribution $\phi(\vec{x}) + 2\pi\vec{s}\vec{x}$ is different from the old one $\phi(\vec{x})$. The image intensity is maximised by minimising the phase variance [39]. Usually, this minimisation is done by minimising the absolute error

$$E_{\text{abs}} = \int_{\text{aperture}} (\phi(\vec{x}) + 2\pi\vec{s}\vec{x})^2\, d\vec{x}. \tag{3.7}$$

This is another way of formulating the Zernike polynomials; the Zernike tip and tilt terms are defined such that this error sum is minimal if the components of the vector $\vec{s}$, s_x and s_y, are equal to a_2 and a_3. For high quality optical systems with small aberrations this approach is appropriate and, if the variance is smaller than about $\pi^2/4$, the Maréchal approximation can be used to calculate the Strehl ratio [5]. Thus, minimising E_{abs} means to maximise the Strehl ratio .

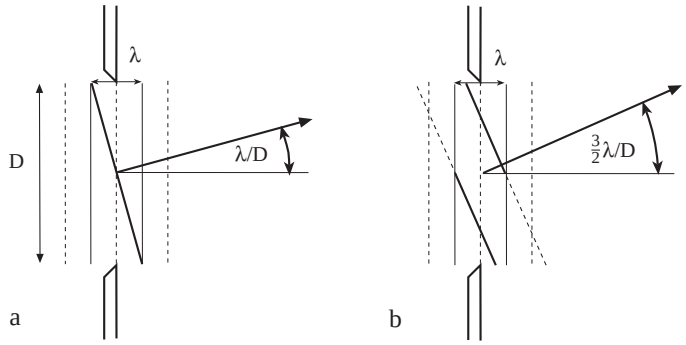

Figure 3.2: The angular direction of the first minimum (a) and the first maximum (b) of the diffraction pattern of a rectangular slit. The tilted wave-front and the incoming plane wave are displayed in the aperture. In (a), the tilted wave lies within an interval of one λ of the incoming wave. In (b), the tilted wave-front extends beyond the one λ interval and the effective part, the wave-front modulo λ, is displayed by the solid line. If the intensity in the direction of the diffraction angle is interpreted as an aberration compared to the incoming plane wave then the aberration of the wave-front modulo λ determines the intensity.

However, if the aberrations are large there might be areas in the aperture where the aberration $\phi(\vec{x}) + 2\pi\vec{s}\vec{x}$ is larger than 2π. Then the minimum of E_{abs} usually does not coincide with the peak intensity. In Eq.(3.6) only the difference modulo 2π determines the value of the complex exponential under the integral. Therefore it is appropriate to minimise an error function that weights the aberration modulo 2π:

$$E_{\text{eff}} = \int_{\text{aperture}} (mod_{2\pi}(\phi(\vec{x}) + 2\pi\vec{s}\vec{x}))^2\, d\vec{x}. \tag{3.8}$$

The simple example of a plane wave incident on a rectangular slit of width D illustrates the effect. Fig. 3.2 displays the wave-front modulo 2π in the slit aperture when the diffraction pattern has its first minimum (in the angular direction λ/D) and its first maximum (at $\frac{3}{2}\lambda/D$). Tilting the wave by $2\pi s$ in our formalism means to calculate the angular distribution of the diffraction pattern as a function of s. For $s = 0$ the error sum E_{eff} (as well as E_{abs}) is zero and the intensity is at a maximum. Increasing the tilt angle increases the absolute error constantly. The effective error first increases too, and the intensity decreases until the first intensity minimum is reached for the diffraction angle λ/D, where E_{eff} has its first maximum of $\pi^2/3$ (see Fig. 3.3). Fig. 3.2 shows that the peak-to-valley value of the aberration is then λ. Increasing the tilt further reduces the effective error until at the position of the first sidelobe of the diffraction pattern the effective error reaches a local minimum at $\frac{3}{2}\lambda/D$. One has to be very careful when adjusting a constant ϕ_0 that can be added to the phase. This constant does not change the value of the intensity as $\exp(2\pi\phi_0)$ can be put in front of the integral in Eq.(3.5). The variance calculation, however, is affected by the average value of the wave-front modulo 2π. The constant ϕ_0 has to be set such that the average is zero and the aberration is still in the range $\pm\pi$. In Fig. 3.2b the proper phase distribution for a tilt corresponding to the first sidelobe is shown in the slit aperture.

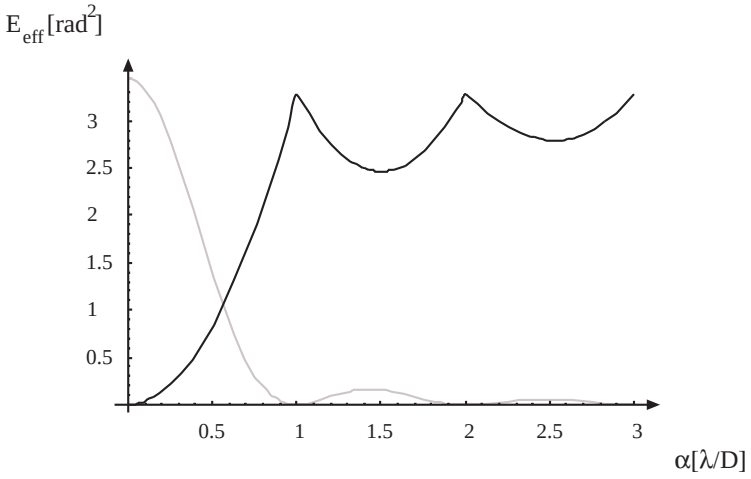

Figure 3.3: The effective error, *i.e.* the sum of the aberration modulo 2π for the diffraction at a rectangular slit is displayed by the solid line. The gray line is the intensity distribution in the diffraction pattern. The maxima of the error sum coincide with the minima of the intensity pattern and vice versa.

Increasing s beyond the first maximum enlarges E_{eff} before it is reduced again at the second side lobe. Thus, the intensity distribution in the diffraction pattern can be explained in terms of the distribution of maxima and minima in the effective error sum E_{eff}.

If positioning the brightest speckle at the image center provides the global minimum of the error sum E_{eff}, then every single speckle as a local intensity maximum represents a local minimum of the error sum. Fig. 3.4 demonstrates this effect with a simulated speckle pattern with $D/r_0 = 24$ corresponding to a seeing of 0.7″ and an $r_0 \approx 15\,\text{cm}$ in the visible on a $3.5\,\text{m}$ telescope. Every pixel of the speckle pattern in Fig. 3.4a is taken as shift vector $\vec{s}_i$. Then the error sum of the effective aberration E_{eff} is calculated and its square is displayed in Fig. 3.4b, where

the coordinates represent the shift $\vec{s}_i$. The agreement between the speckle as local maxima and the minima of the error sum is extremely good. Fig. 3.4c shows the conventional error sum E_{abs} of the absolute aberration. There is only one minimum of the error sum over the whole image. The shift that corresponds to this minimum is the best conventional fit of a slope to the wave-front, which is identical to the tip-tilt term of a Zernike polynomial.

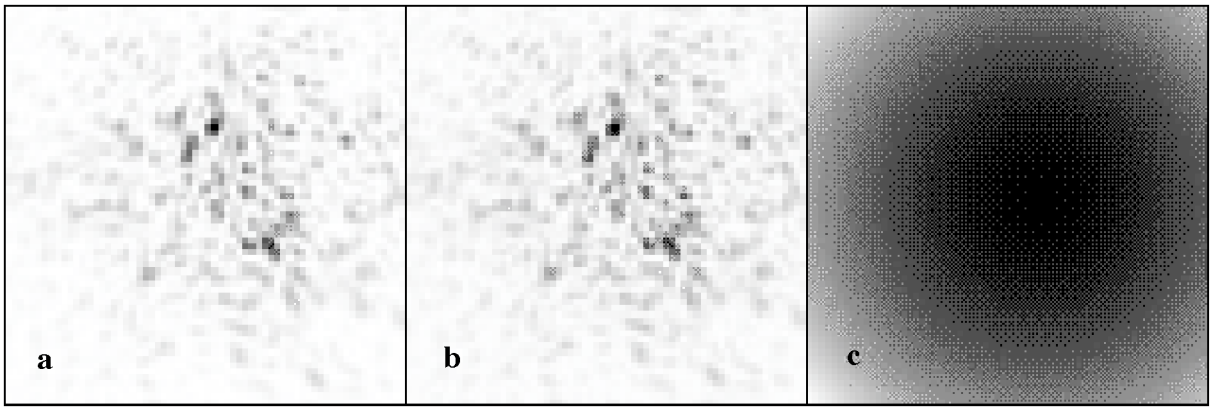

Figure 3.4: (a) Speckle pattern with $D/r_0 = 24$, (b), (c) the sums of the remaining wave-front aberrations. The value at each coordinate in (b) and (c) represents the error sum if the corresponding pixel of (a) is shifted to the image center. In (b) the square of the effective aberration, i.e. the aberration modulo 2π, is shown, and in (c) the absolute aberration is taken. It is readily apparent that the minima of the error sum in (b) correspond to the positions of the speckles in (a). The absolute minimum of the error sum in (c) indicates the position of the centroid of the speckle pattern.

An empirical formula for the residual variance of the wave-front phase when peak-tracking is used to stabilise the image is derived from the values of the simulation [21] and it reads as

$$\sigma^2_{\text{peak}} = \frac{\pi^2}{3}\frac{0.062(D/r_0)^{5/3}}{1+0.062(D/r_0)^{5/3}}[\text{rad}^2]. \tag{3.9}$$

The same formalism can be applied to include focus. The shift of the intensity pattern along the optical axis is equivalent to defocusing which is considered by a square term $g|\vec{x}|^2$ in the phase. Now the error measure that has to be minimised reads as

$$E^f_{\text{eff}} = \int_{\text{aperture}} \left(mod_{2\pi}\left(\phi(\vec{x}) + 2\pi(\vec{s}\vec{x} + g|\vec{x}|^2)\right)\right)^2 d\vec{x}. \tag{3.10}$$

In simulations of tip-tilt systems and of tip-tilt and focus systems, it has been shown that the relative improvement of the image quality in the visible, when $D/r_0 \gg 1$, is remarkable if peak tracking is used [21]. In a seeing of of 0.7″ in the visible (displayed in Fig. 3.4) peak tracking and focus correction increases the peak intensity tenfold.

For $D/r_0 < 3$, corresponding to a seeing better than 0.4″ at 2.2 μm on a 3.5-m telescope, the Strehl ratio for peak tracking and for centroid tracking are about the same, and the position of the brightest speckle and the centroid coincide (see Fig. 3.1). Then, the residual aberration is smaller than 2π and peak tracking gives no advantage over centroid tracking.

Fig. 3.1 displays the superior performance of peak tracking when D/r_0 increases. For $D/r_0 = 6$, the seeing is 0.76″at a wavelength of 2.2 μm on a 3.5-m telescope. Then, the Strehl ratio is 15%, *i.e.* 6 times the uncorrected value. However, peak tracking requires a pixel size in the tip-tilt sensor that allows Nyquist sampling of the speckle pattern. As for $D/r_0 = 6$ roughly 12^2 pixels are required, the guide star has to be at least 30 times brighter than for centroid tracking with a quadrant detector, reducing the sky coverage drastically.

This concept can be extended to higher orders than tip-tilt and focus. It is superior to the conventional error measure as long as the peak-to-valley value of the residual aberration is larger than 2π. However, as it is the goal of most adaptive optics systems to reduce the error to much less than $\pi^2/4$ which is equivalent to a Strehl ratio better than 10% the conventional error measure can be used without loss in performance.

3.1.3 Measurement noise

The residual variances of the wave-front phase for perfect centroid or peak tracking are given in Eq.(3.4) and Eq.(3.9). To derive these expressions we assumed that the image centroid and the peak were determined error free. For low light levels one has to consider two types of measurement errors that deteriorate the performance of the correction system: the photon noise σ_{ph}^2 and the read noise σ_r^2. These variances are given as variance of the wave-front phase due to photon noise and to read noise of the intensity measurement. Primot derived these quantities assuming that the seeing disk is approximately Gaussian and that it is centered [64].

Then the form of the phase variance due to signal photon noise is [80]

$$\sigma_{\rm ph}^2 = \frac{\pi^2}{2}\frac{1}{N_{\rm ph}}\left(\frac{\alpha_0 D}{\lambda}\right)^2 [\mathrm{rad}^2], \tag{3.11}$$

where N_{ph} is the total number of photoelectrons, α_0 the angular size of the image and D the diameter of the aperture. In the diffraction limited case the image size α_0 is equal to λ/D and the variance is proportional to $1/N_{ph}$. In the case of a seeing limited point source one can write

$$\sigma_{\rm ph}^2 = \frac{\pi^2}{2}\frac{1}{N_{\rm ph}}(D/r_0)^2. \tag{3.12}$$

The wave-front variance as a function of the detector read noise σ_d can be written in a similar fashion [80]

$$\sigma_r^2 = \frac{\pi^2}{3} f^2 N_{\alpha_0}^2 \left(\frac{\sigma_d}{N_{\rm ph}}\right)^2 \left(\frac{D}{r_0}\right)^4 [\mathrm{rad}^2], \tag{3.13}$$

with $N_{\alpha_0}^2$ the total number of pixels per Airy disk, and f the quotient between the area on the detector used for the centroid calculation or the peak search, and the area of the seeing disk. If for instance the (square) area on the detector is $(2'')^2$ in 0.7″ seeing the quotient f is 10. The case of background photo noise is treated very similarly by replacing the detector read noise σ_d by the background noise σ_b [80].

As already noted the wave-front sensor usually operates in the visible whilst the science camera works in the infrared. In order to convert the wave-front variances to the infrared they have to be multiplied by $(\lambda_{\rm WFS}/\lambda_{\rm IR})^2$. The number of pixels per Airy disk is determined by the optical

design of the wave-front sensor. As the square of this number goes into the variance calculation it should be kept small.

The sum σ_{st}^2 of all static errors, the error budget, reads as

$$\sigma_{\rm st}^2 = \sigma_{\rm fit}^2 + \sigma_{\rm ph}^2 + \sigma_r^2, \tag{3.14}$$

where σ_{fit}^2 is $\sigma_{\rm centroid}^2$ for centroid tracking or $\sigma_{\rm peak}^2$ for peak tracking. It is interesting to note that the variance due to read noise ($\sigma_r^2 \propto (D/r_0)^4$) depends much stronger on the seeing conditions than $\sigma_{fit}^2 \propto (D/r_0)^{5/3}$ and $\sigma_{\rm ph}^2 \propto (D/r_0)^2$.

To have a better idea of the implications of the single error sources on the error budget we discuss a numerical example for centroid tracking. The tip-tilt sensor is assumed to work in the visible at $0.5\,\mu{\rm m}$ and the science camera in the infrared at $2.2\,\mu{\rm m}$. The table summarises the relevant seeing parameters.

Wavelength	$0.5\,\mu{\rm m}$	$2.2\,\mu{\rm m}$
Seeing	$1''$	$0.76''$
D/r_0	35	6

The pixel size is $0.72''$, *i.e.* $N_{\alpha_0} = 1/24$ (since the FWHM is $0.03''$ at $0.5\,\mu{\rm m}$) and the size of the detector area used for the centroid calculation is $3''$, *i.e.* $f = 10$. The error budget can now be written as

$$\begin{aligned}\sigma_{\rm st}^2 &= 0.16\ 6^{5/3} + (\frac{\lambda_{\rm WFS}}{\lambda_{\rm IR}})^2 \left(\frac{\pi^2}{3} f^2 (\frac{1}{24})^2 \left(\frac{\sigma_d}{N_{\rm ph}}\right)^2 35^4 + \frac{\pi^2}{2}\frac{1}{N_{\rm ph}} 35^2\right) \\ &= 3.16 + \left(210\frac{\sigma_d}{N_{\rm ph}}\right)^2 + \frac{312}{N_{\rm ph}}. \end{aligned} \tag{3.15}$$

If it is the goal that the noise adds less than 10% to the fitting error $\sigma_{\rm centroid}^2$ the number of photons has to be $N_{\rm ph} \approx 2000$ if the detector read noise is $\sigma_d = 5$ which is typical for CCD cameras. Taking the atmosphere, the telescope mirror coating and the quantum efficiency of CCD cameras into account one finds that a $m_V = 15$ star provides about 2000 photoelectrons in $20\,{\rm msec}$ on a $4\,{\rm m}$-class telescope [28]. The performance of the tip-tilt system at the UKIRT telescope with similar specifications confirms this calculation [27].

3.2 Wave-front sensing

Three different types of higher order wave-front sensors are discussed in this section. Starting with the Shack-Hartmann sensor this is most commonly being used since it is conceptually simple and its properties are well understood, the curvature sensor is described next. This technique was introduced by F. Roddier in 1988 [74]. The adaptive optics system installed at the CFHT[3] in 1996 was the first large system to use a curvature sensor, and it has shown excellent performance.

[3]The CFHT is the Canada-France-Hawaii Telescope on Mauna Kea, Hawaii. It has a 3.6-m primary mirror.

The obstacle preventing the wide spread use of this technique is the very complicated theory behind the concept. Also, according to Roddier, it is suited particularly for adaptive optics systems correcting less than 40 modes [76].

The last wave-front sensor to be discussed briefly is the shear interferometer. This sensor was used especially in military systems. There is no civilian adaptive optics system that employs a shear interferometer as wave-front sensor.

3.2.1 Shack-Hartmann sensor

The Shack-Hartmann sensor divides the telescope aperture into an array of smaller subapertures, and a lenslet array is used to produce multiple images (see Fig. 3.5). The centroid displacement of each of these subimages gives an estimate of the average wave-front gradient over the subaperture [64] that can be calculated using Eq.(3.1). The important consequence is that the Shack-Hartmann sensor is achromatic – the image movement is independent of wavelength – and that extended sources can be used as long as they fit into the subimage boundary.

In practice, a Shack-Hartmann sensor is built by putting a lenslet array in the reimaged telescope pupil. The subimages from each subaperture are imaged onto a CCD camera. The size of the subimages has to be chosen such that the image motion even of extended sources does not drive the images outside of the subimage boundary. The single axis rms image motion can be calculated from the variance in Eq.(2.36); it is

$$\Delta\theta = 0.41(\lambda/r_0)(d/r_0)^{-1/6}[\mathrm{arcsec}], \tag{3.16}$$

where d is now the diameter of the subaperture and λ/r_0 is the seeing in arcsec. $\Delta\theta$ is between 0.2 and 0.4 times the seeing and the peak-to-valley image motion about six times this value. Thus, the size of the subimage should be at least three times the seeing. If the size of the extended sources is likely to be larger than this the subimage size has to be chosen accordingly. Even the solar surface can be used for wave-front measurement if a field stop and image correlation techniques are used to determine the wave-front gradients. If the subimage size is very large several sources can be observed independently allowing for isoplanatic effects to be measured (see Sect. 3.7) [23].

The perfect information about the position of the subapertures with respect to the telescope aperture allows one to calculate the interaction matrix Θ_{sh} linking the image positions with the modes of the wave-front polynomial. However, this information might be difficult to obtain. Therefore a different approach was realised in ALFA. Instead of calculating the subimage centroid positions for the Zernike modes (see the following example) the deformable mirror is driven to form these modes and the subimage centroids are then measured. This method is discussed in larger detail in Sect. 4.2.

As an example a 2×2 Shack-Hartmann sensor is modelled, subdividing the aperture into four quarter circles [29]. The integration in Eq.(3.1) has to be performed over the subapertures, i.e. for $\rho = 0$ to 1 and $\theta = 0$ to $\pi/2$ for the first subaperture. The centroid displacement in x for the first subaperture therefore becomes

$$M_{x1} = \frac{\pi}{2}a_2 + \frac{4}{\sqrt{3}}a_4 + \frac{2}{3}\sqrt{6}(a_5 + a_6) + \frac{3}{2}\sqrt{2}(a_7 + a_9) + \frac{\pi}{\sqrt{2}}a_8 + \dots\ .$$

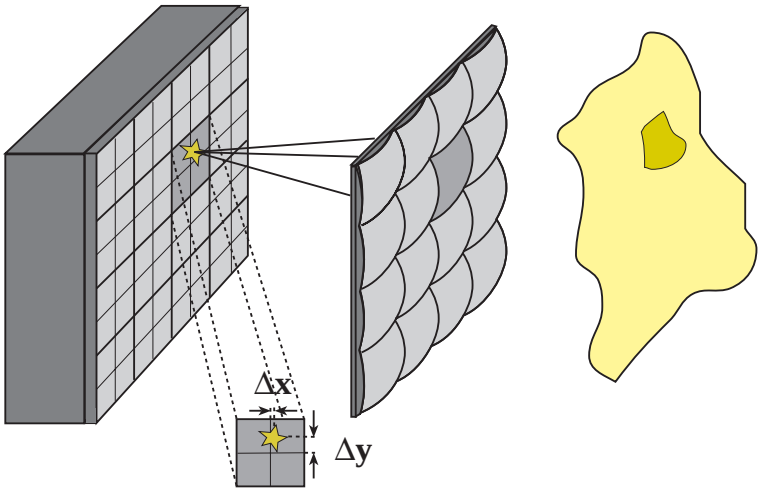

Figure 3.5: Measurement principle of a Shack-Hartmann sensor. The incoming aberrated wave is subdivided by the lenslet array and the image centroid in every subimage is shifted according to the average wave-front slope over the subaperture formed by the lenslet.

As each lenslet yields two measurements, in x and in y, one obtains a total of eight gradients. Usually this system of eight equations is written in matrix form

$$\begin{pmatrix} M_{x1} \\ M_{y1} \\ M_{x2} \\ M_{y2} \\ . \\ . \\ M_{y8} \end{pmatrix} = \Theta_{\mathrm{sh}} \begin{pmatrix} a_1 \\ a_2 \\ a_3 \\ a_4 \\ . \\ . \\ a_8 \end{pmatrix} \tag{3.17}$$

with $\vec{M}$ the vector containing the measured gradients, $\vec{a}$ the vector containing the coefficients of the Zernike polynomial and Θ_{sh} the interaction matrix. The optimal number of Zernike coefficients estimated from a 2×2 Shack-Hartmann sensor is not 8 but 6 because the Zernike coefficients are not statistically independent. The non-diagonal covariance matrix (Table 2.3) shows their interdependencies. Thus, the residual aberration starts increasing again (see Table 3.1) [47]. As discussed in Sect. 2.6, with Karhunen-Loève functions this increase is less severe, however, with an increase in computational effort. Using the *a priori* knowledge about the correlation of the Zernike coefficients a_i it is possible to reconstruct the wave-front to a higher precision [50].

The measurement errors of the image centroid due to photon noise and read noise were derived in Sect. 3.1.3. Since the reconstruction of the phase is made through a linear process the noise of each subaperture measurement propagates linearly with

$$\sigma^2_{\mathrm{noise}} = P(J)\left(\sigma_r^2 + \sigma^2_{\mathrm{ph}}\right), \tag{3.18}$$

where P(J) is the factor that describes the error propagation as a function of the number J of corrected modes. It depends on the properties of the system, like sensor and mirror geometry,

Zernike mode compensated	3	4	6	8	9
Theoretical $(D/r_0)^{5/3}$	0.134	0.111	0.065	0.053	0.046
Achieved $(D/r_0)^{5/3}$	0.15	0.13	0.088	0.093	0.106

Table 3.1: The residual phase variance σ^2 in units of $(D/r_0)^{5/3}$ after using a standard least-squares method described by Primot[64] to solve Eq.(3.17). The theoretical results for perfect compensation were given by Noll [62]

number of sensors and actuators etc. Rigaut has derived an expression for Zernike modes [72] that is given as

$$P(J) \approx 0.34 \ln(J) + 0.10. \tag{3.19}$$

The error budget of a Shack-Hartmann sensor correcting for J modes can now be written as

$$\sigma^2_{\rm st} = \Delta_J + P(J)\left(\sigma^2_r + \sigma^2_{\rm ph}\right), \tag{3.20}$$

where Δ_J is the wave-front fitting error after removing the first J Zernike modes given in Eq.(2.44). The implications of the dynamic behaviour of the turbulence will be discussed in Sect. 3.4.

3.2.2 Curvature sensor

The idea of a curvature sensor was first discussed by Roddier [74]. It relies on measuring the intensity distribution in two different planes on either side of the focus using the normalised difference between the distributions. This difference is a measure for the curvature of the wave-front in the telescope pupil and for the wave-front tilt at the aperture edge. The principle is sketched in Fig. 3.6. The two intensity distributions are recorded in the two planes P_1 and P_2, a distance δ from the telescope focal plane. The figure displays the effect of a local curvature of the wave-front: the curved wave-front leads to a local excess of illumination in plane P_1 and to a lack of illumination at the corresponding position in P_2 as the light is spread out. The two planes of observation have to be far enough apart so that geometrical optics is a good approximation, *i.e.* $(f-\delta)\lambda/r_0 \leq r_0\delta/f$.

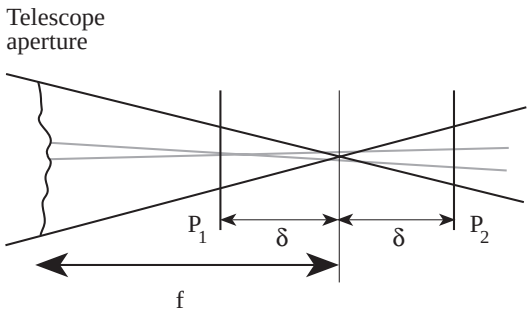

Figure 3.6: Principle of the curvature sensor. The gray lines show the rays from a curved part of the wave-front that form a focus before the focal plane, leading to a local increase in intensity in plane P_1 and a decrease in P_2.

However, for extended sources and different degrees of correction the situation becomes more complicated. The local resolution of the wave-front measurement, given by the size of the subapertures in the Shack-Hartmann sensor, is determined by the size of the blur that is caused *e.g.* by the small piece of curved wave-front in Fig. 3.6. If the separation δ is too small this blur is too small to be measured. Also, if the detector pixels are too large this blur cannot be resolved and the mode corresponding to aberrations of this size cannot be measured. Thus, the separation δ and the pixel size have to be adjusted according to the required degree of correction. An extended source has the same effect as a larger seeing disk, and the separation has to be adjusted accordingly. The conclusion is: for the measurement of high orders, δ must be larger than for low orders, and for extended sources, δ must be larger than for point sources [80].

The normalised difference between the two intensity distributions is [74]:

$$c(x,y) = \frac{I_+(x,y) - I_-(x,y)}{I_+(x,y) + I_-(x,y)} \propto \left[\frac{\partial}{\partial\rho}\phi(\rho,\theta)\Psi - \nabla^2\phi(\rho,\theta)\right], \tag{3.21}$$

where $\nabla^2 = \frac{1}{\rho}\frac{\partial}{\partial\rho}(\rho\frac{\partial}{\partial\rho}) + \frac{1}{\rho^2}\frac{\partial^2}{\partial\theta^2}$ is the Laplacian operator representing the curvature of the wave-front. The wave-front radial tilt $\frac{\partial\phi}{\partial\rho}$ has to be weighted by an impulse distribution Ψ around the pupil edge. The advantage of the curvature measurement over the slope measurement in a Shack-Hartmann sensor is the very low correlation of the local curvature over the wave-front. Measuring statistically independent signals gives a better estimate of the wave-front [76]. Eq.(3.21) is the irradiance transport equation for paraxial beam propagation providing a general description of incoherent wave-front sensing methods [75].

That means in an f/35 beam on a 3.5-m telescope for $\lambda = 2.2\,\mu\mathrm{m}$ and $r_0 = 0.6\,\mathrm{m}$ the planes should be $\delta = \pm 90\,\mathrm{mm}$ apart.

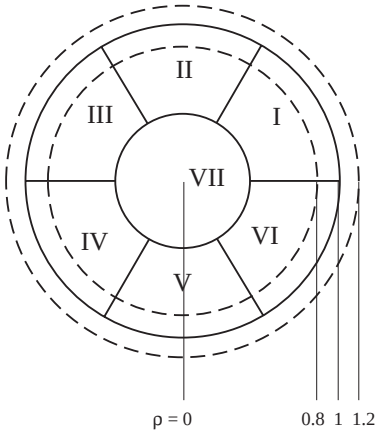

Figure 3.7: Sampling geometry for a low order curvature sensor. The illumination is integrated over each segment. The width of the impulse distribution Ψ is displayed by the dashed lines.

We have modelled a 7-element curvature sensor displayed in Fig. 3.7 [29]. Using the geometrical optics approximation $(f-\delta)\lambda/r_0 \leq r_0\delta/f$ one finds that δ is $\pm 90\,\mathrm{mm}$ for a f/35 beam on a 3.5-m telescope for $\lambda = 2.2\,\mu\mathrm{m}$ and $r_0 = 0.6\ \mathrm{m}$. As we model a low order system we used $\delta = \pm 20\,\mathrm{mm}$. The signal in Eq.(3.21) has to be integrated over the area of each segment where the width of the impulse distribution for the 6 edge segments has to be carefully adjusted. We

have assumed that Ψ has a width of 20% of the pupil diameter and that it has a rectangular shape. Thus, we obtain the signal c_I at detector I in Fig. 3.7 by integrating the curvature for $\rho = 0.5$ to 1 and $\theta = 0$ to $\pi/3$ and by integrating $\frac{\partial \phi}{\partial \rho}$ for $\rho = 0.8$ to 1.2 and $\theta = 0$ to $\pi/3$. The result is

$$c_I \propto 0.4\sqrt{3}\ a_2 + 0.4\ a_3 - 2.5\ a_4 + 1.489\ a_5 + 0.8598\ a_6 - 5.736\ a_7 - 9.935\ a_8 + 2.353\ a_9 ... \ .$$

One obtains a set of seven equations relating the signals of the sensors to the Zernike coefficients. This set of equations can be written in matrix form similar to Eq.(3.17) as

$$\vec{c} = \Theta_c \vec{a}, \tag{3.22}$$

with $\vec{c}$ the vector containing the measured curvature and gradients for the edge segments, $\vec{a}$ the vector containing the coefficients of the Zernike polynomial and Θ_c the interaction matrix. A simple least-squares routine was used to solve this equation.

A comparative study between the 2×2 Shack-Hartmann sensor discussed in the previous section and the 7-element sensor discussed here has shown that the performance is very similar down to very low light levels [29, 80].

The measurement errors of the curvature sensor were investigated by Roddier [76]. He found that the error propagation coefficient $P(J)$ (Eq. 3.19) increases with J and not with $\ln(J)$. This is the reason why the curvature sensor is more suited for low order correction.

3.2.3 Shearing interferometer

Apart from the two wave-front sensing methods discussed so far, both of them measuring intensities in or close to the telescope focus, there is a third method, the shearing interferometer. Here, the wave-front interferes with itself in the telescope pupil. The interference pattern, the fringes, are then used to determine the local slope of the wave-front. Fig. 3.8 displays the principle.

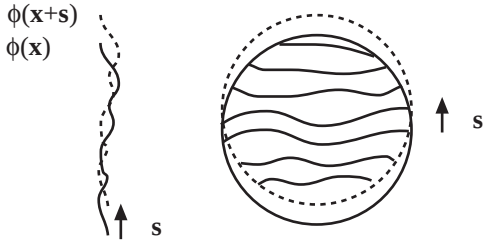

Figure 3.8: Principle of the shear interferometer. The form of the fringes in the interferogram are determined by the shape of the wave-front.

The signal that is measured in a shearing interferometer can be expressed quite simply as the sum of the complex amplitudes

$$\begin{aligned} I(\vec{x}) &= \frac{1}{2}\left|\exp(i\phi(\vec{x})) + \exp(i\phi(\vec{x}+\vec{s}))\right|^2 \\ &= 1 + \cos(\phi(\vec{x}) - \phi(\vec{x}+\vec{s}))\ . \end{aligned} \tag{3.23}$$

With ϕ the phase of the wave-front in rad, the signal is wavelength dependent. It becomes independent of the wavelength if the shift is proportional to the wavelength. Grating interferometers have been used to achieve achromatic properties (see [96] for details). For a small shift $|\vec{s}|$ the phase difference $\phi(\vec{x}) - \phi(\vec{x} + \vec{s})$ is approximately equal to the slope of the wave-front in the direction of the shear vector $\vec{s}$. With a Taylor approximation for small shear s_x along the x-axis one obtains

$$\phi(\vec{x}) - \phi(\vec{x} + (s_x, 0)) = s_x \frac{\partial \phi(\vec{x})}{\partial x} + \epsilon(s_x) \; . \tag{3.24}$$

In order to reconstruct the wave-front two interferograms with orthogonal shear are required. Extended sources reduce the fringe contrast since the quantity that is being measured is the coherence function at $|\vec{s}|$. Thus, similar to the curvature sensor the wave-front sensor geometry has to be adjusted according to the object size.

The subapertures that determine the spatial resolution of the slope measurements are represented by the size of the detector pixels. Since the shear interferometer belongs to the class of slope sensors the noise properties are very similar to the Shack-Hartmann sensor.

3.3 Wave-front reconstruction

In the last section, we have assumed that the modes of a polynomial, in our example the Zernike modes, are reconstructed from the information obtained by the wave-front sensor. Apart from this modal reconstruction of the wave-front there exists also the zonal approach where the error in *e.g.* each subimage of a Shack-Hartmann sensor is minimised by tilting the wave-front in the subaperture. In a curvature sensor system this approach is even more intuitive in combination with a bimorph mirror (see Sect. 3.5). Here, the curvature of the mirror surface is changed by applying a voltage to the mirror actuator and, in principle, the measured curvature signal from a single detector element can be hard-wired to the corresponding actuator of the bimorph mirror [76].

In both cases the local piston of the wave-front elements in each subaperture has to be treated separately in order to smoothly model the wave-front. This requires some very difficult reconstruction techniques [80]. Together with the high accuracy that is required in the opto-mechanical alignment to ensure a precise correspondence between the wave-front sensor elements and the deformable mirror actuators, the zonal approach becomes less attractive than the modal approach.

The matrix equation for the modal reconstruction $\vec{M} = \Theta_{\mathrm{sh}} \vec{a}$ (Eq. 3.17) connecting the coefficients of the Zernike modes $\vec{a}$ with the wave-front slopes $\vec{M}$ can be solved by a least-squares approach:

$$\vec{a} = (\Theta_{\mathrm{sh}}^T \Theta_{\mathrm{sh}})^{-1} \Theta_{\mathrm{sh}}^T \vec{M}. \tag{3.25}$$

The product of matrices $(\Theta_{\mathrm{sh}}^T \Theta_{\mathrm{sh}})^{-1} \Theta_{\mathrm{sh}}^T$ is called reconstructor matrix. This method can be extended to include the noise characteristics by adding a noise vector to the vector of slopes

$$\vec{M}_n = \vec{M} + \vec{N}. \tag{3.26}$$

To solve this equation the covariance matrix of the noise $< \vec{N} \vec{N}^T >$ has to be calculated. Since the two noise sources, the photon noise and the read noise, are statistically independent for each subaperture the covariance matrix is diagonal. If the noise variance of each subaperture is the

same and equal to $\sigma^2_{\rm noise}$ the result of the least-square minimisation can be written as (see *e.g.* [58])

$$\vec{a} = (\Theta^T_{\rm sh}\Theta_{\rm sh} + \sigma^2_{\rm noise} < \vec{a}\vec{a}^T >^{-1})^{-1}\Theta^T_{\rm sh}\vec{M}, \tag{3.27}$$

where $< \vec{a}\vec{a}^T >$ is the covariance matrix of the Zernike coefficients given in Table 2.3. This technique to reconstruct the wave-front is also called *maximum likelihood technique* as by determining $\vec{a}$ one maximimises the probability of producing the measurements $\vec{M}$. This method has recently been improved by implementing knowledge about the correlation of the slopes between the subapertures [82].

The coefficients $\vec{v}$ of the polynomials of the deformable mirror (the mirror modes) are related to the Zernike coefficients $\vec{a}$ through an additional interaction matrix so that a new interaction matrix can be calculated linking the slope measurements $\vec{M}$ directly with $\vec{v}$. The formalism is the same as above, with the exception that it might be extremely difficult to calculate the inverse of the covariance matrix $< \vec{v}\vec{v}^T >$ for a non-orthonormal set of mirror modes. If the mirror modes do not exactly match the surface of the mirror the maximum likelihood technique no longer represents the best estimate of the wave-front [79]. The minimum-variance method can be used to circumvent this problem [93]. Here, in order to maximise the image intensity the variance of the residual wave-front aberrations are minimised incorporating the mirror influence function. The practical drawback is that accurate knowledge of the wave-front and noise statistics, and of the mirror influence function are required.

3.4 Closed loop operation

So far, the properties of wave-front sensors have been discussed for the static case of a single measurement. In order to investigate the performance of adaptive optics systems the dynamic behaviour of turbulence has to be considered. In Sect. 2.5 and 2.6, the temporal characteristics of image motion and of the Zernike modes have been discussed. These properties are used in the following investigation of the dynamic requirements of adaptive optics systems.

3.4.1 Tip-tilt correction

First, we have to define a requirement for the image stabilisation that provides an acceptable image quality. The next step is then to determine the tracking frequency that stabilises the image sufficiently to achieve the image quality, using the temporal power spectra that were calculated in Sect. 2.5.

In Sect. 2.5 the two axis variance of the image centroid motion was given as

$$(\Delta\theta)^2 = 0.34(\lambda/r_0)^2(D/r_0)^{-1/3}[\mathrm{arcsec}^2], \tag{3.28}$$

with the seeing λ/r_0 in arcsec. The related variance $\sigma^2_{\rm tt}$ of the wave-front phase ϕ due to the two axis image centroid motion is the sum of the variance due to the wave-front slope alone and the contribution of the wave-front coma given in Table 2.2, yielding

$$\sigma^2_{\rm tt} = (0.896 + 0.025)(D/r_0)^{5/3} = 0.92(D/r_0)^{5/3}[\mathrm{rad}^2]. \tag{3.29}$$

The two axis variance of the image motion $(\Delta\theta)^2$ and the residual phase variance $\sigma^2_{\rm tt}$ are related linearly by

$$\sigma^2_{\rm tt} = 2.7\,\frac{(\Delta\theta)^2}{(\lambda/D)^2}[{\rm rad}^2], \tag{3.30}$$

with $\Delta\theta$ and λ/D both in $\rm arcsec$ or both in $\rm rad$.

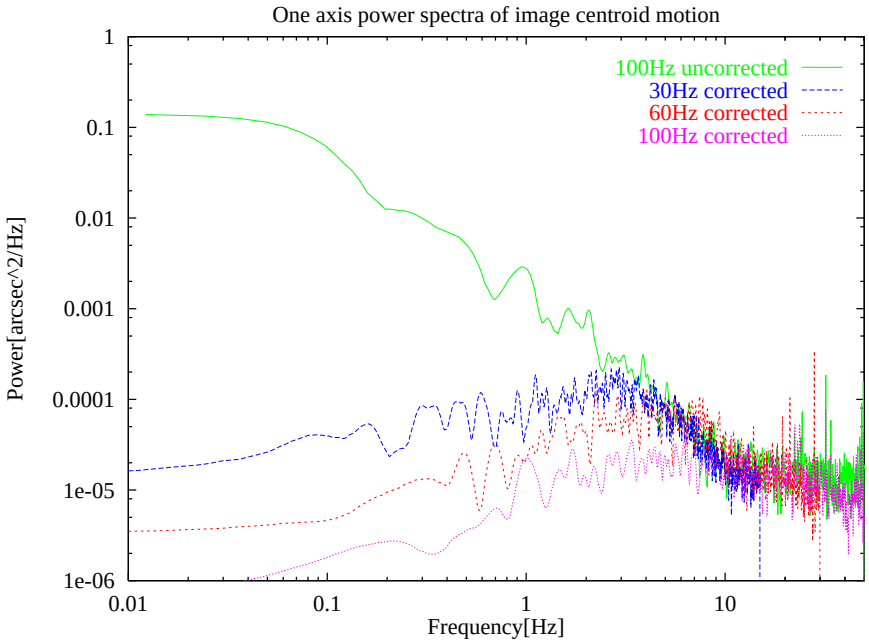

Figure 3.9: An uncorrected power spectrum sampled at 100 Hz, and power spectra sampled and corrected at 30, 60 and 100 Hz. At frequencies below 10 Hz, one can clearly see the influence of the different sampling frequencies. The level of the power spectrum is lower for higher sampling frequencies implying better correction. At higher frequencies there is no difference.

As a performance criterion for tip-tilt systems, one can use a measure that is related to the variance of the wave-front phase after perfect centroid tracking. If it is acceptable that the phase variance due to the residual image motion adds 10% to the phase variance due to higher order terms given in Eq.(3.4), the tip-tilt system has to reduce the variance of the image motion $(\Delta\theta)^2$ and the phase variance σ^2_{tt} by a factor of 64, yielding

$$\begin{aligned} \sigma^2_{\rm tt,res} &= 0.014(D/r_0)^{5/3}[{\rm rad}^2], \\ (\Delta\theta_{\rm res})^2 &= 0.0053(\lambda/D)^2\,(D/r_0)^{5/3}[{\rm arcsec}^2]. \end{aligned} \tag{3.31}$$

Then, the tolerable single axis rms image motion in terms of the seeing λ/r_0 in $\rm arcsec$ is given as

$$\Delta\theta_{\rm res,single} = 0.052(\lambda/r_0)(D/r_0)^{-1/6}[{\rm arcsec}]. \tag{3.32}$$

If the seeing is 0.76″ at 2.2 μm and r_0 is 60 cm on a 3.5-m telescope the single axis rms image motion has to be reduced from 0.23″ to 0.028″ in order to add less than10% to the residual variance of the wave-front phase.

The variance of the wave-front phase ϕ, due to the higher order Zernike terms plus the remaining coma (Eq. 3.4), and the residual image motion (Eq. 3.31), can be written as

$$\begin{aligned} \sigma^2 &= \sigma^2_{\text{centroid}} + \sigma^2_{\text{tt,res}} \\ &= (0.158 + 0.014)(D/r_0)^{5/3} \\ &= 0.172(D/r_0)^{5/3}[\text{rad}^2]. \end{aligned} \tag{3.33}$$

This expression was derived in [22] with a minor numerical inaccuracy.

How fast do we have to track the image in order to reduce the image motion by this amount? Control theory provides the tools to describe closed loop systems. Similar to the description of the imaging process with a transfer function for the spatial frequency spectrum of the image intensity, a tip-tilt system can be modelled with a temporal transfer function describing the effect of the tracking process on the temporal frequency spectrum of the image jitter.

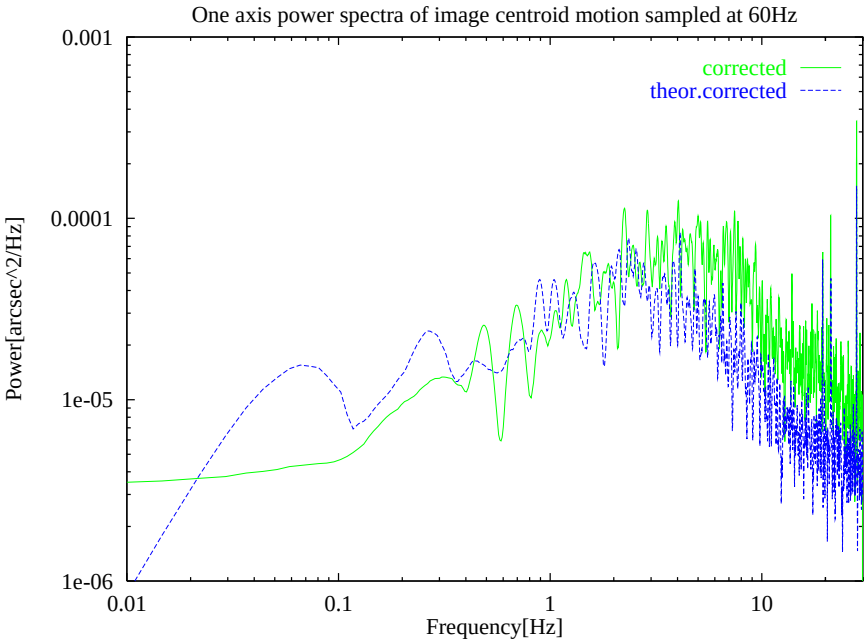

Figure 3.10: Comparison between the measured power spectrum of the image motion corrected at 60 Hz, and the theoretical power spectrum that is calculated by multiplying the spectrum of the uncorrected image motion with the closed loop transfer function. The latter can be regarded as the 'best case' power spectrum of corrected image motion. The spectra agree fairly well at low frequencies between 0.1 and 1 Hz. At higher frequencies, the corrected power spectrum is slightly amplified compared to the 'best case' spectrum.

The power spectra of tip-tilt corrected image motion can be modelled using the closed loop transfer function [31]

$$T(f) = \frac{(f/f_{3\text{dB}})^2}{1 + (f/f_{3\text{dB}})^2}\ , \tag{3.34}$$

with $f_{3\text{dB}}$ the *3dB servo bandwidth* which is about 10 times smaller than the loop frequency, depending on the parameters of the closed loop algorithm. Multiplying the temporal power spectrum $\Phi_{\theta,t}(f)$ (Eq. 2.37) of the image motion with the transfer function $T(f)$ gives the corrected

power spectrum. The properties of the corrected spectrum in the low and high frequency regime can be described using the approximation for $\Phi_{\theta,t}(f)$ given in Eq.(2.38). With $T(f) \approx (f/f_{3\mathrm{dB}})^2$ for $f \ll f_{3dB}$ and $T(f) \approx 1$ for $f \gg f_{3\mathrm{dB}}$ the corrected low frequency spectrum $P_{f_{low}}$ becomes proportional to $f^{4/3}$, and the corrected high frequency spectrum for $f \gg f_{3\mathrm{dB}}$ remains unaffected.

The integral over the product of the corrected power spectrum is the variance of the corrected image motion:

$$(\Delta\theta_{\mathrm{corr}})^2 = \int \Phi_{\theta,t}(f)T(f)df \ . \tag{3.35}$$

The bandwidth $f_{3\mathrm{dB}}$ of the servo system has to be chosen such that the corrected variance equals the value defined in Eq.(3.31). Using the approximation of a single dominant layer with a wind speed $\hat{v}$ (see Sect. 2.5) one finds that the required tracking bandwidth to reduce the rms image motion to 1/8 of the uncorrected value is

$$f_T = 1.62\ \hat{v}/D \ , \tag{3.36}$$

where D is the telescope diameter. If the effective wind speed is $15\,\mathrm{m/sec}$ ($54\,\mathrm{km/h}$) on a 3.5-m telescope the required tracking bandwidth is approximately $7\,\mathrm{Hz}$. As the bandwidth of a closed loop system is about 10 times smaller than the sampling frequency, the image motion has to be sampled at about $70\,\mathrm{Hz}$. The Strehl ratio that can be achieved at $2.2\,\mu\mathrm{m}$ in $0.76''$ seeing is then 5.3%, which is twice the uncorrected value of 2.6%.

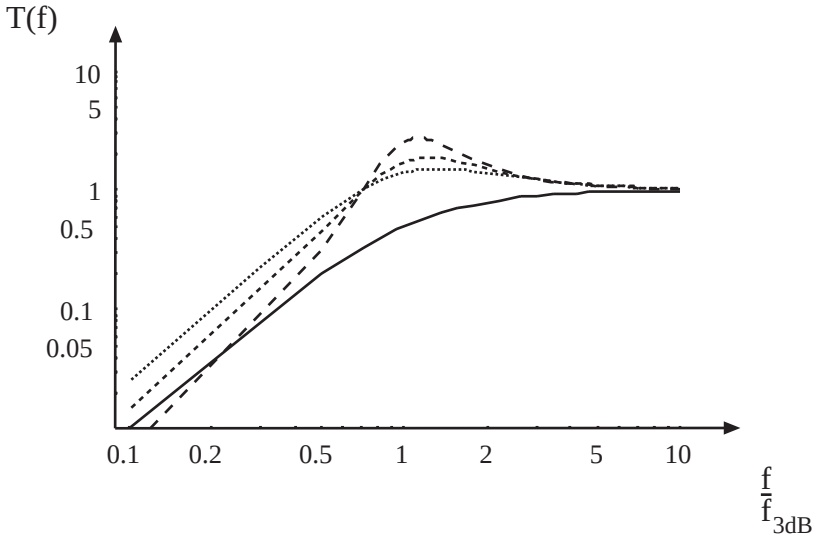

Figure 3.11: Closed loop transfer functions for different parameters. The solid line represents the transfer function given in Eq. (3.34). The dashed lines incorporate the effect of the finite bandwidth of the tip-tilt mirror, where the curve with the highest peak at $f/f_{3\mathrm{dB}}$ represents the system with the highest gain. Lower gain results in a lower peak, but the properties at low frequencies are deteriorated. (Compare to experimental results in Fig. 3.12.)

It is interesting to write the variance of the tip-tilt corrected wave-front as a function of the actual bandwidth $f_{3\mathrm{dB}}$ of the tip-tilt system. If $f_{3\mathrm{dB}}$ is much larger than the tracking bandwidth,

one finds that the residual variance is proportional to $f_{3\mathrm{dB}}^{-2}$ [88]. In the frequency region around the tracking bandwidth the variance is approximately proportional to $f_{3\mathrm{dB}}^{-5/3}$ [22] and one can write

$$\sigma^2_{\mathrm{tt,res}} = (f_T/f_{3\mathrm{dB}})^{5/3} 0.014 (D/r_0)^{5/3} [\mathrm{rad}^2]. \tag{3.37}$$

Power spectra of uncorrected image motion and of corrections at sampling frequencies of 30, 60 and 100 Hz are displayed in Fig. 3.9. This data was taken with CHARM, a tip-tilt correction system for the Calar Alto 3.5-m telescope that is described in Sect. 4.1 [26]. The cross over point between the uncorrected and the corrected spectrum is approximately the servo bandwidth of the closed loop system. Fig. 3.9 shows that the bandwidth is roughly 4, 6 and 10 Hz for 30, 60 and 100 Hz loop frequency respectively. It should be noted that the residual image motion calculated as the integral over the power spectrum is mainly caused by incomplete removal of image motion at frequencies below 5 Hz.

Fig. 3.10 displays a measured tip-tilt corrected power spectrum and a theoretical power spectrum that is obtained by multiplying an uncorrected power spectrum with the transfer function $T(f)$. The comparison shows that $T(f)$ models the system reasonably well except for the amplification that occurs at frequencies larger than the bandwidth. This behaviour is caused by the tip-tilt mirror that needs a finite amount of time to move to a new position. Taking this lag into account the transfer function takes on a more complex form that is displayed in Fig. 3.11 (see [89], Chapter 7). This is only one example for a closed loop transfer function. Depending on the

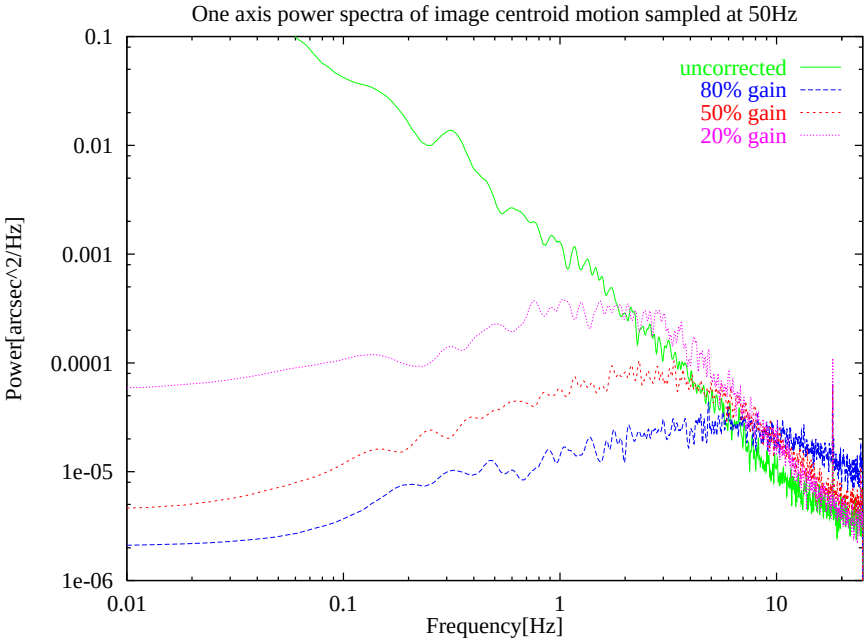

Figure 3.12: Comparison between an uncorrected power spectrum and power spectra corrected at 50Hz with different gains. The values of the corrected power spectrum at low frequencies increase as the gain is decreased, since lowering the gain has a similar effect to lowering the sampling frequency as shown in Fig. 3.9. However, low gain results in less amplification of high frequency jitter. Thus, lower gain can be an advantage if high frequency telescope resonances have a larger influence on the image quality than atmospheric turbulence.

parameters of the servo system one can create a large variety of transfer functions to optimise the behaviour at different frequencies [12].

The amplification at frequencies $f \geq f_{3\mathrm{dB}}$ is proportional to the applied gain that is defined as the percentage of the measured centroid offset that is applied to the piezos in order to move the centroid to the image center. However, reducing the gain in order to decrease this effect reduces the performance at lower frequencies. As the atmospheric tip-tilt power spectrum shows a steep decay at high frequencies one has to carefully adjust the gain factor in order to optimise the performance.

Usually, we run our tip-tilt system at a gain of 80%. In Fig. 3.12 the power spectra at a loop frequency of 50 Hz are compared for gains of 80, 50 and 20%, showing that the bandwidth drops with decreasing gain. The servo bandwidth is at about 5 Hz for 80% gain, at 3 Hz for 50% gain and at 2 Hz for 20% gain. The amplification of the power spectrum at high frequencies is lowest for the lowest gain. Thus, if the telescope mechanical resonance frequencies have a larger effect on the image quality than the atmospheric turbulences, then the gain can be reduced to dampen them. CHARM allows the adjustment of the gain in real time, and the changes can be controlled via the real time display of the image centroids.

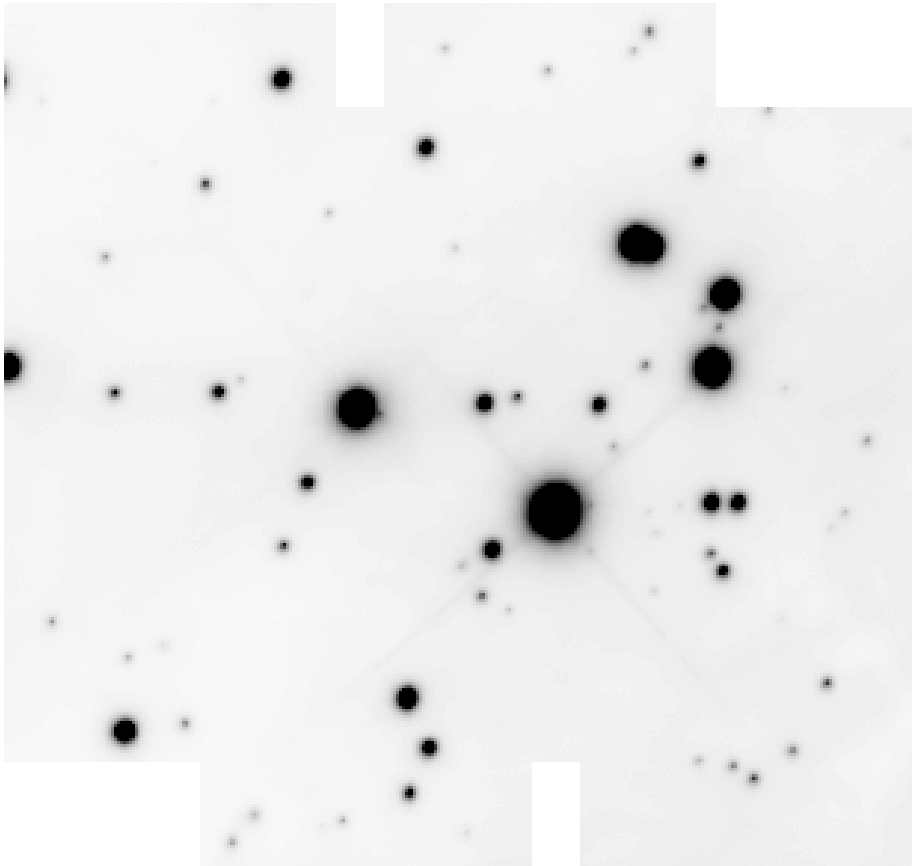

Figure 3.13: A mosaic of tip-tilt corrected images of the Trapezium Cluster at 2.1 $\mu\mathrm{m}$. The field of view is 54.5$\times$51.8 arcsec at 0.178″ per pixel, and the resolution is 0.35″ FWHM which is a factor of two improvement over the uncorrected images (see [56]). For comparison: the diffraction limit of the Hubble Space telescope at the same wavelength is 0.21″.

In order to give an idea of the image quality that can be achieved with a tip-tilt system a corrected image of the Trapezium is displayed in Fig. 3.13. The images were obtained in September 1993 on the Calar Alto 3.5-m telescope in the near infrared (2.1 $\mu\mathrm{m}$).

A mosaic of several corrected images is displayed in Fig. 3.13. Here, two different guide stars (θ^1Ori C and θ^1Ori D) were used for peak tracking in different series of images. Of the 40 tip-tilt corrected images, the best 24 were chosen to ensure the highest image quality. The mosaic covers an area of $54.5\times51.8\,\mathrm{arcsec}$, and the effective integration time per pixel is $72\,\mathrm{sec}$. The uncorrected seeing was typically 0.7″ FWHM. The peak intensity of the corrected images is doubled and the FWHM is 0.35″, which is only a factor of 2.7 above the diffraction limit of the 3.5-m telescope. In the corrected image, the stars are seen to have narrow cores superimposed on a broader halo. These features are more prominent in the image profiles. There is no evidence of degraded resolution towards the edges of the image indicating that the isoplanatic patch is larger than the field of view. The astronomical results from these data have been discussed in McCaughrean and Stauffer [56].

3.4.2 Higher order correction

Operating an adaptive optics system by correcting many modes of the Zernike polynomials can be regarded as an extension of the tip-tilt system described in the last section since all modes are controlled independently. Two parameters have to be adjusted according to the number of modes that are corrected: the gain and the bandwidth. The gain should be different for each mode depending on the accuracy of the measurement that can be determined experimentally.

The required bandwidth for full correction was given by Greenwood [31]. He assumed a system that in the static case corrects the wave-front perfectly, and that all aberrations are caused by the finite bandwidth of the control system. He then used the power spectrum $\Phi_t(f)$ of the phase fluctuations of the wave-front (Eq. 2.30) and applied the transfer function $T(f)$ (Eq. 3.34) to calculate what was subsequently called the Greenwood frequency that by using the single dominant layer approximation is simplified yielding

$$f_G = 0.43\frac{\hat{v}}{r_0}. \tag{3.38}$$

The residual variance of the wave-front can then be calculated as

$$\sigma_G^2 = (f_G/f_{3\mathrm{dB}})^{5/3}[\mathrm{rad}^2]\ . \tag{3.39}$$

If the servo bandwidth $f_{3\mathrm{dB}}$ of the closed loop system is chosen equal to f_G the variance is $1\,\mathrm{rad}^2$ which is equivalent to a Strehl ratio of about 35%.

This variance has to be compared to the residual variance after correcting *e.g.* 50 Zernike modes perfectly. Using Eq.(2.45), one finds that it is $\Delta_{50} = 0.25\,\mathrm{rad}^2$ in 0.9″ seeing, corresponding to a Strehl ratio of 77%. Although Greenwood's assumption of a perfect system cannot be compared easily to the case of removing only a limited number of Zernike modes – leaving a residual phase variance even for infinite bandwidth – it is clear that the Greenwood frequency with the residual variance of $1\,\mathrm{rad}^2$ is too small for a good correction.

Fig. 3.14 shows the result of a simulation using the method described in Sect. 2.7. Correcting for 50 Zernike modes with infinite bandwidth (for details see the figure caption) gives a Strehl

ratio of about 80% that agrees well with the theoretical result of 77%. However, applying Greenwood's criterion to estimate the additional residual phase variance for a finite bandwidth leads to a discrepancy between the simulated values and the theoretical values. For instance, for a loop frequency of100 Hz and for 50 corrected modes the Strehl ratio in the simulation is 56% (Fig. 3.14), and the Strehl ratio of the Greenwood model is 66%. The simulation gives an idea of how the image quality evolves with bandwidth and number of modes. But in order to come to a better analytic estimate one should apply the closed loop transfer function of the system in use to the temporal power spectrum of the Zernike modes and calculate the contributions of the single modes at a given bandwidth. This estimate would then be much more realistic.

In the case of a laser guide star adaptive optics system the image motion has to be measured with a natural guide star (see Sect. 3.6). Then our criterion to reduce the image motion to one 1/8 of the uncorrected value is no longer sufficient. One has to redefine the requirement in terms of the Airy disk with a diameter λ/D. If it is the goal to reduce the single axis rms image motion $\Delta\theta$ to $0.25\lambda/D$ the tracking bandwidth can be calculated in the same way as in the last section using Eqs. (3.30), (3.31) and (3.37) to obtain

$$f_{\mathrm{h.o.,T}} = 0.25\ \hat{v}/r_0. \tag{3.40}$$

Tyler investigated pure Zernike tilt and the centroid tilt separately, and he presented a similar result [88].

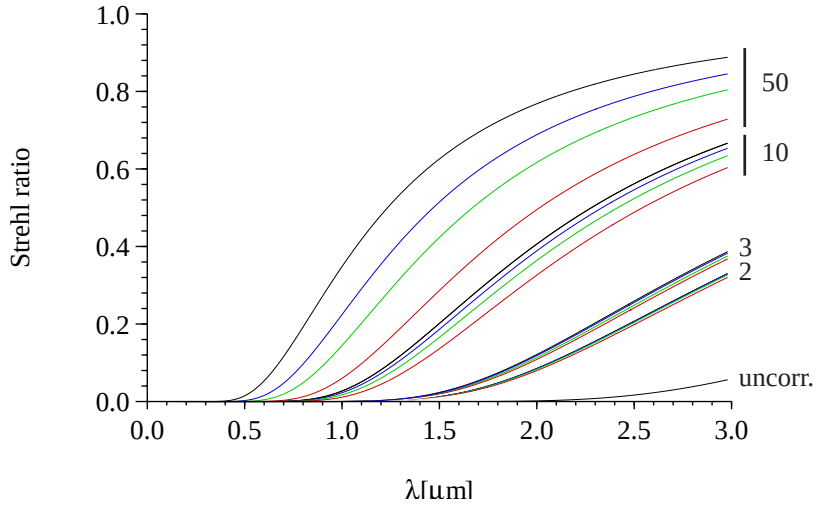

Figure 3.14: The Strehl ratio as a function of wavelength for different numbers of corrected modes and different bandwidths for an effective wind speed of 4 $\mathrm{m/sec}$ and 0.9″ seeing at 2.2 $\mu\mathrm{m}$. Four groups of curves (each group ranging from black to light grey) and the uncorrected seeing, reaching barely 0.06 at 3 $\mu\mathrm{m}$, are displayed for corrections of 2, 3, 10 and 50 Zernike modes each correction at four loop frequencies, ∞ Hz (black curves), 400, 200 and 100 Hz (light grey curves). The largest number of modes, 50, yields the highest Strehl ratios at all frequencies, with a wide spread for different frequencies. Correcting only two (tip and tilt) or three (tip, tilt and focus) modes shows approximately the same result for all frequencies as 100 Hz is well above the required tracking frequency of 20 Hzwhich is about 10 times the tracking bandwidth f_T. The curves are the result of a simulation using the method described in Sect. 2.7.

The subsequent variance of the wave-front phase due to the residual image jitter alone is

$$\sigma^2_{\mathrm{h.o.T}} = (f_{\mathrm{h.o.T}}/f_{\mathrm{3dB}})^{5/3} 0.33\,[\mathrm{rad}^2]. \tag{3.41}$$

The very simple assumptions that lead to these results make it impossible to draw far reaching conclusions. However, it is fair to say that the tip-tilt system has to be run at almost the same frequency as the higher order system in order to add an acceptable amount to the variance of the wave-front. Conan et al. came to a very similar conclusion discussing the temporal power spectra of the Zernike modes that are displayed in Fig. 2.6.

If for example the effective wind speed $\hat{v}$ is $15\,\mathrm{m/sec}$ and if r_0 is $60\,\mathrm{cm}$ which is equivalent to 0.76″ seeing at $2.2\,\mu\mathrm{m}$ the bandwidth for full correction according to the Greenwood criteria is $f_G = 11\,\mathrm{Hz}$, and the required tracking bandwidth is $f_{\mathrm{h.o.,T}} = 6\,\mathrm{Hz}$. The respective tracking frequencies are about $110\,\mathrm{Hz}$ and $60\,\mathrm{Hz}$. It should be emphasised that this can only give an idea about the order of magnitude since the adaptive optics system is not perfect as Greenwood assumed, and, as noted above, since a residual variance of $1\,\mathrm{rad}^2$ is too large. In practice one can start at about 2–4 times the Greenwood frequency and determine the optimum bandwidth by examining the image quality achieved.

3.4.3 Error budget – limiting magnitude

We can now write down the error budget of an adaptive optics system with a Shack-Hartmann sensor:

$$\sigma^2 = \sigma^2_{\mathrm{fit}} + \sigma^2_{\mathrm{noise}} + \sigma^2_{\mathrm{bw}}, \tag{3.42}$$

with σ_{fit} the fitting error that represents the wave-front variance due to the uncorrected Zernike modes, σ_{noise} the measurement noise that is due to photon and read-noise (see Sect. 3.1.3), and σ_{bw} the error due to finite bandwidth. The fitting error for correcting J Zernike modes is given by Noll [62] as

$$\sigma^2_{\mathrm{fit}} = \Delta_J \approx 0.2944 J^{-\sqrt{3}/2}\,(D/r_0)^{5/3}\,[\mathrm{rad}^2] \text{ for large } J\,, \tag{3.43}$$

and is listed in Table 2.2 for J<12. D is the diameter of the telescope aperture.

The noise error σ_{noise} is given in Eqs. 3.18 and 3.19 and, including the complete expressions for the photon noise and the read noise, reads as

$$\begin{aligned}
\sigma^2_{\mathrm{noise}} &= P(J)\frac{\lambda_{\mathrm{WFS}}}{\lambda_{\mathrm{IR}}}\left(\sigma^2_{\mathrm{ph}} + \sigma^2_r\right)\,[\mathrm{rad}^2]\,, \text{with} \\
P(J) &= 0.34\ln(J) + 0.10, \\
\sigma^2_{\mathrm{ph}} &= \frac{\pi^2}{2}\frac{1}{N_{\mathrm{ph}}}(d/r_0)^2, \text{and} \\
\sigma^2_r &= \frac{\pi^2}{3} f^2 N^2_{\alpha_0}\left(\frac{\sigma_d}{N_{ph}}\right)^2\left(\frac{d}{r_0}\right)^4\,,
\end{aligned} \tag{3.44}$$

with $P(J)$ the factor for the error propagation in a Shack-Hartmann sensor correcting for J Zernike modes [72]. d is the diameter of the subaperture, $N^2_{\alpha_0}$ is the total number of pixels per

Airy disk, and f is the quotient between the area on the detector used for the centroid calculation and the area of the seeing disk. (As long as the subaperture diameter is larger than r_0. This is always the case as the wave-front sensor operates in the visible with r_0 typically $10\,\mathrm{cm}$.) As noted in Sect. 3.1.3, the case of background photon noise is treated very similarly by replacing the detector read noise σ_d by the background noise σ_b [80].

The error due to the finite bandwidth was discussed in the last section and given to be

$$\sigma^2_{\mathrm{bw}} = \sigma^2_G = (f_G/f_{3\mathrm{dB}})^{5/3}\mathrm{rad}^2, \tag{3.45}$$

where the Greenwood frequency is $f_G = 0.43\ \hat{v}/r_0$. A numerical example will illuminate the situation.

We assume a situation where the seeing is 0.76″ in the near infrared at $2.2\,\mu\mathrm{m}$ on a 3.5-m telescope. The Fried parameter is then $r_0 = 0.6\ \mathrm{m}$. A Shack-Hartmann sensor, operating in the visible with $\lambda_{\mathrm{WFS}} = 0.5\,\mu\mathrm{m}$ and 5×5 subapertures ($d = 0.7\ \mathrm{m}$) is used to correct for 15 Zernike modes. In the table the seeing parameters are summarised:

Wavelength	$0.5\,\mu\mathrm{m}$	$2.2\,\mu\mathrm{m}$
Seeing	1″	0.76″
d/r_0	7	1.1

The discussion starts with the fitting error, *i.e.* the best variance that we can theoretically achieve if for correcting 15 Zernike modes. It is $\Delta_J = 0.028(D/r_0)^{5/3} = 0.56\,\mathrm{rad}^2$ corresponding to a Strehl ratio of 57%. If we want to add less than $0.2\,\mathrm{rad}^2$ to the variance, *i.e.* if the Strehl is to stay above 45%, one can for a first iteration allow $0.1\,\mathrm{rad}^2$ for the noise error and equally $0.1\,\mathrm{rad}^2$ for the bandwidth error. The Greenwood formula can be used to estimate the required bandwidth and then the star magnitude can be determined that provides enough photons to have less than $0.1\,\mathrm{rad}^2$ for the noise error.

With $\hat{v} = 15\ \mathrm{m/sec}$ and $r_0 = 0.6\,\mathrm{m}$ the Greenwood frequency is $11\,\mathrm{Hz}$. Since we want to add less than $0.1\,\mathrm{rad}^2$ to the variance our bandwidth has to be $44\,\mathrm{Hz}$, and, thus, the frame rate of the Shack-Hartmann sensor has to be 10 times the bandwidth, *i.e.* about $450\,\mathrm{Hz}$. The exposure time is then about $2\,\mathrm{msec}$.

The read noise for a pure tip-tilt system was investigated in Sect. 3.1.3. To discuss the read noise for centroid measurements in a Shack-Hartmann sensor with subaperture diameter d and with $P(J) = 1$ for correcting $J = 15$ Zernike modes we obtain

$$\sigma^2_{\mathrm{noise}} = \left(40\frac{\sigma_d}{N_{\mathrm{ph}}}\right)^2 + \frac{12}{N_{\mathrm{ph}}}\,[\mathrm{rad}^2]\ . \tag{3.46}$$

If the read-noise is $\sigma_d = 5$ electrons, which is typical for CCD cameras we need about 600 photons per subaperture in $2\,\mathrm{msec}$ to reduce the additional variance to $0.1\,\mathrm{rad}^2$. This corresponds to a star with $m_V = 10$, which is a realistic number for the set of parameters used here. If the requirements for the bandwidth are relaxed the variance σ^2_{bw} increases with $f^{-5/3}_{3\mathrm{dB}}$ and $\sigma^2_{\mathrm{noise}}$ decreases with N^2_{ph} as long as the second term, the photon noise remains small. Thus, reducing the bandwidth by a factor of two increases the noise by a factor of 3 but it reduces the read noise by a factor of 4 resulting in a net gain in performance. However, as the concept of the Greenwood

frequency is fairly crude one should not overestimate the significance of the calculated values for small changes.

One parameter that has not been treated so far is the isoplanatic angle that determines the maximum distance between the object and the guide star. This depends heavily on the degree of correction and the layer structure of the atmosphere. Rigaut has investigated this quantity [70] and found that, depending on the tolerated additional variance values between 10″ and 30″ can be expected in the near infrared. If a guide star of 10th magnitude has to be no more than 30″ from the astronomical object the number of objects that fulfill this requirement is very small.

However, if an artificial guide star can be placed anywhere in the sky the situation changes dramatically. Only the tip-tilt correction relies on a natural guide star, and here the requirements are much relaxed compared to the full correction. A formula for the static error was given in Eq. 3.15, and the noise error is

$$\sigma_{\mathrm{noise}} = \left(210\frac{\sigma_d}{N_{\mathrm{ph}}}\right)^2 + \frac{312}{N_{\mathrm{ph}}}. \tag{3.47}$$

If the tolerated additional variance is 0.1 rad^2 and the read noise $\sigma_d = 5$ electrons, 3000 photons per exposure are required.

The bandwidth for tip-tilt correction can be calculated using Eq.(3.41), yielding $f_{\mathrm{h.o.,T}} = 0.5\ \hat{v}/r_0 = 12.5\,\mathrm{Hz}$, resulting in a tracking frequency of 125 Hz and an exposure time of 8 msec. Here, the tip-tilt system has to run faster than for pure tip-tilt tracking ($f_T = 1.62\ \hat{v}/D \approx 7\,\mathrm{Hz}$ see Sect. 3.4.1) because the error has to be reduced to the absolute value of 0.1 rad^2 independent of seeing conditions. 3000 photons per 8 msec exposure time correspond to a magnitude of about $m_V = 13$. This limiting magnitude and the larger isoplanatic angle increase the sky coverage drastically.

3.5 Deformable mirrors

The earliest developments of deformable mirrors aimed at TV projection systems in the early 1950's. In the so-called Eidophor system, a mirror in a vacuum chamber is covered with a thin layer of oil upon which a modulated beam from an electron gun is deposited in a rastered pattern. Local forces of surface repulsion are induced forming transient changes in the slope of the oil film. The wave-front is then locally tilted by refraction in traversing the film. The optical system of the TV projector blocks the tilted beam, and the point on the mirror remains dark in projection. Bright spots appear in the projected image of the mirror where the oil film is flat. The TV image is modulated onto the mirror by modulating the beam from the electron gun similar to the process of forming an image with a cathode ray tube.

For the application in adaptive optics systems the ability of the Eidophor mirror to shape the wave-front with local tilts was used. H. W. Babcock suggested to use this mirror in his proposal for an adaptive optics system in 1953 [3]. However, the technological problems at that time were too large to actually build the system.

Today, there are mainly three classes of deformable mirrors displayed in Fig. 3.15: The *segmented mirror* with single tip-tilt elements and two mirror types with a continous surface, the

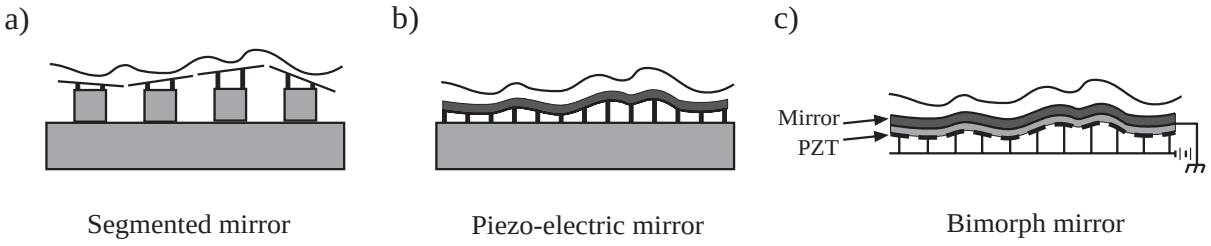

Figure 3.15: Three classes of deformable mirrors. (a), a segmented mirror with tip-tilt actuators behind each segment, (b) and (c) two types of continous mirrors with piston actuation in the piezo-electric mirror(b), and bending actuation in the bimorph mirror (c).

bimorph mirror where the curvature of the mirror surface is affected by applying a force parallel to the surface, and the *piezo-electric mirror*[4] where a stack of actuators behind the mirror surface pushes and pulls the mirror by applying a force perpendicular to the surface (see E. N. Ribak for a review [68]).

Segmented mirrors have a number of advantages over continous mirrors: the segments can be moved independent of each other, they can be replaced easily, and the single segments can be combined to form rather large mirrors. In the section on wave-front sensors (Sect. 3.2) it was discussed that by associating each sub-aperture of a Shack-Hartmann sensor to a segment of the mirror the high order adaptive optics systems consist basically of tip-tilt systems that are run in parallel. Although this is appealing because of its conceptual simplicity, in addition to the single segment tip-tilt correction, one has to process the data to obtain the piston signals that are necessary to reconstruct a continous wave-front. Also the alignment between the subapertures of the Shack-Hartmann sensor and the single segments has to be very precise. The disadvantages of segmented mirrors include problems with diffraction effects from the individual segments and the intersegment alignment. In infrared applications the gaps between the segments can be the source of infrared radiation that deteriorates the image. Only few adaptive optics systems with segmented mirrors have been built for solar [1] and stellar [13] astronomy.

Bimorph mirrors are constructed of a thin piezoelectric material bonded to a thin mirror membrane (see Fig. 3.15c). When a voltage is applied to the PZT material it expands in area similar to a bimetallic strip. The curvature of the surface is proportional to the applied voltage. The application of a curvature to the wave-front make the bimorph mirrors the natural counterparts of the curvature sensor. As noted in Sect. 3.2, it was discussed to feed the signal from the curvature sensor directly to the bimorph mirror [76]. This design is similar in its conceptual simplicity to the idea of using a mirror segment for each subaperture of a Shack-Hartmann sensor. However, the requirements for the optical alignment are similar. The bimorph mirrors that are commercially available have only a low number of actuators, *e.g.* the bimorph mirror in the CFHT adaptive optics system has 19 actuators (see Sect. 3.2). The excellent seeing conditions on Mauna Kea make the 19 actuator mirror a good choice. The seeing at most other observing sites is worse so that a higher number of actuators is required to achieve a good performance.

[4]Since the bimorph mirror also works with piezo-electric material, it is not completely straightforward to use this name for only one class of mirrors. However, most people call it by this short name since this type of mirror is most commonly used, and since the other type is always referred to as bimorph mirror.

Piezo-electric mirrors, *i.e.* continuous mirrors with an array of piezo-electric actuators expanding perpendicular to the mirror surface (Fig. 3.15b) are in widespread use now. They are available with up to 350 actuators, and the technology is well tested and very reliable. They were developed originally to project high power laser beams on military targets when segmented mirrors produce too much scattered light [89]. The typical voltage that is required to move the actuators is below 100 V, the bandwidth is in the kHz range, and the typical stroke is in the 5 $\mu\mathrm{m}$ range. Whilst this is sufficient for high order correction the tip and tilt induced by the turbulence requires a larger tilting angle so that an extra tip-tilt mirror is needed. Some manufacturers are now using electrostrictive material like a lead-magnesium-niobate (PMN) crystal that is similar to the piezo-electric lead-zirconate-titanate (PZT) ceramics, but that displays a smaller hysteresis and a better motion control.

Both types of continous surface mirrors avoid the diffraction effects associated with the single segments and the intersegment alignment problem. Here, the problems arise from the complexity of the algorithm to control the mirror surface as the actuators are not allowed to move independent of each other. If one actuator is set to the maximum voltage its next neighbour must not be set to the minimum voltage. Otherwise the mirror surface would be damaged. Also, changing the voltage of a particular actuator usually affects the shape of the mirror surface at the location of its neighbours.

There are several new developments ranging from very large deformable mirrors that can replace the telescope secondary [81], to extremely small units that are based on microelectronical manufacturing methods [91]. A completely different class of wave-front actuation is represented by the liquid crystal half-wave phase shifter especially suitable for narrow band applications [52]. The LBT[5] will be equipped with an adaptive secondary with 1000 actuators that has a diameter of 870 mm and a thickness of 2 mm. Using actuators with a larger stroke this design allows the correction of all aberrations, including tip-tilt. It is discussed to use an actuator design based on loudspeaker technology where the actuator motion is provided by voice coils. The advantage of the design with an adaptive secondary is the conceptual elegance and the low number of reflections that are an advantage both for the optical throughput and the infrared background [40].

3.6 Laser guide stars

An artificial guide star that can be placed anywhere in the sky to a large extent solves the very restrictive limiting magnitude problem. The sky coverage can then be increased to nearly 100% depending on seeing conditions. This technique was first discussed by the US Air Force in 1982 in connection with propagating laser beams to satellites. For this application, natural background stars are not suitable as guide stars since satellites are moving too fast. However, all the related research was classified until 1991 [34]. Independent of the military research, R. Foy and A. Labeyrie published the concept to create a laser guide star in the upper atmosphere in 1985 [14]. Since then, a number of tests have been carried out [87, 42, 51, 18, 55, 84].

[5]The **L**arge **B**inocular **T**elescope consists of two 8.4-m telescopes separated by 14.4 m (center to center). The Telescope is currently under construction on Mount Graham in Arizona, USA

The basic concept of creating an artificial guide star is rather simple: A laser beam is projected into the sky, into the center of the field of view of the observing telescope. Then, using either the light that is reflected in the stratosphere by Rayleigh scattering, or the resonance fluorescence in the D_2 line of sodium (Na) atoms in the mesosphere at an altitude of about 100 km, one can determine the atmospheric turbulence. However, although the Rayleigh scattering is rather strong - indicated by the fact that it is visible with the naked eye - there are some technical difficulties and some principle shortcomings. The technical problem is that the scattered light from the highest layers in the stratosphere should be used, and, thus, the Rayleigh scattering from the lower layers has to be filtered out either by temporal gating or by spatial discrimination. Usually, a fast shutter is used that opens after the light has propagated from the laser launching telescope to a layer at 10-20 km and back [19].

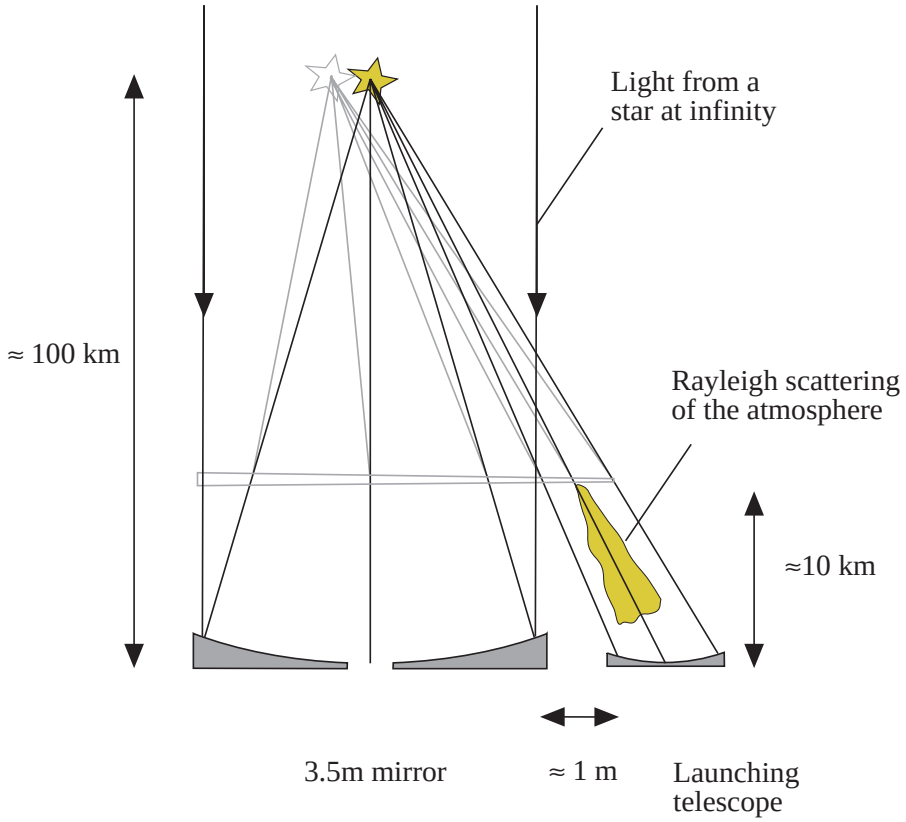

Figure 3.16: Elements of a laser guide star system. The launching telescope projects the beam into the mesosphere at 100 km where the artificial star is observed with the main telescopes. The wedge illustrates the effect of a constant tilt over both apertures: from the main telescope the laser guide star seems to be in the same position as before since the two tilts cancel. One can also estimate the effect of the cone effect by comparing the diameter of the cone at an altitude of 10 km with that of the beams from infinity.

The difficulty is then to relate the wave-front from the artificial star at 10-20 km to the wave-front that comes from the astronomical object at infinity. The problem is that the light from the laser guide star is not affected at all by the highest layer of turbulence as this is where the artificial star is created, and that the lower layers of turbulence are illuminated by a cone with the

laser guide star at the top of the cone. The light from the artificial star always travels through substantially narrower portions of the turbulent layers than the natural star light. Also, the turbulence "seen" by the spherical wave from the laser star is slightly different from the turbulence that affects a plane wave from an object at infinity. This is why this effect is also called focal anisoplanatism or cone effect. The turbulence profile in Fig. 2.2 shows that the contribution from turbulence at high layers is not to be neglected. There have been suggestions to deal with the cone effect by creating multiple guide stars in order to properly scan at least the lower layers [61].

Creating an artificial star in the mesosphere at an altitude of about 100 km reduces the focal anisoplanatism as the cone in the highest turbulent layers at an altitude of 20 km has already 80% of the diameter of the parallel beams from the star at infinity propagating into the telescope aperture. Fig. 3.16 describes the situation, and illustrates too why the image motion cannot be measured with a laser guide star. The laser light projected through a launching telescope into the mesosphere is affected by the atmospheric turbulence. It suffers from the wave-front slope that makes the artificial star move randomly in the mesosphere. Observing the laser star from the ground adds another random slope to the wave-front travelling downwards. If the two slope terms are identical, like in Fig. 3.16 where the slope is represented by a wedge, the artificial star as seen from the ground remains in the same position. In practice, the image of the artificial star in the wave-front sensor camera moves randomly.

The higher orders of the phase distortion on the way up are responsible for the blurring of the intensity distribution. Therefore, the artificial star as a slighly extended object can be used to measure the higher order terms of the turbulence in the downward propagation unaffected by the wave-front distortion on the way up.

Recently, there have been suggestions to measure the tip-tilt term with the laser guide star. R. Foy suggested to achieve this by creating a polychromatic artificial star exciting different lines of the sodium and deriving the slope information using differential effects [15]. Other authors propose to observe the laser from a telescope quite a distance away from the main telescope. The tip-tilt information is obtained by monitoring the movement of the now elongated laser guide star and compare it to a natural star close to the elongated intensity distribution [66]. If it were possible to measure the wave-front slope with the laser guide star one could achieve 100% sky coverage under all circumstances. However, neither technique has been verified experimentally.

The diameter of the spot in the mesosphere is approximately equal to the seeing in rad times the altitude, *i.e.* 0.5 m in $1''$ seeing. An object of this lateral size has an angular diameter of $1''$ from the ground. The image of the laser guide star is degraded due to seeing, and the image shape is the convolution of the seeing disk with the object in the mesosphere that itself has approximately the shape of the seeing disk. The result of the convolution is that the angular size of the laser guide star is $\sqrt{2}$ times larger than the seeing.

The drawback of a laser guide star in the sodium layer is the power requirement. The sodium atoms are in a layer of about 10 km thickness in the mesosphere originating from meteorite ablation. The brightness of the resonance fluorescence is proportional to the column density of sodium atoms and the laser power, as long as the laser power is below the saturation limit. The column density varies with season, with a maximum in winter and a minimum in summer, and with geographical latitude. It can vary by a factor of two or more within a few days. There is not yet a sufficient number of measurements to give more specific numbers. In experiments with a

1 W continous wave dye laser a $m_V = 12$ magnitude sodium star was created [7]. With ALFA, using a 3W laser of the same type, the magnitude of the created laser guide star was $m_V = 10$ [65].

3.7 Outlook – Multi-layer adaptive optics

In the following, we discuss a new method for measuring separately the turbulence in multiple atmospheric layers by combining intensity measurements like in a curvature sensor with wave-front gradient measurements in a Shack-Hartmann sensor [23]. The isoplanatic angle can then be increased by doing this measurement for several stars simultaneously and applying the information on the wave-fronts to deformable mirrors in the image planes of the turbulent layers [44]. Then, a much larger field of view can be corrected. The optical design of a system with deformable mirrors in the proper positions is rather simple. The difficulty lies in the separation of the aberrations of different layers.

The problem of measuring the atmospheric turbulence can be reduced to imaging a phase object, *i.e.* an object affecting only the phase of the wave-front. This is a common problem in microscopy, and defocusing is an old cure. Then, the phase object that is invisible in the focused image shows up in the intensity distribution. If the phase varies only slightly, ($\phi(x) \ll 1$) the image intensity is proportional to the curvature of the phase distribution. Thus, the scintillation on the ground could be used for an estimate of the high altitude layers [69]. In order to reconstruct the phase distribution completely, the intensity distribution has to be measured in two planes positioned symmetrically to the image plane of the phase object. The curvature sensor is based on this idea.

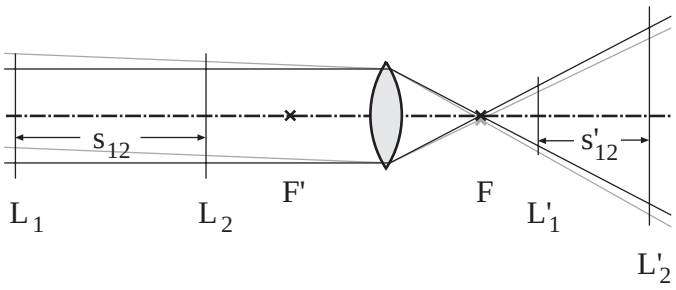

Figure 3.17: Illustration for the optical paths of two different stars.

To simplify the explanation, we start with two dominant layers that carry the bulk of the turbulence. Then, the intensity distribution $I_1(x_1)$ in the conjugate plane L_1' of layer L_1 in Fig. 3.17 would be determined solely by the turbulence in layer L_2. The turbulence in layer L_1 has no effect on the intensity distribution in its image plane, L_1'. Vice versa, the intensity distribution in L_2' is caused only by the turbulent layer in L_1.

Assuming that the phase variation is weak, with $\phi(x) \ll 1$, the complex amplitude immediately behind layer L_1 can then be written as

$$u_1(x_1) = 1 + i\phi_1(x_1).$$

The wave-front amplitude $u_2^-(x_2)$ immediately before L_2 is the Fresnel diffraction pattern of the turbulence in L_1. Using an approximation for Fresnel diffraction for small angles [59], it is

$$\begin{aligned} u_2^-(x_2) &= u_1(x_2) - i\frac{s_{12}}{2k}\frac{\partial^2 u_1(x_2)}{\partial x_2^2} \\ &= 1 + i\phi_1(x_2) + \frac{s_{12}}{2k}\frac{\partial^2 \phi_1(x_2)}{\partial x_2^2}, \end{aligned}$$

with $k = 2\pi/\lambda$. The turbulence in layer L_2 adds to the imaginary part of $u_2^-(x_2)$ yielding

$$u_2(x_2) = 1 + i\left(\phi_1(x_2) + \phi_2(x_2)\right) + \frac{s_{12}}{2k}\frac{\partial^2 \phi_1(x_2)}{\partial x_2^2}. \tag{3.48}$$

Calculating the wave-front in image space, one has to be careful to include the phase disturbances of both layers. Thus, the complex amplitude $u_2'(x_2')$ in L_2' is, neglecting imperfections of the imaging optics, identical to $u_2(x_2)$ in L_2. However, to calculate the wave-front in L_1' the turbulence in L_2 has to be considered. This can be done by first calculating the complex amplitude in L_1' as the defocused image of layer L_2, and then calculating the distribution in L_2' as the defocused image of L_1'.
With $u_2'(x_2') = u_2(x_2')$ (disregarding magnifying factors) the complex amplitude in plane L_1' is

$$\begin{aligned} u_1'(x_1') &= u_2(x_1') + i\frac{s_{12}'}{2k}\frac{\partial^2 u_2(x_1')}{\partial x_1'^2} \\ &= 1 + i\left(\phi_1(x_1') + \phi_2(x_1')\right) - \frac{s_{12}'}{2k}\frac{\partial^2 \phi_2(x_1')}{\partial x_1'^2}. \end{aligned} \tag{3.49}$$

The phase parts of both u_1' (Eq. 3.49) and u_2' (Eq. 3.48 with $u_2'(x_2') = u_2(x_2)$) are given by $\phi_1 + \phi_2$. Thus, the exact position of a Shack-Hartmann sensor measuring the wave-front tilts is not very critical.

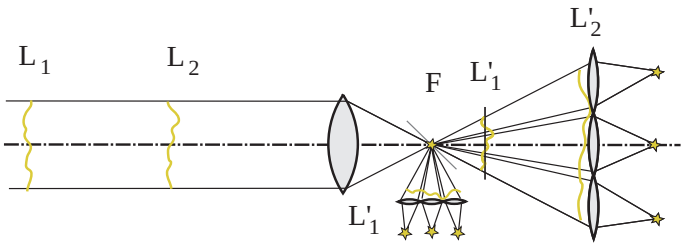

Figure 3.18: Design for a Shack-Hartmann curvature sensor. A beam splitter is used to send the light to the lenslet array in the image plane of L_1. Measuring the total intensity in each sub-image of each lenslet array provides the information on the wave-front curvature, and the measurement of the image centroid positions allows the reconstruction of the sum of the turbulences like in a Shack-Hartmann sensor.

The intensity distributions in L_1' and L_2' can be calculated as

$$\begin{aligned} I_1'(x_1') &= 1 - \frac{s_{12}'}{2k}\frac{\partial^2 \phi_2(x_1')}{\partial x_1'^2} \quad \text{and} \\ I_2'(x_2') &= 1 + \frac{s_{12}'}{2k}\frac{\partial^2 \phi_1(x_2')}{\partial x_2'^2} \end{aligned}$$

The intensity distribution in L_1' is unaffected by ϕ_1 and the intensity distribution in L_2' is unaffected by ϕ_2. Using the difference of the intensity distributions like a curvature sensor yields the second derivative of the sum of the phases. This is the result of a measurement with a curvature sensor neglecting the wave-front radial tilt.

Using Shack-Hartmann sensors in both planes L_1' and L_2', the resulting phase $\phi_1 + \phi_2$ of the wave-front is measured in each plane by determining the wave-front tilt in each subaperture (see Fig. 3.18). Additionally, the intensity distribution can be measured in both planes by integrating over each subaperture of the lenslet array. The normalised signal $I_1' - I_2'/I_1' + I_2'$ is the quotient of the second derivative of the sum and of the difference of the phases. As the sum of the phases is measured directly, the difference of the second derivatives can be determined and, thus, the phase curvature in both layers.

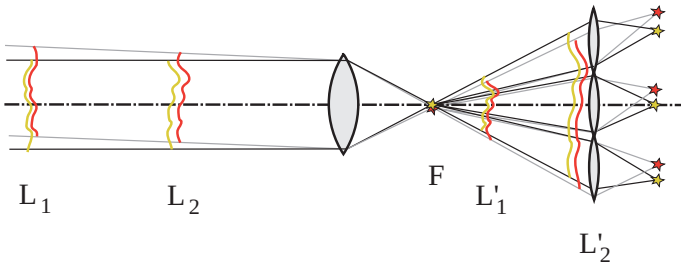

Figure 3.19: Illustration of the multiplexer mode of the Shack-Hartmann curvature sensor. For the sake of clarity only one lenslet array is displayed. In each subimage the total intensity and the centroid position can be measured separately and, thus, different patches of the wave-front can be reconstructed.

The isoplanatic angle can now be enlarged by observing multiple stars with the Shack-Hartmann sensor as displayed in Fig. 3.19. The phase as well as the intensity distribution can be measured for each star individually. Then, the information about the different layers can be stitched together to steer the deformable mirrors in the conjugate planes of L_1 and L_2.

Practical considerations

Before placing the Shack-Hartmann curvature sensors in the conjugate planes of the turbulent layers their altitude has to be determined by *e.g.* using a method suggested by Vernin [92].

So far, the discussion has been restricted to two layers. If the turbulence profile indicates multiple strong layers there has to be a Shack-Hartmann curvature sensor in each conjugate plane of those layers. The position of the deformable mirrors can be adjusted to correspond to the conjugate planes of the layers. The number of deformable mirrors in a real system is obviously fixed. However, the system could be designed with several deformable mirrors using only the required number.

The isoplanatic angle is limited by the separation of the stars used for the measurement of the turbulence. The practical limitation is given by the field of view of each subimage of the Shack-Hartmann sensor. To correct 50 Zernike modes one needs about 8×8 subapertures each of which with a field of view of $30\times30''$. Then, with a pixel scale of roughly $0.5''$ every subimage has a size of 60×60 pixels, and the total size of the CCD is 500×500 pixels.

Chapter 4

Examples of Adaptive Optics Systems

The consequence of the previous discussions is that a high order adaptive optics system needs a laser guide star to provide good sky coverage. There is a number of laser guide star systems for test or military purposes: The US Air Force 1.5-m telescope at the Starfire Optical Range, New Mexico, is equipped with a laser guide star system using Rayleigh scattering with the main task to observe satellites [18]. The Multi-Mirror Telescope, Arizona, also has a laser guide star system to create a Sodium guide star [51] that serves mainly as a testbed for the planned upgrade

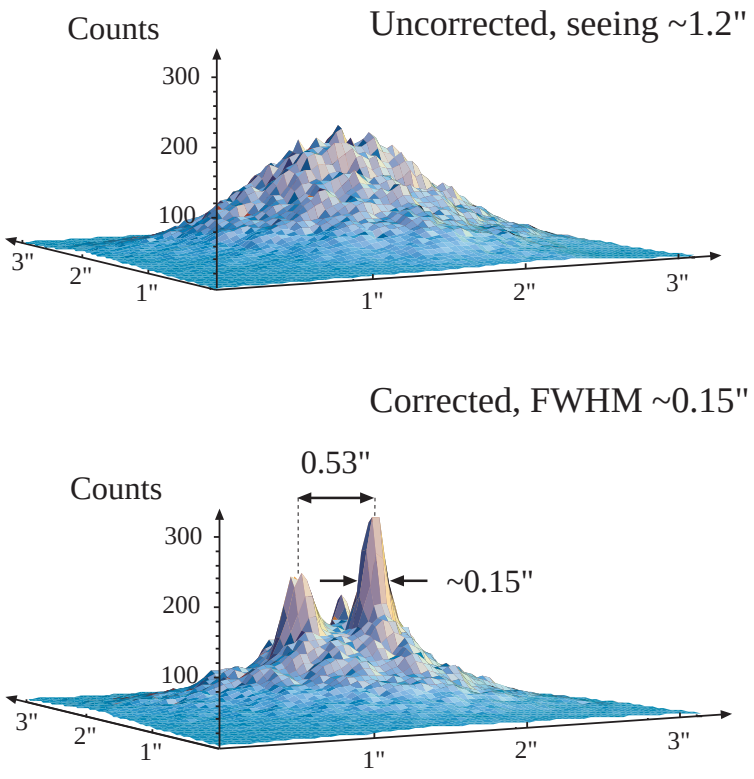

Figure 4.1: The first result with ALFA. This near infrared image ($\lambda = 2.2\,\mu\mathrm{m}$) of 72 Peg, with a magnitude $m_V = 5.75$, was taken on October 7, 1996 at 10pm. The 0.53″ binary is clearly resolved. This is a raw image without any image processing.

of the telescope to a single 6.5-m mirror [83]. Tests for the Keck Telescopes in Hawaii were performed at the 3-m Shane Telescope of the Lick Observatory, California, closing the loop on a Sodium laser guide star for the first time [55]. A group at the University of Chicago, lead by Edward Kibblewhite, designed a laser guide star system, ChAOS, that was tested recently at the Apache Point 3.5-m telescope, New Mexico [84].

In 1994, we decided to build ALFA[1], an adaptive optics system with a 97 actuator deformable mirror and with a laser guide star, as a common user instrument for the Calar Alto 3.5-m telescope. The project is a collaboration between the Max-Planck-Institute for Astronomy, responsible for the adaptive optics system, and the Max-Planck-Institute for extraterrestrial Physics, providing the laser guide star system [24]. We saw first light in September 1996.

As a preparation for the high order adaptive optics system we built a tip-tilt system for the 3.5-m telescope, CHARM, that eventually became the prototype for the ALFA tracking system and for our contribution to the UKIRT Upgrades Programme. For this programme we provided a new telescope front ring with a tip-tilt secondary mirror and the required wave-front sensor. The two tip-tilt systems will be described briefly before ALFA will be discussed.

4.1 Tip-tilt systems: CHARM and UKIRT

CHARM[2] was designed as a simple tip-tilt correcting module to the near-infrared camera MAGIC [38] for the 3.5-m telescope on Calar Alto. For tip-tilt sensing in the visible the system is equipped with a CCD camera. In regions where no bright enough optical stars are available (*e.g.* star forming regions, molecular clouds and the Galactic Center), we have also implemented for the first time a mode in which MAGIC can be used both as a tip-tilt sensor for infrared sources, and simultaneously as the science camera [26].

CHARM was built between March and September 1993. It fits into MAGIC's mounting flange and leaves the telescope focus in the same position with or without the CHARM reimaging optics in the beam. These optics can be moved remotely in and out of the telescope beam. Fig. 4.2 displays the instrument. The relay optics of ALFA are based on this design.

The optical design is similar to the MMT tip-tilt system [95]. A single parabola is used to image the telescope pupil on the tip-tilt mirror - which is in the focal plane of the parabolic mirror - and to reimage the telescope focus into MAGIC's focal plane (see Fig. 4.2). In order to keep the telescope focus in the same position with and without CHARM, we have changed the MMT design in positioning the telescope Cassegrain focus closer to the parabola. Consequently, the reimaged focus moves further away from the parabola. The two folding mirrors and the tip-tilt mirror are mounted on a motorised stage and can be moved remotely in and out of the telescope beam. The folding mirror just before the infrared camera has a dichroic coating that reflects the infrared and transmits the visible to the CCD camera.

The instrument has two image motion sensors: MAGIC in subarray mode in the infrared and a CCD camera in the visible. The tip-tilt mirror is mounted on a piezo unit (PI-S330, manufactured by Physik-Instrumente, Waldbronn) with a maximum throw of $3.2''$ in the image plane. A VME bus system under VxWorks is used to run the instrument, *i.e.* to do the image centroid

[1] ALFA stands for Adaptive optics with Laser For Astronomy

[2] CHARM is an acronym for Camera High Angular Resolution Module

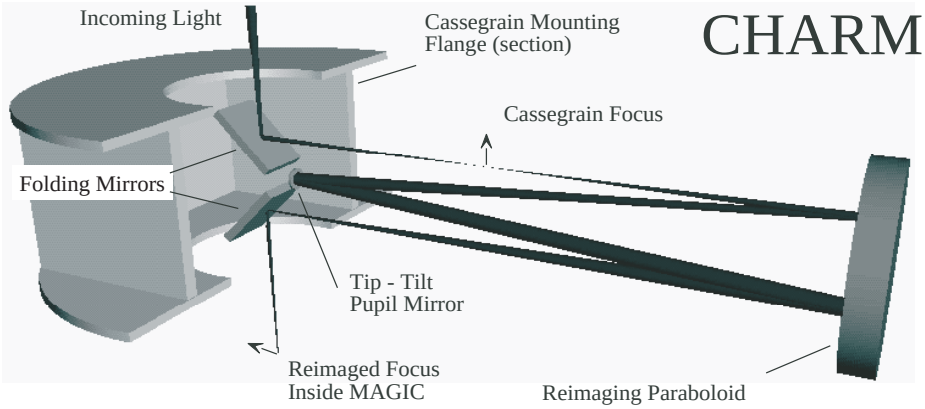

Figure 4.2: A sketch of the opto-mechanical setup of CHARM. The mounting flange is cut open to show the details. The two folding mirrors and the tip-tilt mirror are mounted on a motorised stage to move them in and out of the beam. The telescope focus without CHARM is in the same position as the reimaged focus. The lower folding mirror has a dichroic coating to reflect infrared wavelengths ($> 1\,\mu\mathrm{m}$) into MAGIC and to transmit visible wavelengths into the CCD camera (not shown here). The focal length of the parabola is $600\,\mathrm{mm}$ and the diameter is $200\,\mathrm{mm}$. The tip-tilt pupil mirror is in the focal plane of the parabola.

calculations and to provide the remote control of the movable mirrors. With a graphical user interface CHARM can be controlled from any computer on the network. The computer soft- and hardware is identical to the tip-tilt system of the UKIRT Upgrades programme [67] and very similar to ALFA.

An AstroCam 4201 controller with a Peltier cooled EEV CCD02 chip with 6 e^- read noise is used in the tip-tilt sensor in the visible (AstroCam, Cambridge, UK). With a pixel rate of 40 kHz, the chip has to be read out in subarray mode to produce a suitable frame rate. Reading out a 32 by 32 pixel subarray (*i.e.* 3.5″ by 3.5″ at a pixel scale of 0.11″) takes about $5\,\mathrm{msec}$ when 8 by 8 pixels are binned. As the binning is done before the analog-digital conversion, it does not add to the read noise of the chip. Exposure times of 5-20 msec and a read out time of $5\,\mathrm{msec}$ result in loop frequencies between 30 and $100\,\mathrm{Hz}$.

In Sect. 3.4.1, the measured power spectra of the image motion were discussed, and an example for the image quality of a tip-tilt corrected image was given. Here, a corrected and an uncorrected image of a single star (Fig. 4.3) are compared in order to evaluate the image quality of the tip-tilt correction using the formulas given in Sect. 3.1.1 and 3.4.1.

The data were taken in July 1995 on the Calar Alto 3.5-m telescope. A 9th magnitude star (SAO71942) was used both as a tip-tilt guide star for centroid tracking in the visible and as a 'science' object in the infrared. The seeing was 0.76″ at $2.2\,\mu\mathrm{m}$, corresponding to a Fried parameter of $r_0 = 0.6\ \mathrm{m}$, and the Strehl ratio of the uncorrected image was 2.7%. Running CHARM at $50\,\mathrm{Hz}$, the single axis rms image motion was reduced to 0.026″ which is equivalent to reducing the phase variance due to tip-tilt alone to $\sigma_{\mathrm{tt}} = 0.21\,\mathrm{rad}^2$ (Eq. 3.30). This variance and the contribution from the uncorrected high order modes (Eq. 3.4) predict a Strehl ratio of 6.8%.

However, the theoretical value cannot be achieved since the measured peak of the intensity distribution is reduced to about 85% of the maximum by integrating over one pixel although this pixel has a size of half the diffraction limit [22]. Thus, one cannot achieve more than 5.7%

Strehl ratio. The difference between this value and the measured value of 4.6% is acceptable as one also has to consider that the noise in the measurement forms a non zero background and the measured position of the image centroid and, thus, the residual image motion appear smaller than they actually are.

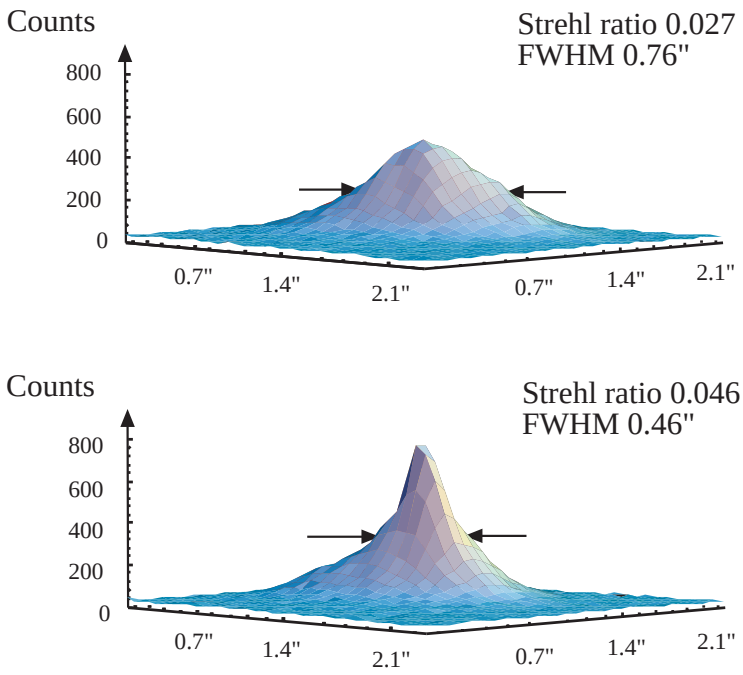

Figure 4.3: Tip-tilt correction with CHARM: Uncorrected (top) and corrected (bottom) images observed using MAGIC at 2.2 μm, and corrected at 50 Hz with the CCD camera as tip-tilt sensor. The star has a magnitude of $m_V = 9$. The measured Strehl ratio of 0.046 is 80% of the theoretical value for a tip-tilt corrected image under these seeing conditions at 2.2 μm on a 3.5-m telescope.

One can also make a careful estimate about the effective wind speed: With a closed loop bandwidth of about 1/10 of the tracking frequency of 50 Hz, *i.e.* $f_{3\mathrm{db}} = 5\,\mathrm{Hz}$, the residual phase variance of $\sigma_{\mathrm{tt}} = 0.21\,\mathrm{rad}^2$ and the tracking bandwidth $f_T = 1.62\hat{v}/D$, one can use Eq.(3.37) to estimate the wind speed to be about $9\,\mathrm{m/sec}$.

The second tip-tilt system was designed as part of the Upgrades Programme for the 3.8-m UK Infrared Telescope (UKIRT) on Mauna Kea, Hawaii. This programme was started in 1991 by the UK Science and Engineering Research Council through the Royal Observatory Edinburgh (ROE). The goal was to routinely provide near-diffraction limited images at 2.2 μm [37]. The main elements of the system are an adaptive tip-tilt secondary mirror system mounted on a hexapod structure for active collimation, an upgraded primary mirror support system and modifications to the telescope and dome to reduce dome seeing, so as to take advantage of the excellent natural seeing on Mauna Kea.

The contribution of the MPIA to this programme is a new telescope front ring with the tip-tilt secondary and the hexapod mount, and a small Shack-Hartmann wave-front sensor to measure tip-tilt and focus [27]. The primary mirror support system and the telescope modifications were provided by the Joint Astronomy Center in Hawaii in collaboration with the ROE.

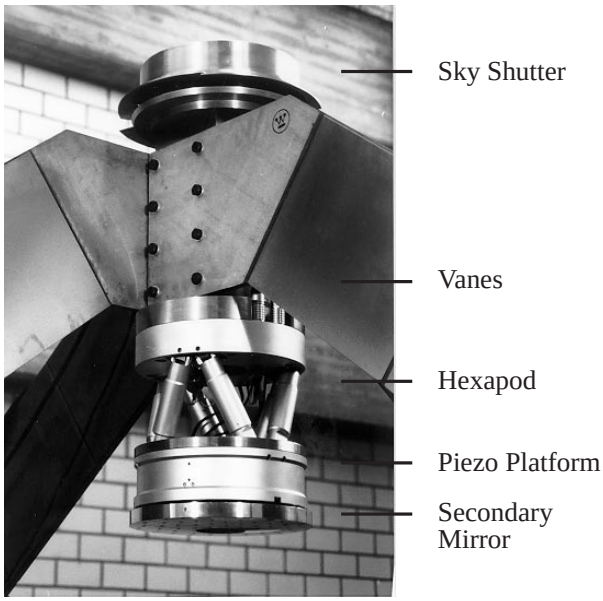

Figure 4.4: UKIRT: The new tip-tilt secondary mirror (diameter 313 mm) mounted on a hexapod structure. The telescope vanes covered with a thin sandwich structure to dampen mechanical oscillations. The sky shutter allows to optimise the telescope aperture for observations in the mid-infrared.

The Hexapod unit with the piezo platform was manufactured by Physik-Instrumente, and it is shown in Fig. 4.4. The secondary mirror with a diameter of 313 mm was fabricated by Horst Kaufmann, Crailsheim. With an ultra-sound light-weighting technique the weight of the secondary was reduced from 5.7 to 2 kg allowing for a maximum tip-tilt frequency of 225 Hz. The maximum tip-tilt angle is 5″ and the maximum chop[3] angle is 30″ up to a frequency of 10 Hz. Problems with high winds at Mauna Kea required extra measures to increase the mechanical stability of the top end. Therefore, the vanes are covered with a thin sandwich structure (manufactured by Westinghouse Electric Corporation, Sunnyvale, USA) increasing the modal damping coefficient by a factor of 60 over blank steel.

The hexapod provides six degrees of freedom for the secondary mirror for slow corrections of telescope aberrations due to mechanical flexure of the support structure, the so-called *active optics*. The throw of the hexapod legs is sufficiently large to use them to focus the telescope. The three piezo-electric actuators for the adaptive mode correct the image motion and the defocus due to atmospheric turbulence. The latter is possible since there is a large leverage between moving the secondary and the resulting focus shift: moving the secondary mirror 1 $\mu\mathrm{m}$ along the optical axis shifts the telescope focus by 200 $\mu\mathrm{m}$. The maximum motion of the piezos of 30 $\mu\mathrm{m}$ shifts the telescope focus by 6 mm which is the range of motion of the telescope focus due to turbulence under typical seeing conditions.

[3] *Chopping* is an imaging technique for mid-infrared observations (in the wavelength range $\geq 5\ \mu\mathrm{m}$) to reduce the slowly fluctuating thermal background. Here, the image position is moved at a frequency of about 1 Hz with a chopping mirror. With an exposure time of about 10 msec one obtains several images with the object and then several image with blank sky in the same area of the detector. The image intensity is obtained by calculating the difference

Therefore, the wave-front sensor of the UKIRT system was designed as a small Shack-Hartmann sensor with 2×2 subapertures. The same CCD camera and electronics is used as for CHARM. The software had to be extended to handle the four subimages and to reconstruct the first eight Zernike modes as described in Sect. 3.2.1. The requirement to enable tip-tilt correction on both ends of the chop throw made it necessary to have the camera rotatable so that the images of the guide star on both ends of the chop can be placed in an optimal position for fast read out of the subimages, that is as close as possible to the horizontal register of the CCD chip.

The tip-tilt system was inaugurated in August 1996 and immediately functioned without problems. The initial worry about the telescope oscillations disappeared after the first images were taken. The mechanical disturbances proved too small to measurably deteriorate the image quality. Fig. 4.5 displays power spectra of corrected and of uncorrected image motion with a tracking frequency of 100 Hz. The closed loop bandwidth is then approximately 10 Hz. The slight amplification around 20 Hz is caused by the closed loop transfer function (see Sect. 3.4). This increases the contributions of the oscillations around 20 Hz. Therefore, the rms image motion is reduced from typically 0.23″ to only 0.035″. This has to be compared to an rms image motion of 0.025″ that was achieved with CHARM on the more stable 3.5-m telescope at Calar Alto.

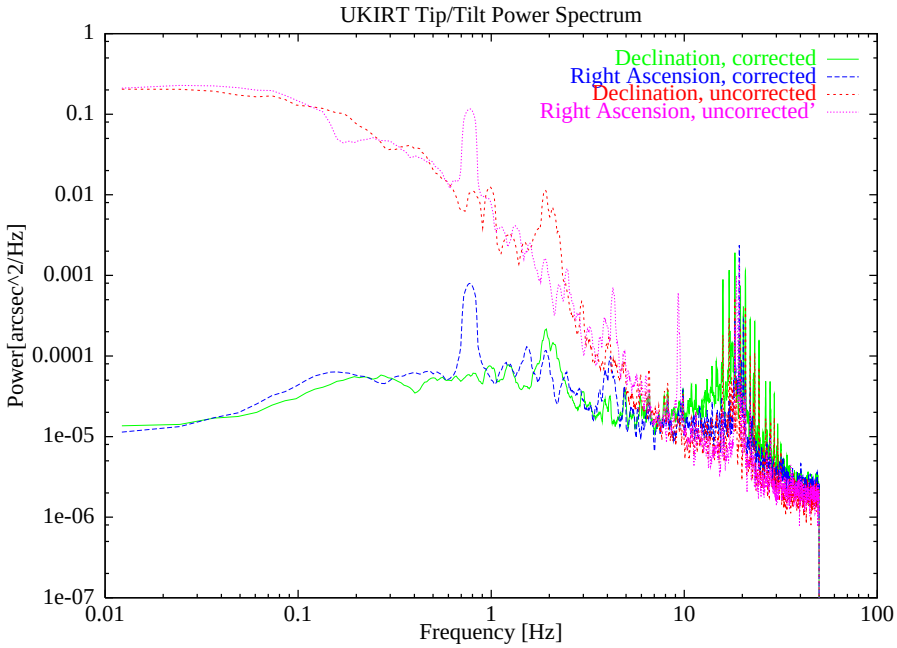

Figure 4.5: Power spectra of the corrected and uncorrected image motion at UKIRT with a tracking frequency of 100 Hz. The mechanical oscillations around 20 Hz are readily apparent.

An example of the improved image quality is shown in Fig. 4.6: The peak intensity tripled to 12% Strehl ratio and the FWHM at 0.25″ is only a factor of two larger than the diffraction limit. Although only tip and tilt are corrected the image shows the seeing limited halo around the almost diffraction limited spike as discussed in Sect. 2.6.

The formulas developped in Sect. 3.1.1 and 3.4.1 predict this Strehl ratio very nicely. In 0.5″ seeing at 2.2 μm the Fried parameter is $r_0 = 0.9$ m. The residual single axis rms image motion of 0.035″ corresponds to a residual phase variance due to tip-tilt alone of $\sigma_{\mathrm{tt}} = 0.46\,\mathrm{rad}^2$ (Eq. 3.30).

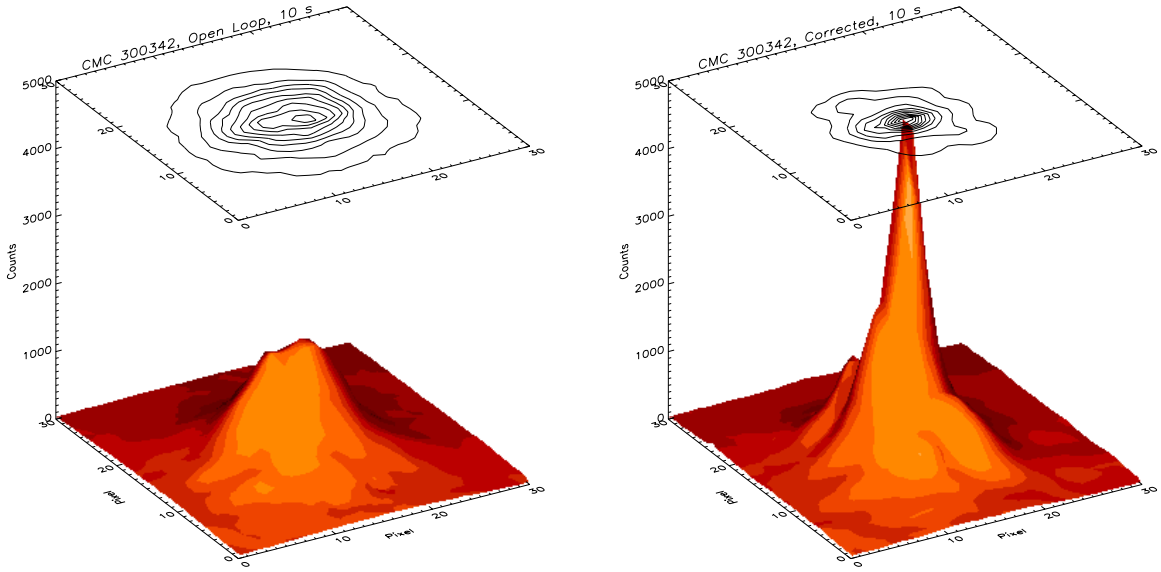

Figure 4.6: Uncorrected (left) and tip-tilt corrected (right) image of a single star at UKIRT. The FWHM is improved from 0.5″ to 0.25″ (the diffraction limit at the observing wavelength of $\lambda = 2.2\,\mu\mathrm{m}$ is 0.12″). The Strehl ratio increased from 4% to 12%.

The phase variance due to the uncorrected high order terms and the over-compensated coma is $\sigma_{\mathrm{centroid}} = 1.74\,\mathrm{rad}^2$ for $D/r_0 = 3.8/0.9 = 4.2$ (Eq. 3.4). Thus, the Strehl ratio is 15% which is reduced to 12.5% due to the finite pixel size of the infrared camera, which agrees very well with the measured value of 12%. However, due to the peculiar form of the power spectrum the Kolmogorov theory should be applied with care.

The example for the determination of the limiting magnitude in Sect. 3.1.3 gave a value of about $m_V = 15$ in 0.76″ seeing at $2.2\,\mu\mathrm{m}$ with 5 electrons read noise. Similar instrumental parameters in better seeing at UKIRT predict a value of about $m_V = 16$. In the meantime, a value of $m_V = 16.5$ has been confirmed experimentally [36].

More measurements when chopping was switched on and in 40 mph wind further underlined the excellent performance of the system. The FWHM was improved from 0.59″ to 0.28″ in high wind, and from 0.69″ to 0.30″ when tip-tilt correction was done together with chopping.

However, the adaptive focus correction suffers from insufficient stroke of the piezos. Although the motion range is of the same order of magnitude as the rms image motion, it is insufficient to cover the range of peak-to-valley values that are about 6 times larger. One could combine the rather slow motion of the hexapods to correct for the slow moving large values of turbulence induced focus, and let the piezos do the adaptive correction at the same time. This mode has yet to be implemented. Simulations have shown that the Strehl ratio could be improved from 12% to about 14% when the focus is corrected adaptively.

The UKIRT tip-tilt system is now part of the telescope, and it is used every night. Although the performance of tip-tilt systems depends heavily on the seeing conditions and do not allow to go to the diffraction limit they provide a steady improvement of the image quality increasing the scientific output of a telescope at virtually no penalty.

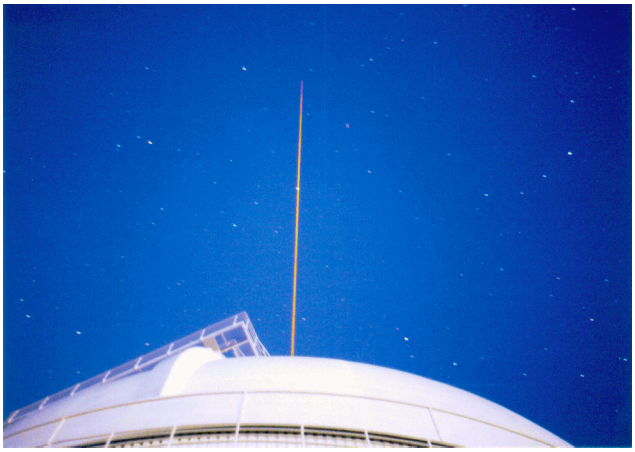

4.2 ALFA, an adaptive optics system with a laser guide star

The performance goal for ALFA was to achieve above 50% Strehl ratio in the near infrared at 2.2 μm under average seeing conditions, and to have a good sky coverage. Thus, a laser guide star is mandatory, and, given the weather conditions at Calar Alto with a median seeing of 0.9″at 2.2 μm, the number of corrected modes on the 3.5-m telescope has to be larger than 50. Under these seeing conditions, the perfect correction of 50 modes gives a Strehl ratio of 78% (Eq. 2.45). Taking the finite bandwidth (see Fig. 3.14), the detector noise and other error sources into account 50 modes were considered to be sufficient to achieve 50% Strehl ratio.

Since the project was planned on a time scale of two years between starting the design in 1994 and first light in 1996 we decided to purchase the main parts of the system. The 97-actuator deformable mirror with PMN (lead-magnesium-niobate) actuators was purchased from Xinetics, Littleton, USA[4], the high order wave-front sensor with a maximum of 100 subapertures and the soft- and hardware to do the wave-front reconstruction and to control the deformable mirror was provided by Adaptive Optics Associates (AOA), Cambridge, USA, the fast CCD camera for the Shack-Hartmann sensor is a product from Lincoln Laboratories, MIT, Lexington, USA, and the laser system with a 3-W dye laser was bought from Coherent, Santa Clara, USA. The camera and the software of the tip-tilt system are the same as in CHARM. The opto-mechanical design was done in house as well as the electronics for the optical elements that can be controlled remotely.

4.2.1 Optics

Two paraboloids are the main imaging elements of the optical system. The first paraboloid images the telescope pupil onto the deformable mirror and, after the reflection at the deformable mirror, the second paraboloid reimages the telescope focus into the infrared camera. Similar to CHARM, it was the design goal to have the reimaged telescope focus in the same position as the telescope focus without any optical elements from ALFA. Thus, in case of very bad seeing or mal functioning of the adaptive optics system the telescope can be used without ALFA by sliding

[4]The reason for buying a 97-actuator mirror instead of a 50-actuator mirror was simply that it was an off-the-shelf product of Xinetics. The next smallest mirror has 36 actuators which seemed too small for ALFA.

two mirrors out of the beam. Since the image quality of a high order adaptive optics system is always close to the diffraction limit the pixel scale of the infrared camera should be chosen accordingly. Without ALFA, large pixels are more convenient. Therefore the f/10 telescope focus is converted to an f/25 focus by the relay optics.

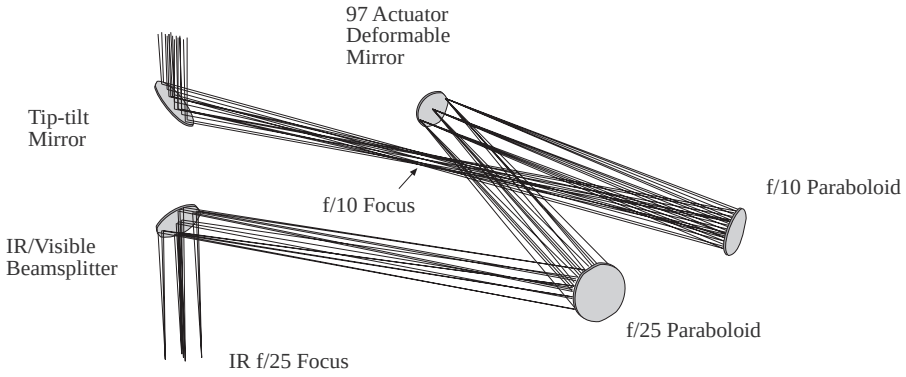

Figure 4.7: The main optical elements of the optical system of ALFA: The first folding mirror is the tip-tilt mirror since the deformable mirror does not provide sufficient stroke to correct for the image motion. The f/10 telescope focus is in the front focal plane of the f/10 paraboloid (focal length 662 mm) that images the telescope pupil onto the deformable mirror. After reflection at the deformable mirror the telescope focus is reimaged by the f/25 paraboloid (focal length 1594 mm), enlarged by a factor of 2.5. The IR/Visible Beamsplitter reflects the infrared band into the science camera and transmits the visible band into the wave-front sensor arm (see Fig. 4.8).

The diameter of the deformable mirror determines the basic parameters of the optical system displayed in Fig. 4.7. With the f/10 telescope focus in the front focal plane of the f/10 paraboloid its focal length has to be 662 mm in order to image the telescope pupil onto the (tilted) deformable mirror with an effective diameter of 66 mm. After reflection at the deformable mirror, the parallel beam is intercepted by the f/25 paraboloid with a focal length of 1594 mm to reimage the telescope focus into the infrared camera[5]. The first folding mirror is used as a tip-tilt mirror, and the last folding mirror acts as a beam splitter reflecting the infrared downwards into the infrared camera and transmitting the visible into the wave-front sensor arm. The field of view has a diameter of 3 arcmin. The optical design was provided by E. Harvey Richardson from the University of Victoria, Canada, who also designed the CFHT adaptive optics system which is very similar to ALFA. However, due to the smaller diameter of the bimorph mirror (42 mm) employed at the CFHT the focal lengths of the paraboloids can be shorter and the total dimensions of that system are about 1 m $\times$ 1.2 m.

The complete ALFA system mounted on a breadboard is presented in Fig. 4.8. One can recognise the five optical components described above: the tip-tilt mirror mounted on a linear motorised stage, the f/10 paraboloid, the deformable mirror and the f/25 paraboloid, and the partially hidden IR/Vis beamsplitter that reflects the infrared focus downwards. The additional components form five groups: the *FISBA interferometer* (FISBA Optik, St. Gallen, Switzerland), the

[5] As a result of the optical design the f-ratio of the reimaged focus was changed to f/24 instead of f/25. Out of habit, we keep calling it f/25.

f/10 reference fiber, to provide a perfect point source in the telescope focus, the *TV guider*, the *Shack-Hartmann sensor* and the *tip-tilt sensor* with the Na/Optical beamsplitter to separate the light from the sodium guide star from the natural tip-tilt guide star.

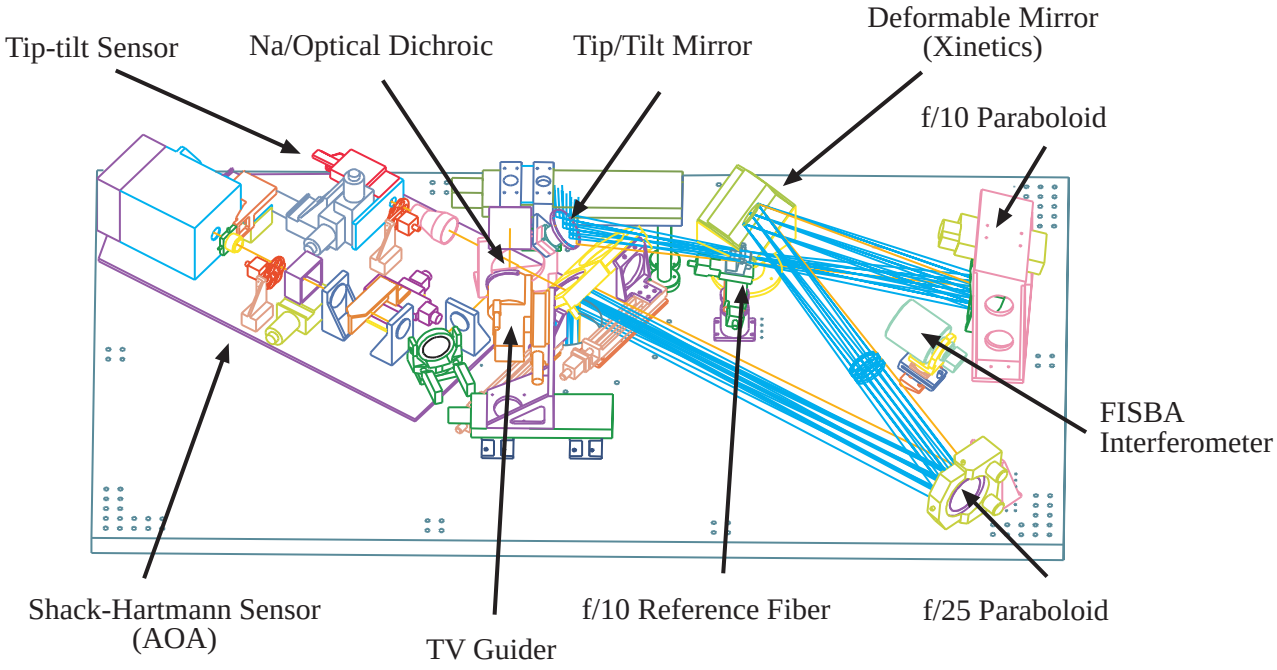

Figure 4.8: A CAD drawing of the ALFA breadboard with all opto-mechanical elements. The optical path in Fig. 4.7 is extracted from this drawing. Thus, the tip-tilt mirror, the f/10 paraboloid, the deformable mirror, the f/25 paraboloid and the (partially hidden) IR/Visible beamsplitter can easily be identified. Additionally, there is an artificial light source for adjustment and calibration purposes, the FISBA interferometer to control the mirror surface, the TV guider for acquisition, and the wave-front sensor arm with the Shack-Hartmann sensor and the tip-tilt sensor. Between the two the light is split by the Na/Optical beamsplitter.

The FISBA interferometer, a Twyman-Green interferometer, is a commercial product, to control the surface of the deformable mirror. This interferometer does not obstruct the telescope beam as it "looks" perpendicular at the mirror. After applying a voltage to the deformable mirror the actuators assume slightly different lengths that have to be equalised by adjusting the voltage carefully. The interferometer is used to control this process. The rms aberration of the reflected wave is about 600 nm when the same voltage is applied to all actuators and about 100 nm after adjusting the voltages. In the infrared this is equivalent to a phase variance of about 0.1 rad^2.

The f/10 reference fiber is a monomode fiber with a core diameter of 3.6 $\mu\mathrm{m}$ that serves as a perfect point source for alignment and calibration. It can be moved remotely in and out of the beam.

The TV guider is used for acquisition. As the field of view of the infrared camera MAGIC is only 1 arcmin it is very helpful to have a sensitive camera with a 4 arcmin field of view to acquire the astronomical object.

The Shack-Hartmann sensor was provided by AOA. A close-up view in Fig. 4.9 displays the individual components. The field select mirror is in a reimaged telescope pupil plane so that

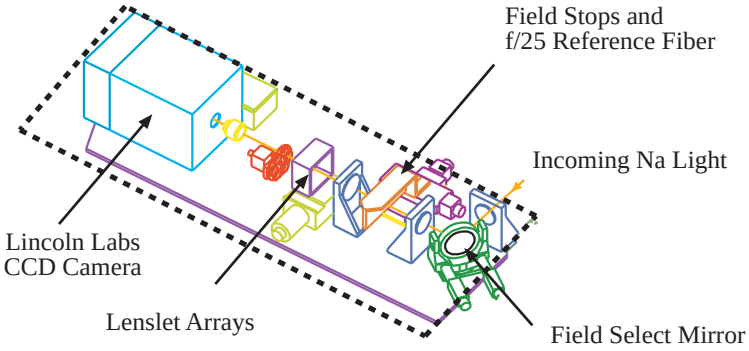

Figure 4.9: The elements of the Shack-Hartmann sensor (see Fig. 4.8 for the complete system). The field select mirror is placed in reimaged pupil plane of the telescope, moving the image in the CCD camera if the mirror is tilted. The reimaged telescope focus can be masked by applying field stops *e.g.* to block the Rayleigh scattering when using a laser guide star. The lenslet arrays can be changed remotely, the range of subapertures is from 3×3 to 12×12. The Lincoln Labs CCD camera allows frame rates between 100 and 1206 Hz.

tilting this mirror results in a movement of the image in the Lincoln Labs CCD camera. (Tilting this mirror must not be confused with the tip-tilt required for image stabilisation.) The field select mirror allows to place a star from a circle with 1 arcmin diameter around the optical axis in the center of the subimages of the Shack-Hartmann sensor. Mechanical constraints lead to this solution since the CCD camera is too large and to close to the breadboard to be moved around in the image plane. Two field stops and a reference fiber source can be inserted into the reimaged focus. The field stops are required if a natural guide star is in a dense star cluster leading to cross talk between subimages, or if the laser guide star is used and the Rayleigh scattering has to be blocked for the same reason. Eventually, the telescope pupil is imaged onto the lenslet array that forms the subimages in the CCD camera. The lenslets can be changed remotely from 3×3 subapertures to 12×12 subapertures. The focal length of all lenslets is identical so that the pixel scale in the Shack-Hartmann sensor is always $0.75''$. The CCD camera can be focused remotely, also allowing to adjust the difference in foci between a natural guide star at infinity and the laser guide star at 100 km. The difference in focal position is 70 mm in the f/25 beam.

The Lincoln Labs CCD camera has a thinned 64×64 pixel chip that is used in frame transfer mode. The maximum frame rate is 1206 Hz with a read noise of 6 electrons. At the slowest frame rate of 100 Hz the read noise is slightly higher at 9 electrons due to increased dark current as the chip is only cooled to -5°C. An upgrade of the camera will have a two stage thermo-electric cooler providing -35°C eliminating the problem with the dark current and reducing the read noise well below 5 electrons.

The tip-tilt sensor has an AstroCam (Cambridge, UK) CCD camera with a 4201 controller giving 6 electrons read noise. Except for the relay optics in front of the camera this is exactly the CHARM system. A new CCD camera head will have less than 2 electrons read noise and a quantum efficiency that is roughly doubled since the chip will be thinned.

The size of the breadboard is $2.7\,\mathrm{m}\times1.5\,\mathrm{m}$ and the whole assembly is mounted via aluminum struts to an aluminum flange that is bolted to the telescope mounting flange. The total weight (including infrared camera) is 1.1 tons. Fig. 4.10 shows the CAD drawing of the breadboard

mounted on the mirror cell and Fig. 4.11 shows a photograph of the telescope with ALFA being mounted at the mirror cell.

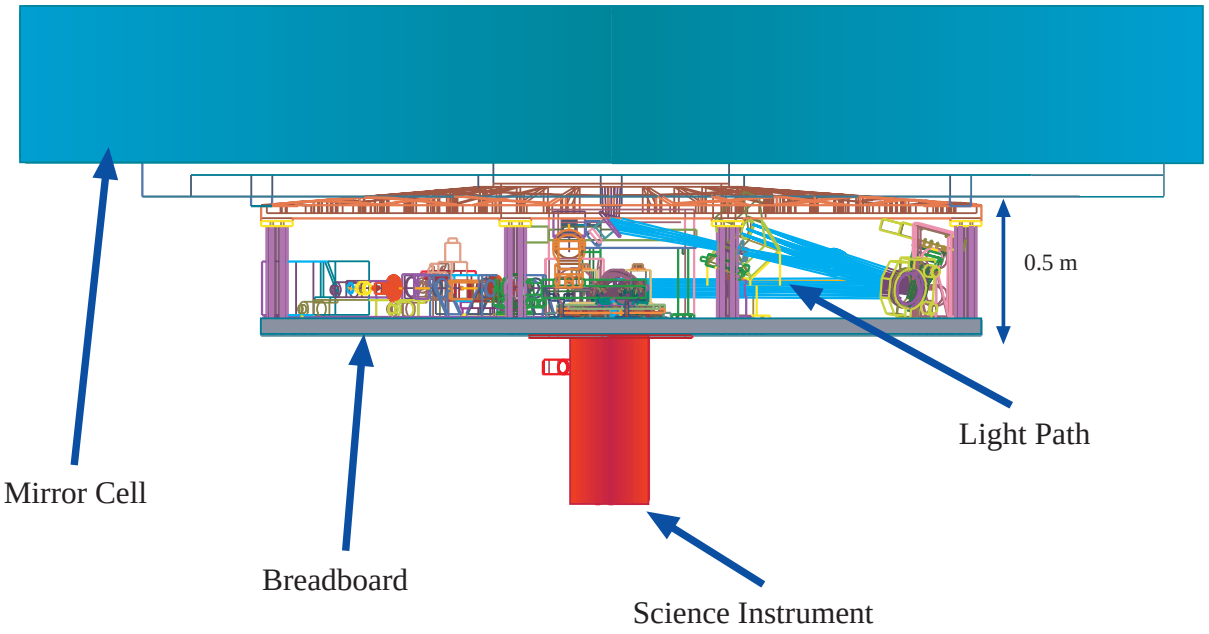

Figure 4.10: The CAD drawing of the whole system mounted on the mirror cell gives an idea of the dimensions. The orientation is the same as in Fig. 4.8 with the f/25 paraboloid on the right.

4.2.2 Calibration and wave-front reconstruction

The adaptive optics system attempts to shape the wave-front such that the spots in the subimages are in their default position. Thus, it is crucial to properly define the default positions. These positions do not necessarily correspond to the positions of a plane wave in the plane of the lenslet arrays as the light passes through a large number of optical elements between the IR/Vis beamsplitter and the lenslet array, introducing aberrations. Vice versa, a plane wave in the plane of the lenslet arrays means an aberrated wave in the plane where the beamsplitter is and, thus, in the infrared camera.

One can either try to minimise the aberrations between the beamsplitter and the lenslet array, or one aligns the optical system with the artificial point source (the f/10 reference fiber) until the image quality in the infrared camera is satisfactory. One then defines the subsequent positions of the spots in the Shack-Hartmann sensor as default positions. Now the alignment of the optical system is the crucial procedure as the adaptive optics system reconstructs exactly this shape of the wave-front. This has the consequence that any aberrations in the wave-front *e.g.* due to misalignment are reproduced by the adaptive optics system. Also, any static aberration in the deformable mirror that cannot be corrected for by aligning the f/10, the f/25 paraboloid or any other mirror limit the final image quality. Therefore, the flattening procedure with the FISBA interferometer has to be done with great care.

Only low order static aberrations up to the order that is being corrected for can be taken out

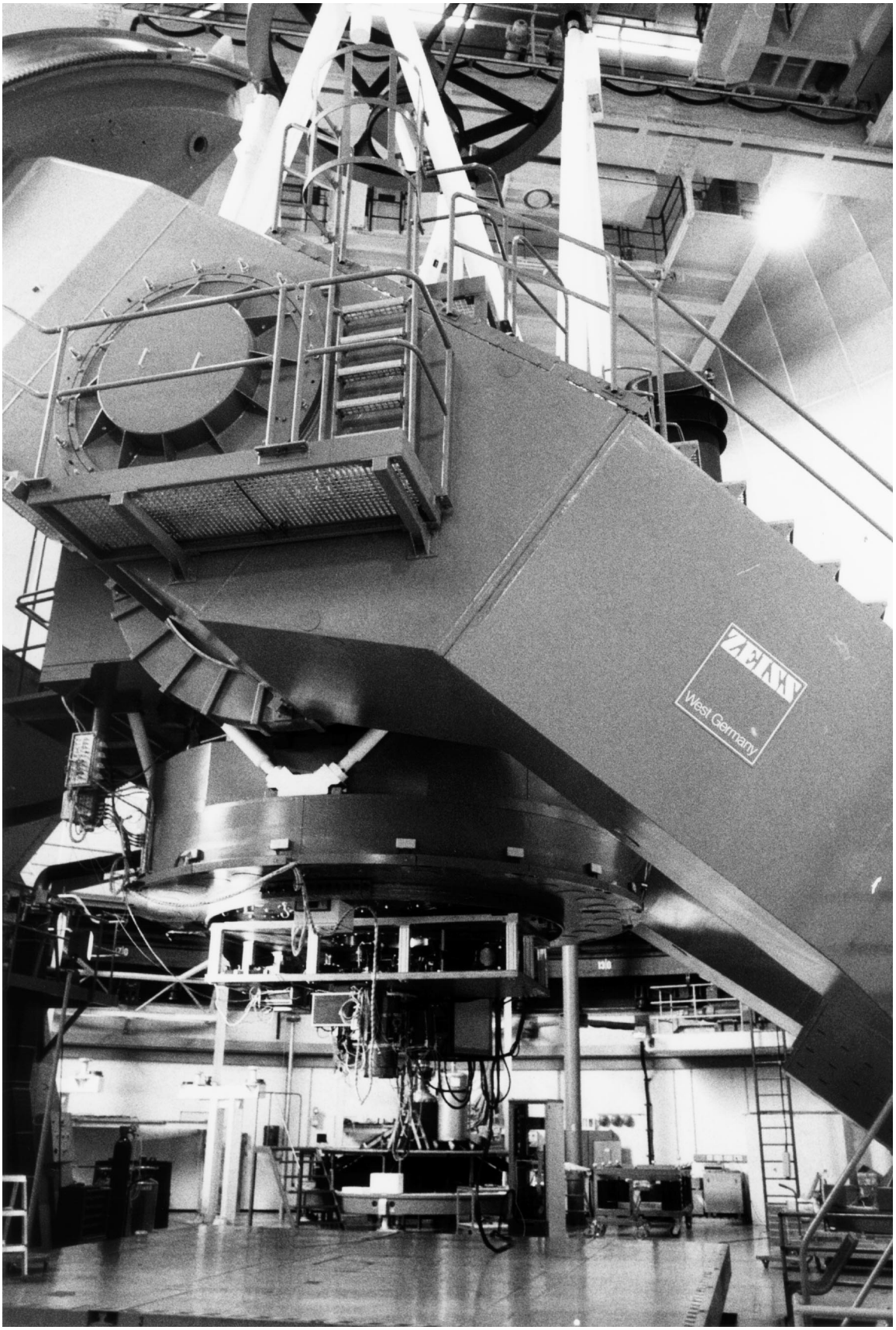

Figure 4.11: ALFA on the 3.5-m telescope at Calar Alto.

with the deformable mirror by putting offsets on the Zernike modes. Orders higher than the degree of adaptive correction, like those that appear if two neighboured actuators are differing in length cannot be corrected with Zernike offsets.

The calibration procedure consists of the following steps: After the system is optically aligned using the f/10 reference fiber as a perfect point source, the spots in the Shack-Hartmann sensor are defined as default positions and around every spot the subimage size is defined. These boxes are about $4'' \times 4''$ in size depending on the number of subapertures. In the following step, the positions of the subimage centroids are determined as a function of the Zernike modes. In Sect. 3.2.1, this process was done by computing the integral over the subaperture requiring the exact knowledge of the position of the subaperture with respect to the telescope aperture. This knowledge can be ensured by very precise adjustment of the reimaging optics. Another approach is to apply the Zernike modes (in suitable order and slightly modified to take the actuator pattern into account) to the deformable mirror, and then to measure the spot pattern in the Shack-Hartmann sensor directly. This technique was chosen by AOA. The complete calibration procedure described in this paragraph is performed automatically controlled by the software.

In terms of the wavefront reconstruction discussed in Sect. 3.3, the interaction matrix Θ_{sh} is determined experimentally by applying the Zernike modes to the deformable mirror, and the wave-front is being reconstructed using a least-squares algorithm (Eq. 3.25). The inverse of the matrix product $\Theta_{\mathrm{sh}}^T \Theta_{\mathrm{sh}}$ is calculated numerically after the calibration is finished. When the system is running in closed loop the reconstruction of the wave-front and the subsequent computation of the mirror drive signals has to be done in less than $1\,\mathrm{msec}$. There are twenty digital signal processors (DSP) to perform these tasks partially in parallel. The DSPs are mounted in groups of four on Ariel Hydra-II boards and are manufactured by Texas Instruments (TMS320 C40). Four DSPs process the subimages, subtracting the bias and correcting the gain, eight DSPs determine the image centroids and wave-front gradients, four DSPs then perform the wave-front reconstruction by multiplying the gradients with the reconstructor matrix, two DSPs apply the parameters of the control algorithm to the reconstructed modes, and two DSPs handle the input of the data from the Lincoln Labs CCD camera and the output to the deformable mirror. The total computing time is *e.g.* $0.7\,\mathrm{msec}$ if 15 modes are reconstructed from 20 subapertures.

4.2.3 Laser and launching telescope

The heart of the laser system is a $3\,\mathrm{W}$ dye ring laser pumped by a $25\,\mathrm{W}$ Argon ion laser. Both lasers are purchased from Coherent (Coherent 899 and Coherent INNOVA 200). The decision for this laser type was made because they are commercial products with all the advantages of service and warranty. The output power should be sufficient to produce a star with a magnitude of $m_V \approx 10$ (depending on meteorological conditions).

Pulse lasers with larger output power are also available but there are other problems that make them less attractive: Due to the high output power in the pulses security is a more difficult matter. The laser pulses have to be synchronised with the CCD camera. And, saturation processes in the sodium layer can limit the maximum brightness of the artificial guide star. All these difficulties make the dye laser the more sensible choice.

The laser system is placed in the Coudé laboratory of the 3.5-m telescope. The laser beam is guided backwards through the Coudé optical train to the side of the primary mirror and through

additional optical elements into the focus of the launching telescope (see Fig. 4.13). In the Coudé laboratory the required power supply, to provide 50 kW for the pump laser, and the cooling water, to dissipate the heat, are available. The cooling facility is more than one km away from the telescope avoiding the problems with home made seeing.

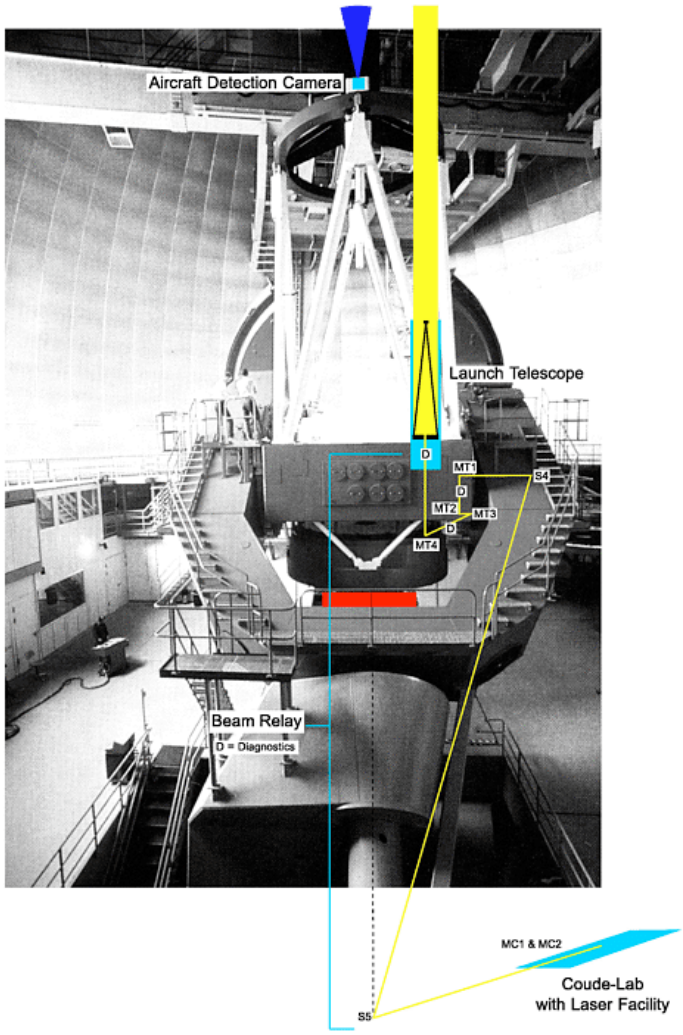

Figure 4.12: Schematics of the laser path on the 3.5-m telescope. The optical train from the Coudé focus to the mirror S4 is the standard Coudé path. The mirrors MT1 to MT4 are mounted additionally to transport the laser beam into the Cassegrain focus of the launching telescope with a diameter of 50 cm. The letter D denotes diagnostic elements in the optical path to ensure that the laser beam is held in the focus of the launching telescopes for all telescope positions. – An aircraft detection system is mounted at the front ring of the telescope.

Guiding the laser beam from the Coudé focus to the focus of the launching telescope requires a precise control of all the mirror positions since a small misalignment does not only move the position of the laser guide star but it also deteriorates the illumination of the telescope pupil, decreasing the laser power that is launched into the atmosphere. Thus, there are a number of CCD cameras and position sensitive detectors (PSD) to monitor the position of the laser beam and a

number of pilot lasers to control the position of the mirrors. This process is partially automated in a closed loop procedure. However, one should not underestimate the complexity of the task to keep the laser beam in a fixed position for all telescope angles.

Therefore, it seems very attractive to replace all the optical elements by a single optical fiber where the laser is fed in at the exit of the laser tube, and that is placed in the Cassegrain focus of the launching telescope to provide a point source. The problem is the extremely high energy density of about $1.4 \times 10^{11}\,\mathrm{W/m^2}$ at the tip of the fiber. Extreme care has to be taken to have a clean surface. First experiments with an optical fiber at Calar Alto have shown that about 70% of the light can be coupled into the fiber. The transmissivity of the mirror system is slightly higher but this is depending on the mirror surfaces.

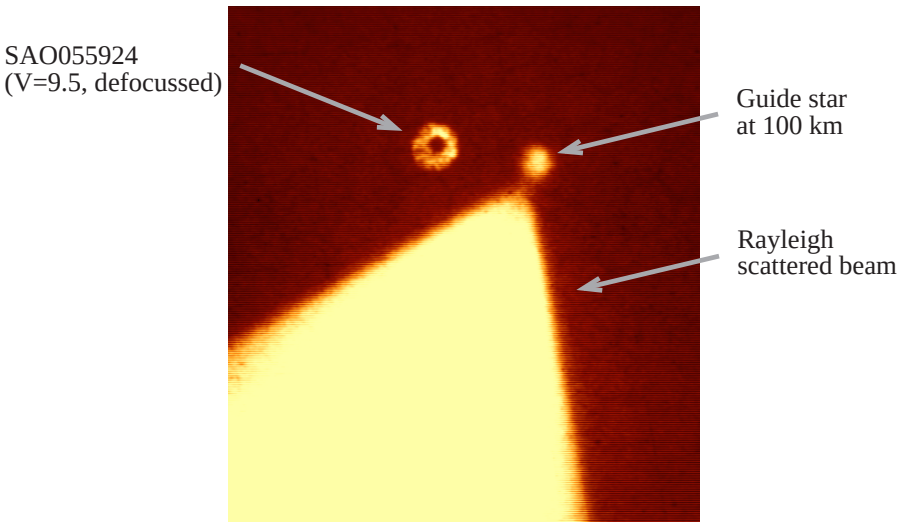

Figure 4.13: The sodium guide star and the Rayleigh scattered light seen through the TV guider camera of the 3.5-m telescope at Calar Alto. For comparison, the image of natural star is displayed too, defocused as the telescope is focused at the artificial star at an altitude of 100 km.

The illuminated diameter of the launching telescope is chosen such that it is approximately $3r_0$. Then the diameter of the instantaneous speckle image in the sodium layer is minimised. The energy density at the telescope exit is below the limits set by laser safety regulations; with less than $50\,\mathrm{W/m^2}$ this is less than a standard He-Ne laser with 0.5 mW output power and a beam diameter of about 1 mm. The aircraft detection system was installed to avoid any risk of even slightly blinding pilots.

The laser system was installed at the 3.5-m telescope in summer 1996 and in August 1996 the first laser guide star was created. Fig. 4.13 displays the first result that is compared to a natural star with magnitude $m_V = 9.5$. The defocused image of natural star – that has a ring shape because of the central obscuration of the telescope – is of comparable brightness to the laser guide star. The very bright Rayleigh scattered light has the shape of a cone.

4.2.4 Results

ALFA was taken to the telescope in September 1996, and as soon as the weather allowed we could close the loop on bright natural guide stars. The first result is shown in Fig. 4.1. During the following observing runs with a total of approximately 40 nights the progress was slower than anticipated partially due to very bad weather conditions; more than half the nights were lost, during the other half the seeing was worse than 1.5″ with very few exceptions.

It became clear very quickly that the mirror surface had to be flattened with an interferometer in order to produce a good static image in the infrared camera that is the precondition for good image quality, as described above. After the FISBA interferometer was installed and the mirror flattened to about 100 nm rms flatness, the image quality in the corrected image improved considerably. In Fig. 4.14, the 0.24″ binary ϕ Ursa Majoris is clearly resolved although the star was observed through a thin layer of clouds. The star itself was used as a guide star for the adaptive optics system in the Shack-Hartmann sensor. 20 Zernike modes were corrected, and the system was running at 900 Hz. The improved image quality compared to the very first result (see Fig. 4.1) shows particularly in the lower halo and in the reduced number of subsidiary peaks.

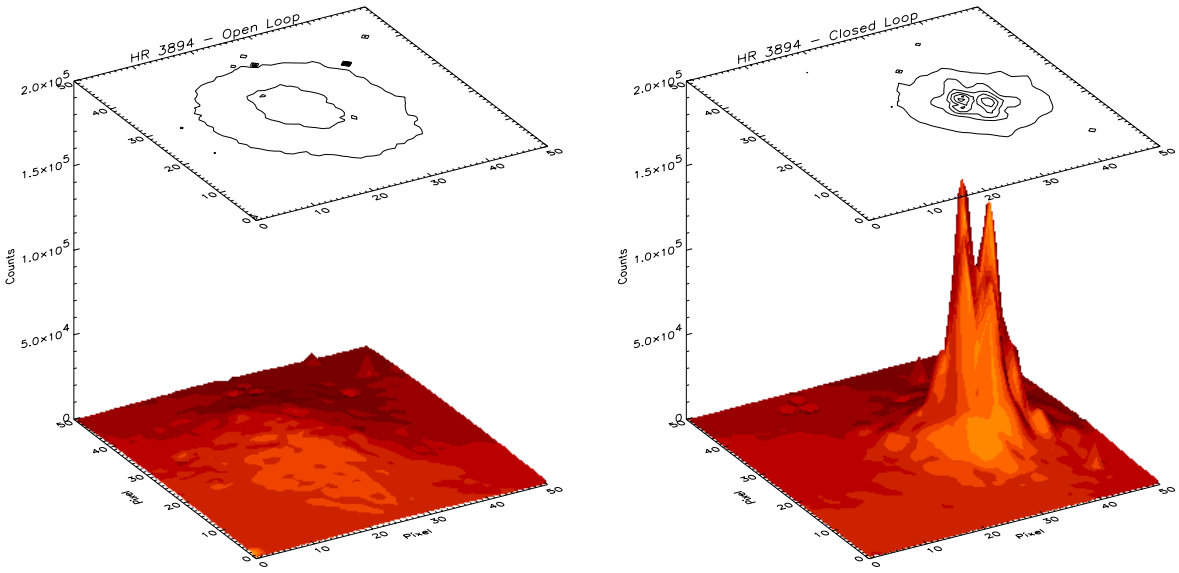

Figure 4.14: A near infrared image of the 0.24″ binary ϕ Ursa Majoris (HR 3894, $m_V = 4.6$) observed through clouds in 1.7″ seeing on March 1, 1997. The observing wavelength was 2.2 μm. 20 Zernike modes were corrected with a frame rate of 900 Hz. This is a raw image without any image processing adding up single images to a total exposure time of 50 sec. The two components are clearly resolved.

In Sect. 2.6, the temporal power spectra of the Zernike modes were discussed. Corrected and uncorrected power spectra for the Zernike modes $J = 4$ (focus) to $J = 9$ (trifoil) are displayed in Fig. 4.15 measured with 300 Hz. The corrected spectra have clearly reduced values at low frequencies. The transient frequency is around 10 Hz. All uncorrected spectra are slightly decreasing in the low frequency region below 10 Hz. Fitting an asymptote to the high frequency parts of the spectra gives values around -4 for all modes. This is slightly less than the $-17/3$

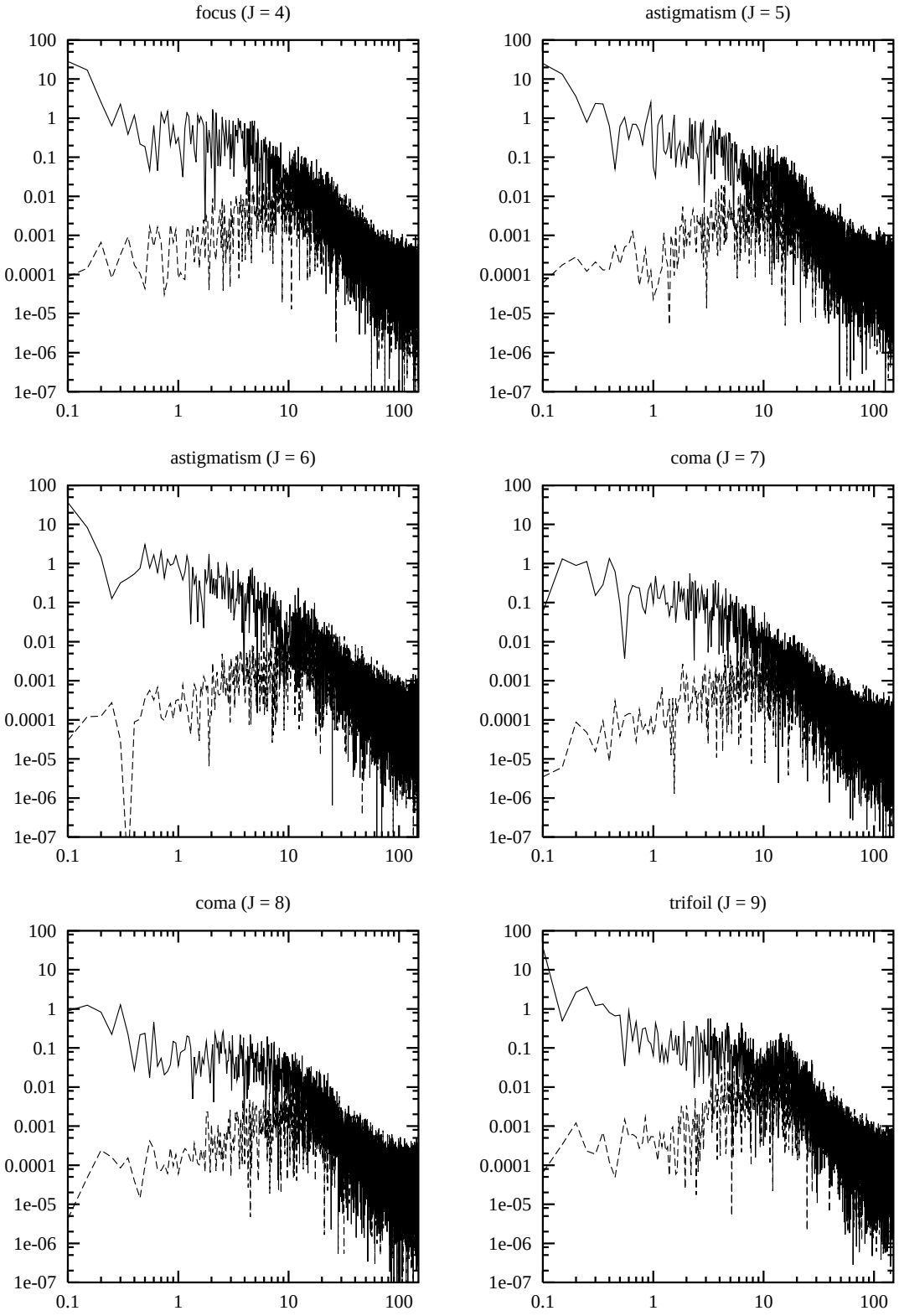

Figure 4.15: Uncorrected and corrected power spectra of six Zernike modes ($J = 4$ to 9) as a function of frequency in Hz.

predicted by the theory. The theory is confirmed, however, in predicting the *same* power law for all Zernike modes at high frequencies. The contributions of the single Zernike modes to the variance of the wave-front were calculated by Noll [62]. He found that the contribution depends on the radial order of the modes (see Table 2.2). The radial mode for $J = 4$ to 6 is $n = 2$ and for $J = 7$ to 9 $n = 3$. For the low order modes with $n = 2$ one finds a variance that is about three times larger than for $n = 3$ confirming Noll's numbers.

It was also discussed in Sect. 2.6 that – except for the lowest orders (tip and tilt) – the low frequency asymptote for the power spectra of a given radial order averaged over the azimuthal orders is a constant [11] (see Fig. 2.6). If the average of the three modes of $n = 2$ ($J = 4$ to 6) are supposed to have a constant power in the low frequency region there should be at least one that is increasing. This effect could not be measured. The predicted dependence of the transient frequency on the radial order of the Zernike modes (Eq. 2.48) could not be confirmed either. More measurements have to be taken before these questions can be answered conclusively.

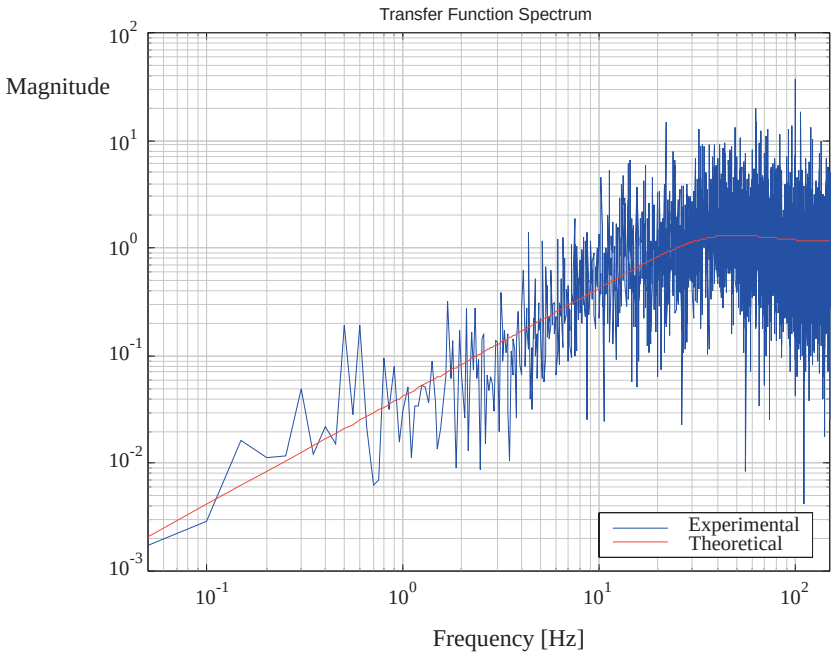

Figure 4.16: The measured and the theoretical transfer function of the closed loop system for the Zernike mode $J = 4$ (focus). The measured transfer function is the quotient of the uncorrected and the corrected spectrum displayed in Fig. 4.15. The theoretical function is calculated using the parameters of the control loop.

The corrected power spectra in Fig. 4.15 are all reduced to about 10^{-4} at low frequencies, and they approach the uncorrected spectra around the servo bandwidth of about 30 Hz. They show the same behaviour as the corrected tip-tilt spectra that were discussed in Sect. 3.4.1. Fig. 4.16 shows the measured closed loop transfer function, *i.e.* the quotient of the corrected and the uncorrected spectrum, that is compared to the theoretical transfer function which follows from the control loop parameters. The latter has been calculated by Douglas Looze from the University of Massachusetts, USA, who designed the control loop algorithm for AOA. The theoretical and the measured transfer functions agree very well indicating that the control loop is working properly.

The limiting magnitude of the current tip-tilt system is $m_V = 13.5$. With the new CCD we expect it to be around $m_V = 16$. In the Shack-Hartmann sensor we could close the loop on a $m_V = 11$ magnitude star in 1.5″ seeing. The upgrade of the CCD camera should improve this value by about two magnitudes.

The best result to date is shown in Fig. 4.17. The image of the star 14 Peg is improved from 2.4% to 20% Strehl ratio in 0.85″ seeing. The star itself was used for wave-front sensing. The Shack-Hartmann sensor was running at 100 Hz correcting 15 modes, and the tip-tilt sensor was running at 80 Hz. Thus, the system was running under the same conditions as with a laser guide star without any obvious problems.

A Strehl ratio of 20% corresponds to a phase variance of 1.6 rad^2. Correcting 17 modes perfectly reduces the wave-front phase variance to $\sigma^2_{\mathrm{fit}} = 0.6\,\mathrm{rad}^2$ (see Eq.(2.45) with $r_0 = 0.53\,\mathrm{m}$, corresponding to 0.85″ seeing). The flatness of the deformable mirror of 100 nm is equivalent to a phase variance of $\sigma^2_{\mathrm{DM}} = 0.1\,\mathrm{rad}^2$ at 2.2 μm. The Greenwood frequency at a wind speed of an estimated 9 m/sec is 7 Hz. As the system was running with a loop frequency of 100 Hz the servo bandwidth is about 10 Hz. With Eq. 3.39 the phase variance due to finite bandwidth then becomes $\sigma^2_G = \left(\frac{7\,\mathrm{Hz}}{10\,\mathrm{Hz}}\right)^{5/3} = 0.55\,\mathrm{rad}^2$. The finite servo bandwidth adds approximately 0.5 rad^2. The remaining variance of 0.35 rad^2 is due to all remaining errors in the optical alignment etc.. Estimating the variances due to finite bandwidth and imperfect alignment cannot replace the measurement of these quantities but it can give an idea of the source of the residual phase variance.

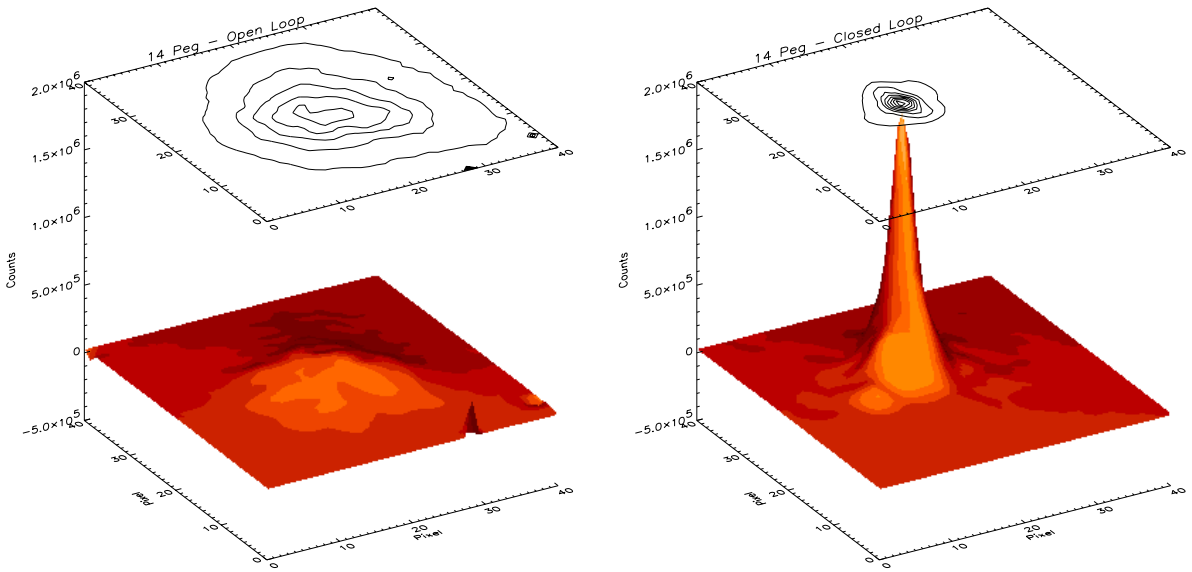

Figure 4.17: Uncorrected and corrected images of 14 Peg ($m_V = 5.04$) at 2.2 μm taken on July 21, 1997. Correcting 17 Zernike modes with a loop frequency of 100 Hz the Strehl ratio is improved from 2.4% to 20% in 0.85″ seeing. Each of the displayed images is the sum of 100 exposures of 0.2 sec. No image processing was applied.

Chapter 5

Conclusions

We have discussed effects of imaging through turbulence and methods to improve the reduced image quality with adaptive optics. The detailed description of existing adaptive optics systems has shown that the technical requirements are met by current technology. There are now about 10 telescopes in the world where adaptive optics is used on a more or less regular base. One can expect that this technology will mature considerably over the next few years, and that the impact on astronomical research will become significant. In particular the new 10-m class telescopes that will all be equipped with adaptive optics will contribute to the scientific progress since diffraction limited images from these telescopes means a factor of 20 to 50 improvement over seeing limited images.

On a more modest scale, simple tip-tilt systems improve the peak intensity by 70 to 300% and the FWHM by about 0.2″ in the near infrared, increasing the scientific output of a telescope without any significant disadvantage. Thus, it is very worthwhile to equip infrared telescopes with tip-tilt systems.

The limit of resolution is an area where large ground based telescopes are superior to observations from space telescopes since the limit for the size of a monolithic mirror in space is considerably below $10\,\mathrm{m}$. Other advantages of ground based telescopes are cost, lifetime, and flexibility as improvements or new instruments can be fitted easily.

If it comes to field of view and sky coverage, so far, the space telescopes have an advantage over observations from the ground. We have discussed methods to increase the corrected field of view of ground based observations by using multi-layer adaptive optics, and to increase the sky coverage by creating laser guide stars. For multi-layer adaptive optics one has to tackle the problems of separating the influence of single turbulent layers on the imaging process, and of applying the correction to the proper layers with multiple deformable mirrors. Laser guide stars provide a method to determine the aberrations caused by the turbulence with the exception of the wave-front slope. Although this already increases the sky coverage drastically one has to be able to deduce the tip-tilt information from the laser guide star in order to achieve 100% sky coverage. The research has to concentrate on these two areas to make observations from the ground competetive with space observations.

Since angular resolution is of key importance in most areas of astronomical research the desire for higher resolution does not stop at $10\,\mathrm{m}$ apertures. However, rather than envisioning larger monolithic telescopes, interferometer arrays are planned and tested, coherently switching

together the light from single telescopes. Then, the limit of resolution is given by the longest baseline. The most challenging projects in this area are the interferometric connection of the two Keck Telescopes, the VLTI connecting eventually the four Very Large Telescopes in Parranal, Chile and the interferometric mode of the LBT. Each of the single 8-10 m apertures requires adaptive optics to increase the peak intensity and the accuracy of the measurement. The coherently combined beams display a fringe pattern that moves around randomly depending on the wave-front slope between the single apertures. This cannot be corrected for by the adaptive optics systems in each telescope. Similar to the problem of the tip-tilt measurement with a natural guide star in a laser guide star system one needs a natural guide star to stabilise the fringe motion.

Here, one faces the same problems as with single telescope adaptive optics. The correction frequency for fringe tracking is affected by the telescope baseline and by the observing wavelength. This determines the limiting magnitude. If the scientific object is not bright enough to serve as a guide star there has to be a star of suitable brightness usually within a few arcsec of the scientific object. Then, one can use the guide star to stabilise the fringe motion, and one can integrate on the scientific object. Increasing the angle between the object and the guide star is most desirable since it improves the sky coverage. This technique has to be mastered in order to make telescope interferometers useful. The experience with adaptive optics systems is a stepping stone to solving these problems.

Bibliography

[1] D. S. Acton and R. C. Smithson, "Solar imaging with a segmented adaptive mirror", Appl. Opt., **31**, 3161–3169, 1992.

[2] D. M. Alloin and J. M. Mariotti (Eds.), *Adaptive Optics for Astronomy*. Vol C423, NATO Advanced Study Institute Series, Kluwer Academic Publishers, 1994.

[3] H. W. Babcock, "Possibility of compensating astronomical seeing", Publ. Astron. Soc. Pac., **65**, 229, 1953.

[4] T. Berkefeld. Dissertation, Universität Heidelberg, 1997.

[5] M. Born and E. Wolf, *Principles of optics*. Pergamon Press, Oxford, 1970.

[6] R. N. Bracewell, *The Fourier transform and its applications*. 2nd edn, McGraw-Hill, New York, 1986.

[7] B. J. Carter, E. J. Kibblewhite, W. J. Wild, J. R. P. Angel, M. Lloyd-Hart, B. P. Jacobsen, D. M. Wittman, and J. W. Beletic, "Sodium beacon used for adaptive optics on the multiple mirror telescope", in *Adaptive Optics for Astronomy*, Eds. D. M. Alloin and J. M. Mariotti, pp. 205–210. Vol C423, NATO Advanced Study Institute Series, Kluwer Academic Publishers, 1994.

[8] J. C. Christou, "Image quality, tip-tilt correction and shift-and-add infrared imaging", Publ. Astron. Soc. Pac., **103**, 1040–1048, 1991.

[9] S. F. Clifford, "The classical theory of wave propagation in a turbulent medium", in *Laser Beam Propagation in the Atmosphere, Topics in Applied Physics, Vol. 25*, Ed. J. W. Strobehn, pp. 9–43, Springer-Verlag, Berlin, 1968.

[10] M. M. Colavita, "Design considerations for very long baseline fringe-tracking interferometers", in *Amplitude and Intensity Interferometer*, Ed. J. Breckinridge, pp. 80–86. Proc .SPIE 1237, 1990.

[11] J. M. Conan, G. Rousset, and P. Y. Madec, "Wave-front temporal spectra in high-resolution imaging through turbulence", J. Opt. Soc. Am. A, **12**, 1559–1570, 1995.

[12] M. Demerle, P. Y. Madec, and G. Rousset, "Servo-loop analysis for adaptive optics", in *Adaptive Optics for Astronomy*, Eds. D. M. Alloin and J. M. Mariotti, pp. 73–88. Vol C423, NATO Advanced Study Institute Series, Kluwer Academic Publishers, 1994.

[13] A. P. Doel, C. N. Dunlop, J. V. Major, R. M. Myers, A. Purvis, and M. G. Thompson, "Stellar image stabilisation using piezo-driven active mirrors", in *Advanced Technology Optical Telescopes IV*, Ed. L. D. Barr, pp. 179–192. Proc. SPIE 1236, 1990.

[14] R. Foy and A. Labeyrie, "Feasibility of adaptive telescope with laser probe", Astronomy&Astrophysics, **152**, 129–131, 1985.

[15] R. Foy, A. Migus, F. Biraben, G. Grynberg, P. R. McCullough, and M. Tallon, "The polychromatic artificial sodium star: A new concept for correcting the atmospheric tilt", Astronomy&Astrophysics Supplement Series, **111**, 569–578, 1995.

[16] D. L. Fried, "Statistics of a geometric representation of wavefront distortion", J. Opt. Soc. Am., **55**, 1427–1435, 1965.

[17] D. L. Fried, "Optical resolution through a randomly inhomogeneous medium for very long and very short exposures", J. Opt. Soc. Am., **56**, 1372–1379, 1966.

[18] R. Q. Fugate, B. L. Ellerbroek, C. H. Higgins, M. P. Jelonek, W. J. Lange, A. C. Slavin, W. J. Wild, D. M. Winker, and J. M. Wynia, "Two generations of laser-guide-star adaptive-optics experiments at the Starfire Optical Range", J. Opt. Soc. Am. A, **11**, 310–324, 1994.

[19] R. Q. Fugate, D. L. Fried, G. A. Ameer, B. R. Boeke, S. L. Browne, P. H. Roberts, R. E. Ruane, G. A. Tyler, and L. M. Wopat, "Measurement of atmospheric wave-front distortion using scattered light from a laser guide star", Nature (London), **353**, 144–146, 1991.

[20] A. Glindemann, *Das Bild der Kante bei teilkohärenter Beleuchtung - Rechnungen und Experimente*. Dissertation, Technische Universität Berlin, 1989.

[21] A. Glindemann, "Improved performance of adaptive optics in the visible", J. Opt. Soc. Am. A, **11**, 1370–1375, 1994.

[22] A. Glindemann, "Relevant parameters for tip-tilt systems on large telescopes", Publ. Astron. Soc. Pac., **109**, 682–687, 1997.

[23] A. Glindemann and T. Berkefeld, "A new method for separating atmospheric layers using a shack-hartmann curvature sensor", in *Adaptive Optics, Vol. 13, 1996 OSA Technical Digest Series*, pp. 153–155, Washington DC, 1996. Optical Society of America.

[24] A. Glindemann, D. Hamilton, S. Hippler, R.-R. Rohloff, and K. Wagner, "ALFA – the laser guide star adaptive optics system for the calar alto 3.5-m telescope", in *Laser Technology for Laser Guide Star Adaptive Optics Astronomy*, Eds. N. Hubin and H. Friedman, p. in press, Garching, Germany, 1997. European Southern Observatory.

[25] A. Glindemann, R. G. Lane, and J. C. Dainty, "Simulation of time-evolving speckle patterns using kolmogorov statistics", J. Mod. Optics, **40**, 2381–2388, 1993.

[26] A. Glindemann, M. J. McCaughrean, S. Hippler, C. Birk, K. Wagner, and R. R. Rohloff, "CHARM - a tip-tilt tertiary system for the Calar Alto 3. 5m-telescope", Publ. Astron. Soc. Pac., **109**, 688–696, 1997.

[27] A. Glindemann, E. Pitz, S. Hippler, R. R. Rohloff, and K. Wagner, "The tip-tilt system of the UKIRT Upgrades Programme", in preparation, 1997.

[28] A. Glindemann and N. P. Rees, "UKIRT 5-axis tip-tilt secondary – wavefront sensor simulations", in *ICO-16 Satellite Conference on Active and Adaptive Optics*, Ed. F. Merkle, pp. 273–278, Garching, Germany, 1993. European Southern Observatory.

[29] A. Glindemann and N. P. Rees, "Photon counting vs. CCD sensors for wavefront sensing - Performance comparison in the presence of noise", in *Advanced Technology Optical Telescopes V*, Ed. P. S. Idell, pp. 824–834. Proc. SPIE 2199, 1994.

[30] J. W. Goodman, *Introduction to Fourier optics*. McGraw-Hill, San Francisco, 1968.

[31] D. P. Greenwood, "Bandwidth specification for adaptive optics systems", J. Opt. Soc. Am., **67**, 390–393, 1977.

[32] D. P. Greenwood and D. L. Fried, "Power spectra requirements for wave-front-compensative systems", J. Opt. Soc. Am., **66**, 193–206, 1976.

[33] C. A. Haniff, J. E. Baldwin, P. J. Warner, and T. R. Scott, "Atmospheric phase fluctuation measurement: Interferometric results from the WHT and COAST telescopes", in *Amplitude and Spatial Interferometry II*, Ed. J. Breckinridge, pp. 407–417. Proc. SPIE 2200, 1994.

[34] W. Happer, G. MacDonald, C. Max, and F. J. Dyson, "Atmospheric-turbulence compensation by resonant optical backscatter from the sodium layer in the upper atmosphere", J. Opt. Soc. Am. A, **11**, 263–275, 1994.

[35] J. W. Hardy, J. E. Lefebvre, and C. L. Koliopoulos, "Real-time atmospheric compensation", J. Opt. Soc. Am., **67**, 360–369, 1977.

[36] T. G. Hawarden, Private communication, 1997.

[37] T. G. Hawarden, C. P. Cavedoni, T. C. Chuter, I. A. Look, N. P. Rees, D. G. Pettie, R. J. Bennett, E. Atad, J. W. Harris, C. M. Humphries, B. Mack, E. Pitz, A. Glindemann, S. Hippler, R. R. Rohloff, and K. Wagner, "Progress of the UKIRT Upgrades Programme", in *Optical Telescopes of Today and Tomorrow*, Ed. A. Ardeberg, pp. 256–266. Proc. SPIE 2871, 1996.

[38] T. M. Herbst, S. V. W. Beckwith, C. Birk, S. Hippler, M. J. McCaughrean, F. Mannuccu, and J. Wolf, "MAGIC: A new near infrared camera for Calar Alto", in *Infrared Detectors and Instrumentation*, pp. 605–611. Proc. SPIE 1946, 1993.

[39] J. Herrmann, "Phase variance and Strehl ratio in adaptive optics", J. Opt. Soc. Am. A, **9**, 2257–2258, 1992.

[40] J. M. Hill, "The Large Binocular Telescope project", in *Optical Telescopes of Today and Tomorrow*, Ed. A. Ardeberg, pp. 57–68. Proc. SPIE 2871, 1996.

[41] R. E. Hufnagel, "Variations of atmospheric turbulence", in *Digest of Technical Papers, Topical Meeting on Optical Propagation through Turbulence*, pp. WA1/1–WA1/4, Optical Society of America, Washington, D. C., 1974.

[42] R. A. Humphries, C. Primmerman, L. Bradley, and J. Herrmann, "Atmospheric turbulence measurements using a synthetic beacon in the mesospheric sodium layer", Opt. Lett., **16**, 1367–1369, 1991.

[43] A. Ishimura, *Wave Propagation and Scattering in Random Media*. Academic, New York, 1978.

[44] D. C. Johnston and B. M. Welsh, "Analysis of multiconjugate adaptive optics", J. Opt. Soc. Am. A, **11**, 394–408, 1994.

[45] V. A. Klückers, N. J. Wooder, M. A. Adcock, T. W. Nicholls, and J. C. Dainty, "Profiling of atmospheric turbulence strength and velocity using a generalised SCIDAR technique", Astronomy&Astrophysics, p. in press, 1997.

[46] A. N. Kolmogorov, "The local structure of turbulence in incompressible viscous fluids for very large Reynolds' numbers", in *Turbulence, Classical Papers on Statistical Theory*, Eds. S. K. Friedlander and L. Topper, pp. 151–155. Wiley-Interscience, 1961.

[47] R. G. Lane and A. Glindemann, "Comparison of computer post-processing and low order adaptive optics", in *Digital Image Recovery and Synthesis II*, Ed. P. S. Idell, pp. 275–286. Proc. SPIE 2029, 1993.

[48] R. G. Lane, A. Glindemann, and J. C. Dainty, "Simulation of a Kolmogorov phase screen", Wav. Rand. Med., **2**, 209–224, 1992.

[49] R. G. Lane and M. Tallon, "Wave-front reconstruction using a Shack-Hartmann sensor", Appl. Opt., **31**, 6902–6908, 1992.

[50] N. F. Law and R. G. Lane, "Wavefront estimation at low light levels", Opt. Commun., **126**, 19–24, 1996.

[51] M. Lloyd-Hart, J. P. R. Angel, B. Jacobsen, D. Wittman, R. Dekany, D. McCarthy, E. Kibblewhite, W. Wild, B. Carter, and J. Beletic, "Adaptive optics experiments using sodium laser guide stars", ApJ, **439**, 455–473, 1995.

[52] G. Love, N. Andrews, P. Birch, D. Buscher, P. Doel, C. Dunlop, J. Major, R. Myers, A. Purvis, R. Sharples, A. Vick, A. Zadrozny, S. R. Restaino, and A. Glindemann, "Binary adaptive optics: atmospheric wave-front correction with a half-wave phase shifter", Appl. Opt., **34**, 6058–6066, 1995.

[53] A. S. Marathay, *Elements of optical coherence theory*. J. Wiley & Sons, New York, 1982.

[54] H. M. Martin, "Image motion as a measure of seeing quality", Publ. Astron. Soc. Pac., **99**, 1360–1370, 1987.

[55] C. E. Max, S. S. Olivier, H. W. Friedman, J. An, K. Avicola, B. V. Beeman, H. D. Bissinger, J. M . Brase, G. V. Ebert, D. T. Gavel, K. Kanz, M. C. Liu, B. Macintosh, K. P. Neeb, J. Patience, and K. E. Waltjen, "Image improvement from a Sodium-layer laser guide star adaptive optics system", Science, **277**, 1649–1652, 1997.

[56] M. J. McCaughrean and J. R. Stauffer, "High resolution near-infrared imaging of the Trapezium: a stellar census", AJ, **108**, 1382–1399, 1994.

[57] B. L. McGlamery, "Computer simulation studies of compensation of turbulence degraded images", in *Image Processing*, pp. 225–233. Proc. SPIE/OSA 74, 1976.

[58] J. L. Melsa and D. L. Cohn, *Decision and estimation theory*. McGraw-Hill, New York, 1978.

[59] E. Menzel, Optik, **8**, 295–301, 1951.

[60] F. Merkle, P. Kern, P. Léna, F. Rigaut, J. C. Fontanella, G. Rousset, C. Boyer, J. P. Gaffard, and P. Jagourel, "Successful tests of adaptive optics", ESO Messenger, **58**, 1–4, 1989.

[61] D. V. Murphy, C. A. Primmerman, D. A. Page, B. G. Zollars, and H. T. Barclay, "Experimental demonstration of atmospheric compensation using multiple synthetic beacons", Opt. Lett., **16**, 1797–1799, 1991.

[62] R. J. Noll, "Zernike polynomials and atmospheric turbulence", J. Opt. Soc. Am., **66**, 207–211, 1976.

[63] A. M. Obukhov, Izv. Akad. Nauk S. S. S. R. , Ser. Geograf. Geofiz., **13**, 58, 1949.

[64] J. Primot, G. Rousset, and J. C. Fontanella, "Deconvolution from wave-front sensing: a new technique for compensating turbulence-degraded images", J. Opt. Soc. Am. A, **7**, 1598–1608, 1990.

[65] A. Quirrenbach, W. Hackenberg, H.-C. Holstenberg, and N. Wilnhammer, "The sodium laser guide star system of ALFA", in *Adaptive Optics and Applications*, Eds. R. K. Tyson and R. Q. Fugate, p. in press. Proc. SPIE 3126, 1997.

[66] R. Ragazzoni, "Absolute tip-tilt determination with laser beacons", Astronomy&Astrophysics, **305**, L13–L16, 1996.

[67] N. Rees and S. Hippler, "Controlling the UKIRT upgrades program", in *Telescope Control Systems*, Ed. P. T. Wallace, pp. 2–10. Proc. SPIE 2479, 1995.

[68] E. N. Ribak, "Deformable mirros", in *Adaptive Optics for Astronomy*, Eds. D. M. Alloin and J. M. Mariotti, pp. 149–162. Vol C423, NATO Advanced Study Institute Series, Kluwer Academic Publishers, 1994.

[69] E. N. Ribak, E. Gershnik, and M. Cheselka, "Stellar scintillations as a remote atmospheric wave-front sensor", Opt. Lett., **21**, 435–437, 1996.

[70] F. Rigaut, "Astronomical reference sources", in *Adaptive Optics for Astronomy*, Eds. D. M. Alloin and J. M. Mariotti, pp. 163–183. Vol C423, NATO Advanced Study Institute Series, Kluwer Academic Publishers, 1994.

[71] F. Rigaut, "Performance of the Canada-France-Hawaii telescope adaptive optics bonnette", Astronomy&Astrophysics, p. in preparation, 1997.

[72] F. Rigaut and E. Gendron, "Laser guide star in adaptive optics: the tilt determination problem", Astronomy&Astrophysics, **261**, 677–684, 1992.

[73] F. Roddier, "The effects of atmospheric turbulence in optical astronomy", in *Progress in Optics XIX*, Ed. E. Wolf, pp. 281–376, Amsterdam, North-Holland, 1981.

[74] F. Roddier, "Curvature sensing and compensation: a new concept in adaptive optics", Appl. Opt., **27**, 1223–1225, 1988.

[75] F. Roddier, "Wavefront sensing and the irradiance transport equation", Appl. Opt., **29**, 1402–1403, 1990.

[76] F. Roddier, M. Northcott, and J. E. Graves, "A simple low-order adaptive optics system for near-infrared applications", Publ. Astron. Soc. Pac., **103**, 131–149, 1991.

[77] F. Roddier, M. J. Northcott, J. E. Graves, D. L. McKenna, and D. Roddier, "One-dimensional spectra of turbulence-induced zernike aberrations: time-delay and isoplanicity error in partial adaptive compensation", J. Opt. Soc. Am. A, **10**, 957–965, 1993.

[78] N. Roddier, "Atmospheric wavefront simulation using Zernike polynomials", Opt. Eng., **29**, 1174–1180, 1990.

[79] M. C. Roggemann and B. M. Welsh, *Imaging through the atmosphere*. CRC, Boca Raton, 1996.

[80] G. Rousset, "Wavefront sensing", in *Adaptive Optics for Astronomy*, Eds. D. M. Alloin and J. M. Mariotti, pp. 115–137. Vol C423, NATO Advanced Study Institute Series, Kluwer Academic Publishers, 1994.

[81] P. Salinari, C. Del Vecchio, and V. Biliotti, "A study of an adaptive secondary mirror", in *ICO-16 Satellite Conference on Active and Adaptive Optics*, Ed. F. Merkle, pp. 247–253, Garching, Germany, 1993. European Southern Observatory.

[82] S. A. Sallberg, B. M. Welsh, and M. C. Roggemann, "Maximum *a posteriori* estimation of wave-front slopes using a Shack-Hartmann wave-front sensor", J. Opt. Soc. Am. A, **6**, 1347–1354, 1997.

[83] D. G. Sandler, M. Lloyd-Hart, P. Gray, T. Martinez, and R. Angel, "The 6.5m MMT infrared adaptive optics system: Detailed design and progress report", in *Adaptive Optics, Vol. 23, 1995 OSA Technical Digest Series*, pp. 25–27, Washington DC, 1995. Optical Society of America.

[84] M. F. Smutko, M. Chun, F. Shi, V. Scor, W. Wild, J. Larkin, and E. Kibblewhite, "An overview of the Chicago adaptive optics system", Bull. American Astron. Soc., **28**, 1996.

[85] V. I. Tatarski, *Wave propagation in a turbulent medium*. McGraw-Hill, New York, 1961.

[86] V. I. Tatarski and V. U. Zavorotny, "Atmospheric turbulence and the resolution limits of large ground-based telescopes: comment", J. Opt. Soc. Am. A, **10**, 2410–2417, 1993.

[87] L. A. Thompson and C. S. Gardner, "Experiments on laser guide stars at Mauna Kea Observatory for adaptive imaging in astronomy", Nature, **328**, 229–231, 1987.

[88] G. A. Tyler, "Bandwidth considerations for tracking through turbulence", J. Opt. Soc. Am. A, **11**, 358–367, 1994.

[89] R. K. Tyson, *Principles of adaptive optics*. Academic Press, San Diego, 1991.

[90] G. C. Valley, "Isoplanatic degradation of tilt correction and short-term imaging systems", Appl. Opt., **19**, 574–577, 1980.

[91] G. Vdovin and P. M. Sarro, "Flexible mirror micromachined in silicon", Appl. Opt., **34**, 2968–2972, 1995.

[92] J. Vernin and F. Roddier, "Experimental determination of two-dimensional spatiotemporal power spectra of stellar light scintillation. evidence for a multilayer structure of the air turbulence in the upper troposphere", J. Opt. Soc. Am., **63**, 270–273, 1973.

[93] E. P. Wallner, "Optimal wave-front correction using slope measurements", J. Opt. Soc. Am., **73**, 1771–1776, 1983.

[94] Eds. R. C. Weast and M. J. Astle, *CRC Handbook of Chemistry and Physics*. CRC, Boca Raton, 1981.

[95] D. Wittman, R. Angel, M. Lloyd-Hart, D. Colucci, and D. McCarthy, "Optical sensing of infrared wavefronts for adaptive control: a new CCD detector and MMT experiments", in *ESO Conference on Progess in Telescope and Instrumentation Technologies*, Ed. M. H. Ulrich, pp. 453–460, Garching, Germany, 1992. European Southern Observatory.

[96] J. C. Wyant, "White light extended source shearing interferometer", Appl. Opt., **13**, 200–202, 1974.

[97] F. Zernike, Physica, **1**, 689, 1934.